1nm

A Double Aberration Corrected, Energy Filtered HREM/STEM

Angus I. Kirkland[†], John M. Titchmarsh[†], John L. Hutchison[†], David J. H. Cockayne[†], Crispin J. D. Hetherington[†], Ron C. Doole[†], Hidetaka Sawada[††], Max Haider[†††]and Peter Hartel[†††]

[†]**Department of Materials, University of Oxford**
[††]**Technical Division, JEOL Ltd.**
[†††]**CEOS GmbH.**

Contents

Cover micrograph

Phase of the exit plane wavefunction of the complex oxide $FeF_3 \cdot 6Nb_2O_5$ recovered from a focal series of aberration corrected images to a resolution of 0.09 nm. The insets show a structural model and an enlargement of the marked region in which both cation and O anion columns are visible.

Courtesy of Dr. Angus I. Kirkland, Department of Materials, University of Oxford.

JEOL
Serving Advanced Technology

A combined 200 kV HREM/STEM incorporating aberration correctors in both probe-forming and imaging lenses has been installed at Oxford University. This unique instrument is also equipped with an Ω-type in-column energy filter, annular dark field detectors both above and below the filter, and an EDX system. This paper presents an overview of the instrument together with data from initial performance tests that have demonstrated < 0.1 nm resolution in both TEM and STEM imaging modes.

Introduction

Transmission Electron Microscopy (TEM) is now clearly established as an invaluable tool in the determination of the structure and structural chemistry of a range of technologically important materials. In the last decade significant advances in instrumentation have been made with the development of Field Emission Gun (FEG) electron sources [1, 2] operating at intermediate (200-300 kV) voltages. These instruments provide imaging at close to 0.1 nm resolution, together with sub nanometer diameter bright probes which can be used to collect Electron Energy Loss Spectra (EELS) and to map characteristic X-Ray emission (EDX) peak intensities, providing chemical as well as structural information.

However, in the case of high resolution imaging, much of the extra information available can only be usefully extracted using indirect computational techniques such as exit wave reconstruction [3] or holography [4] due to the rapid oscillations in the wave aberration function at high spatial frequencies arising from the increased coherence of the source.

For Scanning Transmission Electron Microscope (STEM) based imaging and analysis on the nm scale FEG sources are also indispensable providing increased probe current and reduced probe diameter. In parallel the development of energy-filtered imaging systems [5, 6] has enabled the intensity from electrons scattered inelastically by mechanisms other than phonon scattering to be eliminated from individual HREM images, improving quantitative interpretation and has enabled high resolution Electron Energy Loss Spectra (EELS) to be acquired.

A major practical challenge is now to further improve the limits of TEM and STEM resolution simultaneously by incorporating aberration correctors [7, 8] together with other analytical equipment, including energy filters in a single electron optical column. Recently this has been achieved and we present here the first of this new generation of aberration-corrected analytical FEGTEM/STEM instruments, recently installed at Oxford University's Department of Materials. This unique instrument incorporates hexapole based aberration correctors in both the imaging and probe forming lenses [7, 8], together with an in column Ω type electron energy filter [5]. Pre and post filter High Angle Annular Dark Field (HAADF) detectors are also fitted, in addition to an EDX detector.

In this paper we first describe the instrument, and then present results from preliminary performance tests together with early results from various active areas of materials research at Oxford.

Design and Construction

The basic instrument (**Figure 1**) is based on the new JEOL JEM-2200FS column, incorporating a Schottky field-emission gun operating at up to 200 kV [2]. The aberration correctors are inserted into the column above and below the standard objective lens to enable aberration

[†]Parks Road, Oxford OX1 3PH, U.K.
 E-mail: angus.kirkland@materials.ox.ac.uk

correction of both the illumination (CESCOR) and imaging (CETCOR) systems. Both correctors are based on a pair of strong hexapoles separated by a round doublet transfer lens enabling the correction of spherical and other aberrations to third order [7, 8]. In addition a series of additional weak multipoles are included within the correctors for adjustment of the beam axis and for the correction of residual parasitic aberrations. In order to ensure excellent mechanical and magnetic stability the electron optical column incorporates specially designed and improved magnetic coupling yokes and, as noted later, we have successfully maintained a stable corrected state over many hours. The electron energy filter is a corrected in-column Ω-type [5, 9] providing isochromatic imaging and diffraction together with high resolution EELS. Annular Dark Field detectors are fitted above and below the filter together with a conventional bright field STEM detector below the filter. An EDX detector (50 mm^2 thin window Si(Li)) is also attached to the column. The specimen stage is fully motorized on five axes and integrated piezo drives are provided for precise control of the specimen shifts.

The instrument is configured for full remote operation of the complete electron optical column including both correctors and all ancillary systems (apertures, detectors etc.) using five separate PCs communicating across a local area network and running a combination of Windows® and Unix® operating systems.

For remote viewing at TV rate a Hamamatsu (wide screen) camera system is used which includes automated black level, shutter and gain control, together with a Gatan Ultrascan 2024 × 2024 CCD camera coupled to an independent phosphor for high resolution image recording.

Aberration Correction and Measurement

The Scherzer resolution [10] of the uncorrected objective lens (C_s = 0.5 mm) is 0.19 nm, (**Figure 2(a)**) measured from the calculated power spectrum of an image of a thin amorphous Ge film, calibrated from lattice fringes of Au particles with an information limit better than 0.14 nm. In order to obtain a corrected state, the tilt-induced values of 2-fold astigmatism and defocus are measured from a Zemlin tableau [11] of power spectra obtained from images recorded for a range of beam tilts. From these measured values the complete set of aberration coefficients to third order are calculated [12] and these values are used to apply appropriate voltages to the individual electron optical elements of the post imaging corrector.

In the corrected state, a typical set of calculated aberration coefficients are listed in **Table 1**. For images recorded in this condition the measured continuous signal transfer limits, as measured directly from the Young's Fringe pattern shown in **Figure 2(b)**, corresponding to 37% and 10% are 0.14(5) nm and 0.12(4) nm respectively. As the signal limit is now determined by higher order aberrations and effects of incoherent damping terms this data


Fig. 1 The JEOL JEM-2200FS installed at Oxford showing major electron optical components and detectors. The local computer network controlling the microscope, correctors and ancillary devices is visible in the foreground.

A_1	2-fold astigmatism	239.3 pm
A_2	3-fold astigmatism	33.5 nm
A_3	4-fold astigmatism	639.5 nm
A_4	5-fold astigmatism	18.2 µm
A_5	6-fold astigmatism	1.626 mm
B_2	1st order Axial coma	4.625 nm
B_4	2nd order Axial coma	71.15 µm
S_3	Star aberration	685.4 nm
D_4		13.94 µm
C_1	Defocus	-301.5 nm
C_3	Spherical aberration	802.0 nm
C_5		-2.08 mm

Table 1 Values of individual aberration coefficients to 5th order after correction of CETCOR.
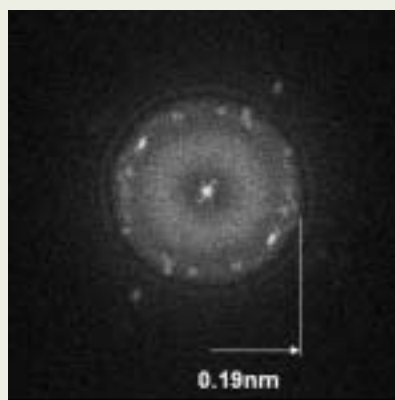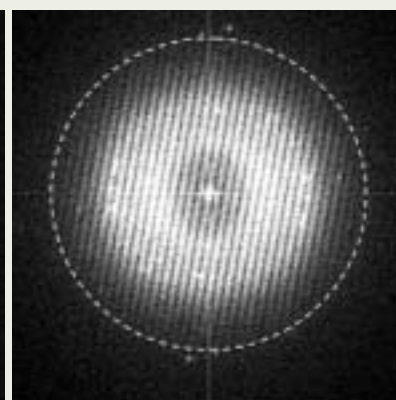

Fig. 2 Power spectra calculated from high resolution images of an amorphous Ge foil in both (a) uncorrected (at the Scherzer defocus) and (b) corrected TEM states. In the corrected state the power spectrum illustrated was calculated from a pair of laterally displaced images of a thin amorphous Ge film and shows information transfer to 0.12(4) nm (marked with a circle), corresponding to 10% signal transfer.
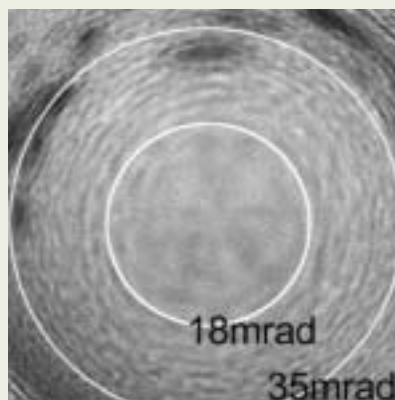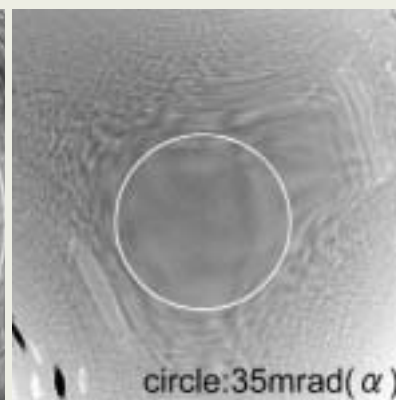
Fig. 3 Ronchigrams recorded from the same specimen as Fig. 2 in both uncorrected and corrected STEM states.

also serves to confirm the excellent mechanical and electrical stability of the total system.

High resolution STEM imaging *and* analysis both require the smallest possible probe with the highest possible current. This has previously been successfully achieved in corrected, dedicated cold field emission gun STEM instruments using an alternative corrector design based on a combination of quadrupoles and octupoles [13]. However, this is now also realized for the first time in a combined TEM/STEM instrument using a hexapole based corrector.

The measurement and subsequent correction of aberrations in the illumination system requires a suitable specimen that contains high-resolution, high-contrast information across the whole field of view at an ADF STEM image magnification of ~×0.3 M. In order to calculate the aberrations present in the probe-forming lenses, successive pairs of images are recorded at over-focus and under-focus conditions for a tableau of probe positions. From such a data set the complete set of aberration coefficients to third order can be determined in an analogous fashion to that used for TEM correction and these values are used to apply appropriate voltages to the individual electron optical elements of the probe forming corrector.

Direct measurement of the aberrations present in the probe can also be made using a Ronchigram of an amorphous specimen recorded with a large condenser aperture (~100 mrad) to enable inspection of the size and symmetry of the features at high angles surrounding the central zone which reflect the symmetry of the residual, higher-order aberrations [14] (**Figure 3**). The present microscope has the unique advantage that the probe can also be imaged *directly* to measure the final corrected state. The potential for using aberration-corrected probes with convergence semi-angles up to 30 mrad is currently being investigated, since such probes have been calculated to contain up to an order of magnitude more current than probes of similar size in an uncorrected instrument employing the same source at the same accelerating voltage. We intend to exploit this in both EELS and EDX analysis at ultra-high spatial resolution.

Initial Applications

The microscope is fitted with a bright-field and an ADF STEM detector below the in-column energy filter to allow unfiltered or energy-filtered STEM images to be acquired. A second HAADF detector is positioned *above* the in-column filter so that a stationary probe position can be selected from within a scan to allow an EELS spectrum to be acquired from a selected point without any disturbance due to the insertion or removal of any aperture or detector. The angular acceptance ranges of both sets of detectors can be varied by changing the magnification of the intermediate and projector lenses. **Figure 4(a)** shows an ADF image of a <110> Si crystal, in which individual atomic columns, spaced 0.136 nm apart in projection, are clearly resolved. The power spectrum calculated from this image (**Figure 4(b)**) indicates the transfer of the {226} reflections corresponding to a spacing of 0.082 nm.

As already noted commercial electron energy filters are now available in several distinct

configurations both with in-column [5, 9] geometries and as post-column imaging spectrometers [6]. In the instrument described here an isochromatic corrected, Ω-filter was chosen for both EELS, and for energy-filtered imaging and diffraction. **Figure 5(a)** shows a series of energy-filtered images of a Y-doped Si_3N_4/SiC ceramic, clearly revealing Y segregation at the

grain boundaries which is important in determining the mechanical and other properties of the material. **Figure 6** shows an example of a zero-loss CBED pattern recorded from a <111> Si single crystal, experimentally confirming a filter acceptance angle of > 80 mrad in the corrected state.
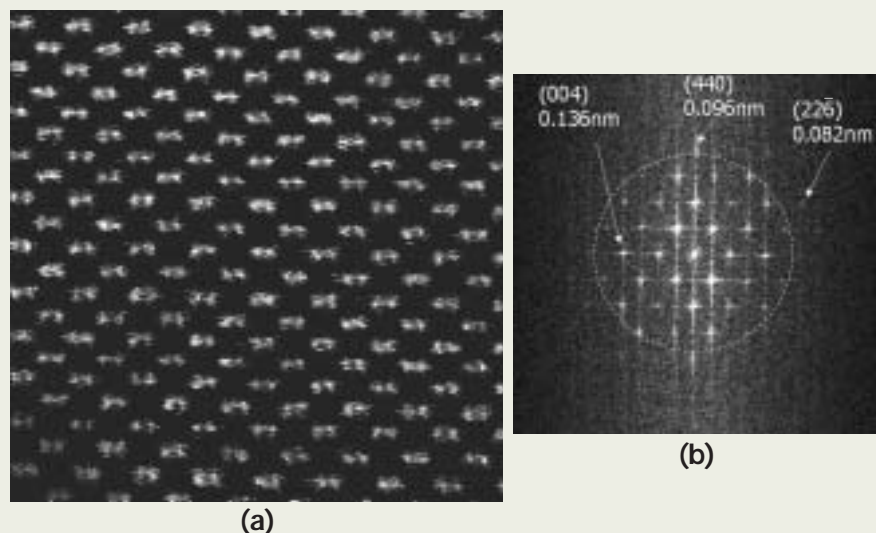
With the versatility offered by this unique

Fig. 4 (a) High resolution ADF STEM image of a <110> oriented Si crystal showing individual atomic columns separated by 0.136 nm. (b) Power spectrum calculated from (a) showing clear transfer of the {226} reflection corresponding to a spacing of 0.082 nm.

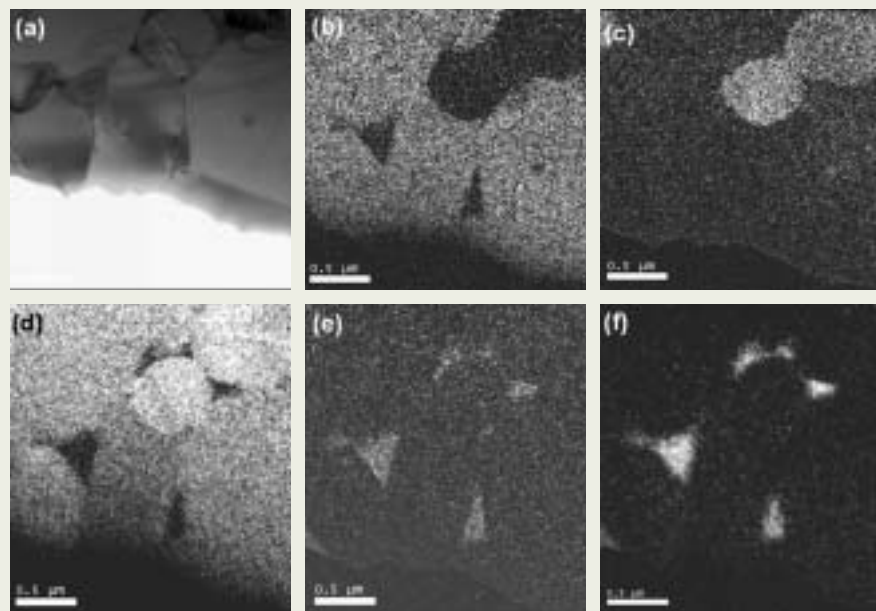Fig. 5 Energy filtered images of a Y-doped Si_3N_4/SiC ceramic showing enhanced Y concentration at the grain boundaries. (a) Zero loss bright field image recorded with a 5 eV energy selecting slit. (b) N map. (c) C map. (d) Si map. (e) O map. (f) Y map.

instrument at our disposal we are planning a wide range of experimental programs of which we present one example here. As part of an on-going study of complex oxides we are now in the position to resolve clearly both the cation lattice and the anion sublattice in many of these compounds. Combining the benefits of TEM aberration correction with indirect speci-men exit wave reconstruction from focal or tilt series [3] of aberration corrected images we can now achieve directly interpretable structur-al resolution below 0.1 nm. As an example, **Figure 7** shows the restored exit wave of a complex niobium oxide block structure in which *all* atom positions, including those of oxygen, are visible in the restored phase and in which structural information has been recov-ered to 0.09 nm. It has also been possible to record ADF STEM images of the same crystal (**Figure 7(b)**) which do not indicate any notable segregation of cation species. We are currently extending these studies into further investigations of interstitial anion and cation distributions in these materials using both recovered specimen exit wave functions in combination with ADF STEM imaging.

Conclusions

A unique double aberration-corrected, energy-filtered analytical HREM/STEM has now been installed and tested at Oxford. Initial data from a range of materials has confirmed that it is capable of resolution below 0.1nm in both HREM and STEM modes and it is now being used in a wide range of applications in materi-als science.

Acknowledgements

Fig. 6 Energy filtered CBED patterns from Si <111> in both (a) uncorrected and (b) corrected states. In both (a) and (b) the energy selecting slit width is 4 eV.
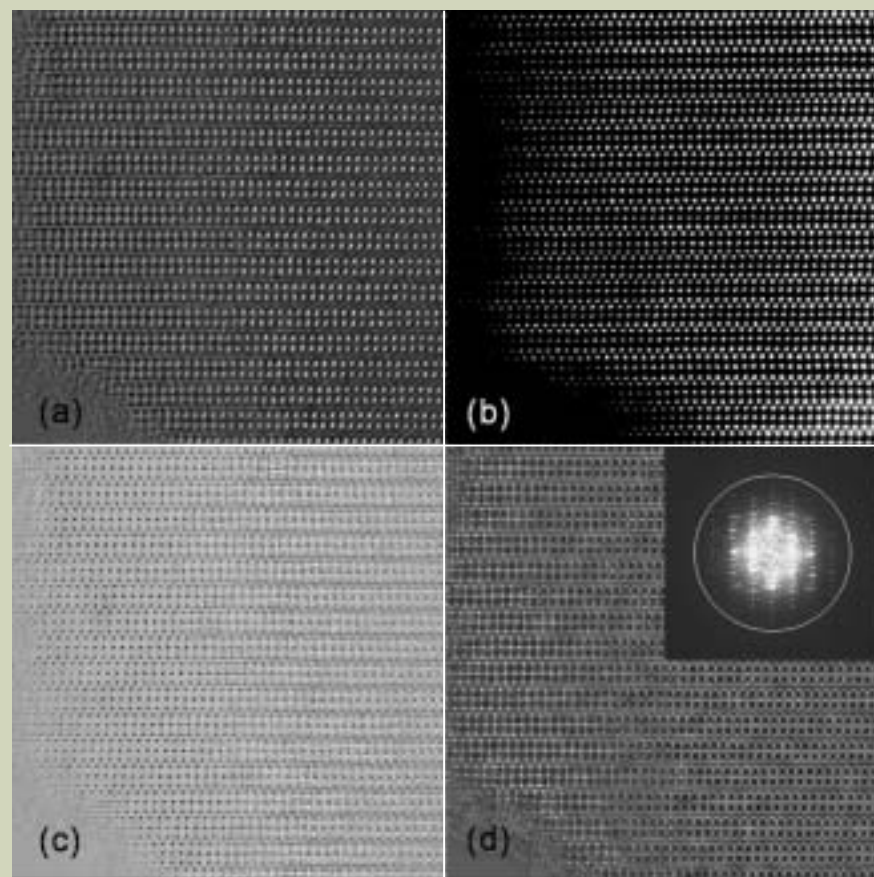
Fig. 7 (a) Conventional HREM image of the complex oxy fluoride $6Nb_2O_5 \cdot FeF_3$. (b) ADF STEM image of the same crystal as (a). (c) Modulus and (d) Phase of the specimen wave of the same crystal recovered from a 20 member focal series of images. The power spectrum of the restoration inset in (d) shows information transfer to 0.09 nm (with 0.1 nm marked with a circle) and in (d) both cation and anion lattices are clearly resolved.

References

[1] J. L. Hutchison, R. C Doole, R. E. Dunin-Borkowski, J. Sloan and M. L. H. Green.: *JEOL News*, **34E**, 10 (1999)

[2] T. Honda, T. Tomita, T. Kaneyama and Y. Ishida.: *Ultramicroscopy*, **54**, 132 (1994)

[3] A. I. Kirkland and R. R. Meyer.: *Microscopy and Microanalysis*, **10**, 1 (2004)

[4] M. Lehmann and H. Lichte.: *Microscopy and Microanalysis*, **8**, 447 (2002)

[5] K. Tsuno, T. Kaneyama, T. Honda and Y. Ishida.: *Nucl. Instrum. Methods*, **A427**, 187 (1999)

[6] O. L. Krivanek, A. J. Gubbens, N. Dellby and C. E Meyer.: *Microsc. Microanal. Microstruct*, **3**, 187 (1992)

[7] M. Haider, H. Rose, S. Uhlemann, E. Schwan, B. Kabius and K. Urban.: *Ultramicroscopy*, **75**, 53 (1998)

[8] H. Rose.: *Optik*, **85**, 19 (1990)

[9] M. Tanaka, K. Tsuda, M. Terauchi, K. Tsuno, T. Kaneyama, T. Honda and Y. Ishida.: *J. Microsc*, **194**, 219 (1999)

[10] O. Scherzer.: *Optik*, **2**, 114 (1947)

[11] F. Zemlin.: *Ultramicroscopy*, **4**, 241 (1979)

[12] W. O. Saxton.: *J. Microsc*., **179**, 201 (1995)

[13] O. L. Krivanek, N. Delby and A. R. Lupini.: *Ultramicroscopy*, **78**, 1 (1999)

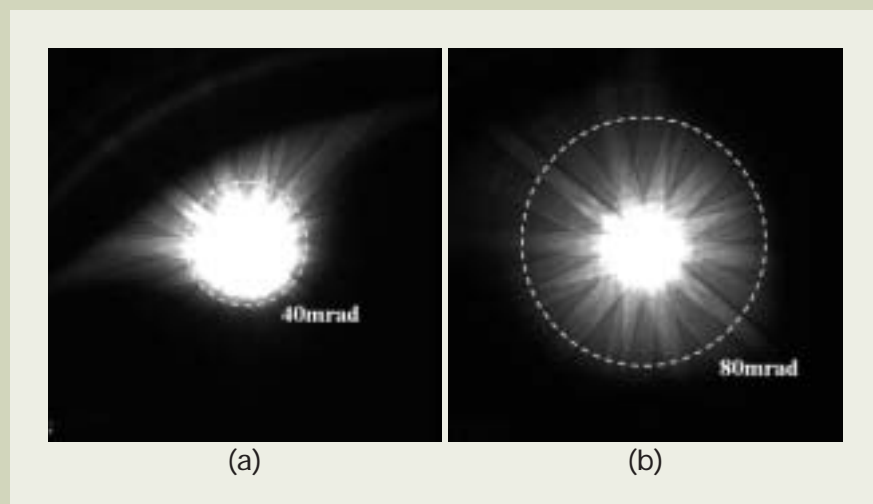[14] J. M. Cowley.: *J. Electron Microscopy Technique*, **3**, 25 (1986)

Variable Magnification of Electron Holography for Junction Profiling of Semiconductor Devices with Dual Lens System on JEOL JEM-2010F

Y. Y. Wang[†], M. Kawasaki[††], J. Bruley[†], M. Gribelyuk [†], A. Domenicucci[†] and J. Gaudiello[†]

[†]IBM Microelectronic Division
[††]JEOL USA, INC.

Dual lens electron holography with wide ranges of field of view and spatial resolution suitable for semiconductor device characterization is summarized. The electron optical configuration utilizes two objective lenses. The first objective lens forms a virtual image of the sample and the second objective lens focuses the virtual image at an intermediate image plane beyond the electron biprism in the form of the hologram. Adjusting the magnification of the objective lenses and the voltage applied to the biprism provides a field of view between 100 and 1,000 nm and a fringe spacing between 0.5 and 10 nm with a fringe contrast (10%-30%) usable for electron holography. The method allows fringe width and spacing relative to the object to be varied independently from the fringe contrast, resulting in holograms with both high spatial resolutions and high signal-to-noise ratios.

Introduction

Recent scaling in semiconductor device manufacturing down to sub-micrometer level (20-100 nm gate length) requires two dimensional electrical junction mapping at a high spatial resolution (less than 1 nm). Off-axis electron holography in a TEM has been successfully used to produce 2-D potential maps of semiconductor device at a spatial resolution from which junction positions can be inferred [1-3]. The potential maps are derived from phase information which is extracted from the interference pattern generated by overlapping electrons which have passed through the semiconductor sample with the electrons which have not. The overlap is accomplished by using an electron biprism (**Fig. 1**). The width of the overlap, the interference fringe spacing, and the fringe contrast are the key holographic parameters which determine the field of view, spatial resolution, and sensitivity of the resultant potential maps.

The requirements of electron holography to inspect the current generation of semiconductor devices are (1) an overlap width in the range of about 100 to 1000 nm for an adequate field of view (FOV), (2) fringe spacing between 0.5 and 10 nm for meaningful spatial resolution, (3) visibility of the fringe contrast (10-30%) for useful signal to noise ratio, and (4) adjustability of both the overlap and the fringe spacing relative to the sample for flexibility.

Under the "commonly used single lens mode", the JEOL JEM-2010F and JEM-3000F FETEMs can achieve two separate FOV ranges from 10 nm to 100 nm and 2 µm to 5

µm, depending on whether the objective lens or objective minilens is excited, respectively [4, 5]. As shown in Fig. 1a, when the lens further away from the sample (OM) is used, the magnification of the image is small, which results in large field of view and low spatial resolution relative to the sample. When the lens close to the sample is used (Fig. 1b), the magnification of the sample is large, which leads to smaller field of view and higher spatial resolution. Unfortunately, semiconductor junction potential mapping requires fields of view and spatial resolutions in the gap between these two ranges.

In this work, we summarize a method of using the two objective lenses on a JEOL JEM-2010F simultaneously to provide a continuously varying magnification of the sample at the intermediate imaging plane. This dual lens operation allows electron holography to be performed from low to high magnification and provides the FOV and fringe spacing necessary for two-dimensional (2D) junction mapping of semiconductor devices [6].

Background

In order to understand the dual lens system in this report, we briefly describe, the basic setup of the microscope, the principles of electron holography, and the basics of dual lens electron optics.

Microscope setup for electron holography

The JEOL JEM-2010F used in this work had a standard lens configuration and was fitted with a Gatan Imaging Filter (GIF). Three condenser lenses preceded objective lens (an ultrahigh resolution pole piece). The objective minilens below the main objective lens was followed by four lenses: I1, I2, I3, and P,

which completed the magnification process. A retractable electron biprism manufactured by JEOL was positioned between the objective minilens and the first intermediate lens (I1). The biprism consisted of a 0.5 µm diameter platinum wire positioned between two ground electrodes. In the present work, I1 was turned off and the intermediate image plane was set below I1. The electron hologram formed at this plane was magnified by the remaining lenses and recorded on the GIF CCD camera to gain the extra magnification necessary for adequate sampling. Alternatively, the CCD device in the camera chamber could be used to record the holograms after adjustment to the biprism position.

Basic principle of electron holography

To form electron holograms, a positive voltage is applied to the biprism wire, while the electrodes are grounded, which causes one beam to split into two beams interfering with each other. As illustrated in Fig.1, the off-axis electron hologram interference pattern can be thought of as being formed from two virtual sources, S_1 and S_2, of finite size (δ) positioned above the biprism and separated by a distance d. The fringe spacing, σ_i, and fringe width, W_i, at the image plane were described by Litchet as [7, 8]:

$$\sigma_i = \frac{\lambda}{2\gamma_o V_b}\left(1+\frac{b}{a}\right) \qquad (1)$$

and

$$W_i = 2\gamma_o V_b b - 2r_b\left(1+\frac{b}{a}\right) \qquad (2)$$

where a is the distance between the virtual sources and biprism position, b is the distance between image plane and the biprism position, λ is the wavelength of the electron beam, and V_b is the biprism voltage, γ_0 is a constant related to microscope setup, and r_b is the radial of

[†]2070 Route 52, Mail Stop 40E, Hopewell Junction, NY 12533-6531, USA
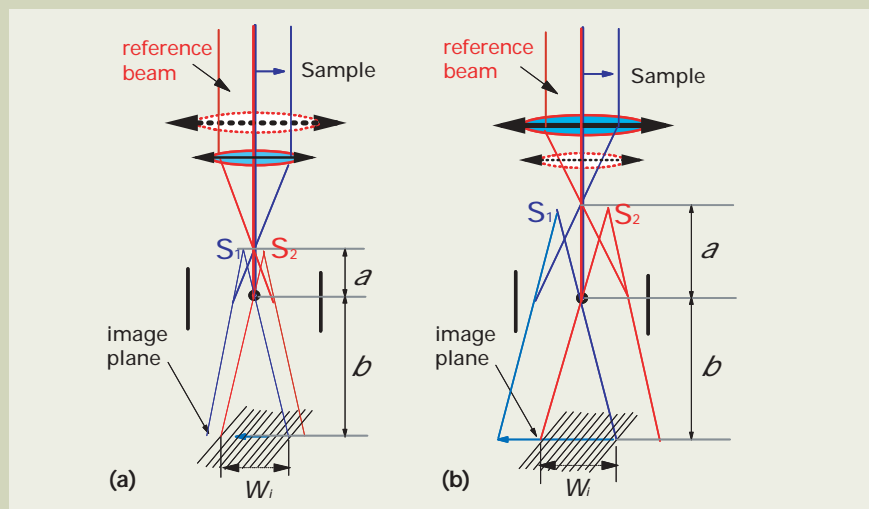E-mail :wangyy@us.ibm.com

Fig. 1 Electron hologram formation using a single lens in a dual lens imaging system. The interference pattern with fringe spacing, σ_i, and fringe width, W_i, is formed by two virtual sources, S_1 and S_2.
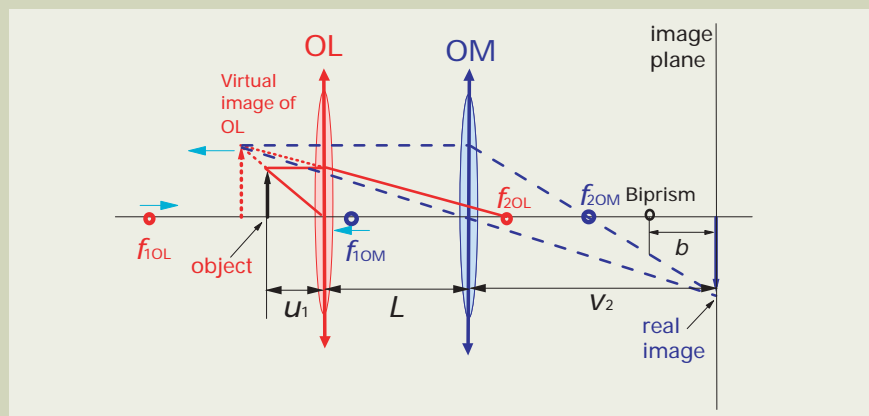

Fig. 2 Ray diagram of the dual lens system for electron holography. Light blue arrow indicates the movement of the focal points of OM and OL in order to keep the final image unchanged.
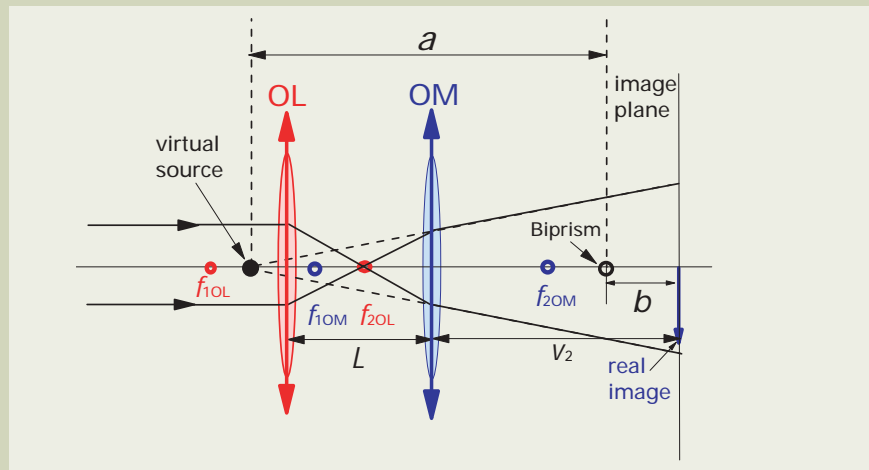

Fig. 3 Virtual source position for the dual lens system. The final virtual source position is the imaging position of the second focal point of the first lens through the second lens. The diagram is only for the purpose of illustration, it does not represent the actual scale of a and b.

biprism wire [8, 9]. The fringe spacing, σ_{obj}, and width, W_{obj}, relative to the object, can be expressed as follows:

$$\sigma_{obj} = \sigma_i / M_{obj} \qquad (3)$$

and

$$W_{obj} = W_i / M_{obj}, \qquad (4)$$

where M_{obj} is the magnification of the imaging lens (es). The above equations show that the magnification is a major factor which determines the fringe spacing and width relative to the object, and hence a major factor in determining the FOV and spatial resolution of the hologram.

Fringe contrast is another important param-

eter in electron holography and can be written as : [6]

$$\eta = \frac{I_{max} - I_{min}}{I_{max} + I_{min}} = \frac{sin(\beta)}{\beta} \qquad (5)$$

where

$$\beta = \frac{2\pi\delta}{\lambda} \frac{\gamma_{ob}}{a+b} V_b \qquad (6)$$

The fringe contrast, along with the electron dose determines the minimum detectable voltage in the potential maps derived from electron holograms. Based on Eqs.(5) and (6), larger biprism voltage leads to larger fringe width and smaller fringe spacing, both preferred for most analyses. However, fringe contrast decreases with increased biprism voltage due to the finite size of the electron source, as indicated by Eqs.(5) and (6). The control of fringe width, spacing, and contrast by varying biprism voltage alone limits the operational range of a TEM set up for electron holography. By continuously altering the magnification of imaging lenses, (see Eqs.(3) and (4)), the fringe width (W_{obj}) and spacing (σ_{obj}) can be changed without significantly degrading fringe contrast, widening the operational range for electron holography.

Optical ray diagram for the dual lens method

For a single imaging lens system, with both object position and image plane fixed, the only way to vary the magnification is adjusting the lens position with an appropriate focal length. As mentioned earlier, if the lens is close to the object, the magnification is large, and if the lens is far away from the object the magnification is small. However, with two or more lenses, the magnification can be changed without changing the position of the lenses by varying the focal length of the lenses.

For the magnetic lenses used in most transmission electron microscopes, the focal length is related to the lens voltage according to the following equation [10],

$$f = \frac{K}{V^2} \qquad (7)$$

where K is a constant for a given lens, and V is the voltage applied to the lens. Increasing the lens voltage (increasing the strength of the lens) decreases its focal length.

Figure 2 illustrates the combined operation of the objective lens and objective minilens which is the basis for this work. The voltage of the objective lens (OL) is set so that the position of the object is behind the first focal point F_{1OL}, but before the lens thereby forming a virtual image of the object. The second objective lens (OM) is used to project a real image of the OL virtual image onto the intermediate image plane beyond the biprism. As shown in Fig. 2, when the focal point of OL gets closer to the sample, the virtual image moves further away from the sample and is magnified. In order to refocus the virtual image onto the same image plane, the focal length of OM is increased (strength of OM decreases) to compensate the movement of the virtual image position. So the magnification of the sample at the image plane, M_{obj}, can be adjusted by varying the focal length of the first objective lens (OL) to give a virtual image of variable size which is refocused to the intermediate image plane by the objective minilens (OM).

The virtual source of electron holography is another important parameter which determines the fringe spacing and fringe contrast, as indicated in the above equations. In a single lens operation with parallel beam illumination, the virtual source position is at the back focal plane of the lens. However, under dual lens operation, the virtual source position depends on the lens condition used. As shown in **Fig. 3**, "a" is determined by the projection action of the objective minilens. Since "a" is variable in the dual lens mode, the fringe spacing, σ_i, will depend not only on the biprism voltage, V_b, but also on the OL and OM excitations, even with the fixed imaging plane (fixed "b").

Experimental Results and Discussions

Figures 4 and **5** summarize experimental results for fringe width, fringe spacing, and fringe contrast. In Fig. 4, the fringe spacing, width, and contrast are plotted against biprism voltage with different OL values. The expected trends of decreasing fringe spacing and increasing fringe width with increasing biprism voltage are observed. Also, as expected, a decreasing fringe spacing for increasing OL excitation is shown in Fig. 4b. The graphical results show that the range of values for field of view and fringe spacing necessary for semiconductor characterization are achieved. Moreover, although the fringe contrast is strongly dependent on the biprism voltage, it is only weakly dependent on the OL excitation. In all, the data shows that the dual lens mode leads to a large operational space for electron holography without sacrificing fringe contrast, which determines the signal to noise ratio in the amplitude and phase (potential) maps derived from the electron holograms.

In Fig. 5, the fringe spacing and width relative to the object are plotted against OL excitation at a constant biprism voltage (20 V). The fringe spacing and width decrease as OL excitation increases, but at different rates. In addition, fringe spacing levels off with OL above 3.0 V. The difference in these trends can be understood in light of Eq.(1) through Eq.(4) above. The fringe width in the object plane is inversely dependent on the magnification of the imaging lenses, when the biprism voltage is fixed and the imaging plane, "b", is fixed. So increasing M_{obj} (increasing OL excitation) causes a continuous decrease in W_{obj}. However, the fringe spacing, σ_{obj}, depends not only on M_{obj}, but also on the virtual source position, "a". When OL is below 3.0 V, the fringe spacing decreases faster than the fringe width does. This is due to the fact that f_{2OL} quickly approaches the position of f_{1OM} as OL is increased from 1.0 V to 3.0 V (see Fig. 3). This, in turn, causes the virtual source to move away from the biprism, which leads to a larger "a". This larger "a" coupled with a larger M_{obj} is responsible for the sharp drop in σ_{obj}. When OL is above 3.0V, the refocusing of the image by OM causes f_{2OL} and f_{1OM} to diverge and leads to a smaller "a". The fringe spacing decreasing rate slows down due to the competing effects of an increasing M_{obj} and a smaller "a" (Eq.(1)).

As mentioned above, dual lens operation results in a wide range of fringe spacing and fringe width at a fixed intermediate image

plane. However, if warranted, the image plane can also be changed with dual lens operation by varying I1 or I2 in combination of OM. The adjustment of the image plane leads to the variation in "b", which provides additional parameters for further widening the FOV and spatial resolution range while keeping the fringe contrast at a usable range. Another way to vary "b" is to physically move the biprism position. For instance, lowering the biprism position leads to a smaller "b" and a larger "a" for a similar lens configuration.

Example

To demonstrate the flexibility of the dual lens method, we obtained electron holograms of pFET devices with poly silicon gate lengths

of 220 nm and 70 nm on bulk Si and on silicon on insulator (SOI) substrates, respectively. Samples were prepared by mechanically polishing to an initial thickness of ~400 nm and using ion milling to reduce the thickness to a final value of ~200-300 nm. Samples were coated on one side with ~20 nm of carbon to reduce the effects of charging. Two holograms were obtained during the operation using the biprism voltage of 20 V: one is the hologram with the sample and the other is the hologram without sample, known as a reference hologram. Phase and amplitude maps were obtained from these two holograms through Fast Fourier Transformation and inverse Fast Fourier Transformation (FFT). Potential can be extracted from the phase map. Potential maps were reconstructed using the ASU plug-
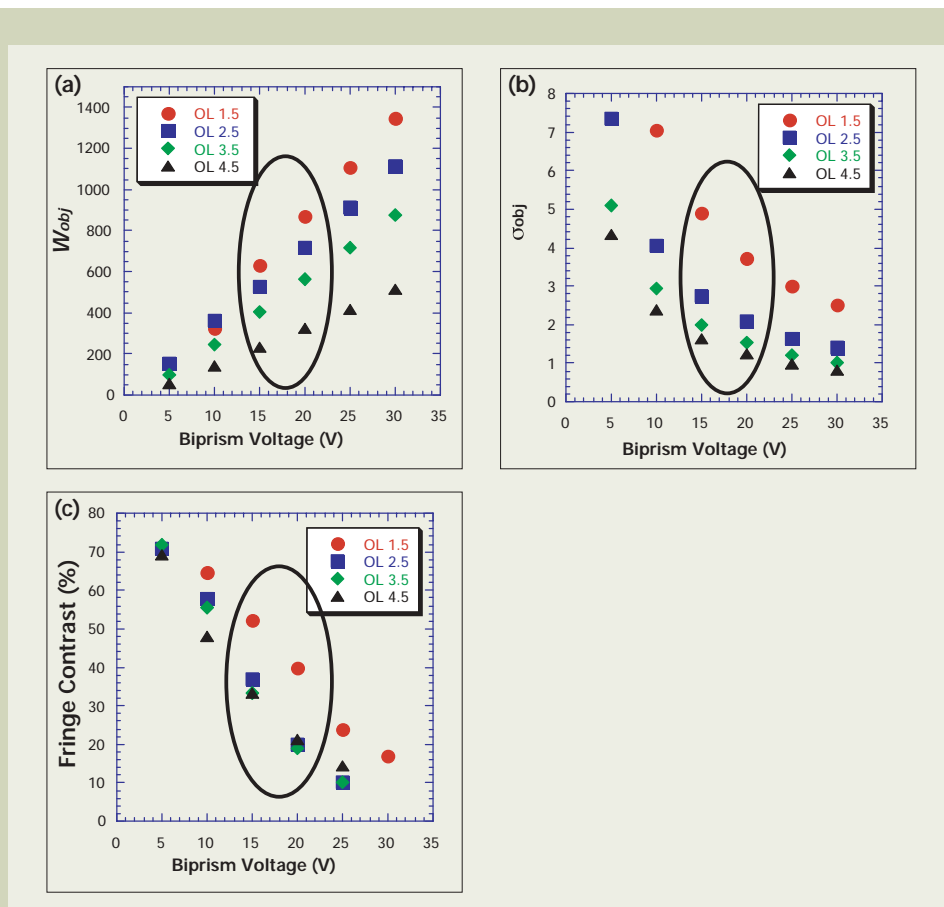

Fig. 4 Fringe spacing (a), width (b), and contrast (c) vs biprism voltage with different OL value. Red circle is for OL 1.5, blue square for OL 2.5, green diamond for OL 3.5, and black triangle for OL 4.5. The circled region is where the optimal operational condition for electron holography is based on fringe contrast value.
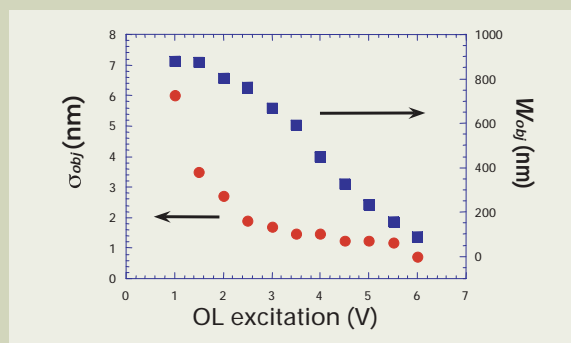

Fig. 5 Fringe spacing, σ_{obj} (circle), and fringe width, W_{obj} (square), relative to the object are plotted against OL excitation with a constant biprism voltage of 20 V.

ins to Gatan Digital Micrograph [2].

Contour potential maps for the two devices are shown in **Fig. 6**. Both devices exhibit symmetric doping profiles and the expected 1.0 V potential drop across the junctions. The intensity of the maps near the sides of the gates (side wall spacers and CoSi2) changes sign abruptly due to phase wrapping. As summarized in **Table 1**, both σ_{obj} and W_{obj} can be scaled by simply varying OL excitation without losing fringe contrast. This allows the characterization of different size devices with the same signal sensitivity.

In high performance CMOS logic devices, low dose ion implants are placed between the channel and the low resistance (high dose) source/drain regions. In Fig.6b, the upper curved portion of the P-N junction on either side of the device channel represents the result of such a low dose implant, which is clearly visible due to the high spatial resolution in the hologram from which the potential map was reconstructed.

Another example is the junction mapping on narrow Si diffusion region (shown in **Fig. 7a**), which is usually perpendicular to the gate. In typical device layouts, this is usually the contact region or the region which makes connection between one device and another. Sometimes, a high leakage current is observed from the contact region to the substrate in this narrow Si diffusion region. In order to understand the leakage path, a junction map was acquired by electron holography (**Fig. 7b**). A P-N junction is clearly shown in the potential map. Near the edge of the Si diffusion region,

the junction is slightly curved upwards towards CoSi2. The slight displacement of the junction near the edge of insulator could be due to either the implant shadowing or B loss at the Si to SiO2 interface. Without high spatial resolution, it would be difficult to detect this small shift of the junction near the edge of Si diffusion region.

Conclusion

Dual lens electron holography with wide range of field of view and spatial resolution for semiconductor junction characterization is reported in this paper. The method has the advantage of allowing the fringe width and fringe spacing in electron holograms to be changed independently from the fringe contrast. This results in better spatial resolution and voltage sensitivity for the characterization of semiconductor devices using 2-D potential mapping. To demonstrate the utility of the method, three potential maps with different spatial resolution were reported in this paper.

Fig. 6 6a and 6b are potential maps of pFET devices made with the dual lens method with different spatial resolution.

Table 1 Experimental conditions of two potential maps shown in Fig. 6b and 6a.

	220 nm Gate (Fig. 6a)	70 nm Gate (Fig. 6b)
OL voltage (V)	2.0	3.5
Fringe Spacing, σ_{obj} (nm)	2.5	1.4
Fringe Width, W_{obj} (nm)	800	575
M_{obj}	5.7	14.8
Contrast (reference hologram)	10%	11%
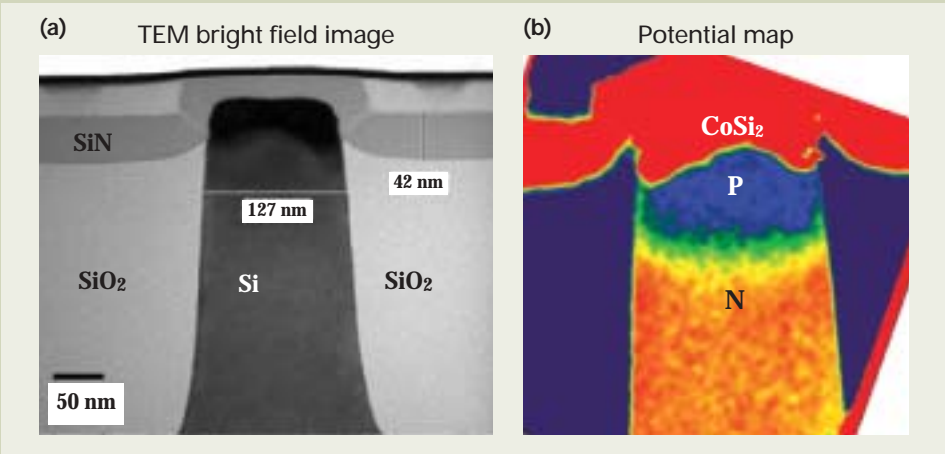
Fig. 7 P-diffusion to N-well profile for narrow Si. At the edge of Si near SiO2 wall, the junction is slightly tilted towards CoSi2.

References

[1] W. D. Rau, P. Schwander, R. H. Baumann, F. H. W. Hoppner and A. Ourmazd.: *Physical Review Letters,* **82**, 2614 (1999)

[2] M. R. Mccartney.: *Ultramicroscopy*, **53**, 283 (1994)

[3] M. A. Gribelyuk, M. R. McCartney, J. Li, C. S. Murthy, P. Ronsheim, B. Boris, J. S. McMurray, S. Hedge, and D. J. Smith.: *Physical Review Letters*, **89**, (2002)

[4] R.E. Dunin-Borkoski, unpublished results.

[5] M. A. Schofield, Y. Zhu, L. Wu, V. V. Volkov, and M. Malac.: JEOL news-electron optics instrumentation, Vol. 36E No.1, p.2 (July 10, 2001)

[6] Y. Y. Wang, J. Bruley, M. Gribelyuk, A. Domenicucci, J. Gaudiello, M. Kawaski, to be published in *Ultramicroscopy*; Y. Y. Wang, M. Kawaski, J. Bruley, A. Domenicucci, M. Gribelyuk, and J. Gaudiello, IBM and JEOL USA patent application, submitted to US patent office.

[7] H. Litchet.: *Ultramicroscopy,* **64**, 79-86 (1996)

[8] W. D. Rau and H. Litchet.: Introduction to Electron Holography, Edited by E. Volk, L. F. Allard, and D.C. Joy, Kluwer Academic/Plenum Publishers, New York, p.208 (1999)

[9] H. Litchet.: Advances in Optical and Electron Microscopy, Vol.12, Academic Press, p. 25 (1991)

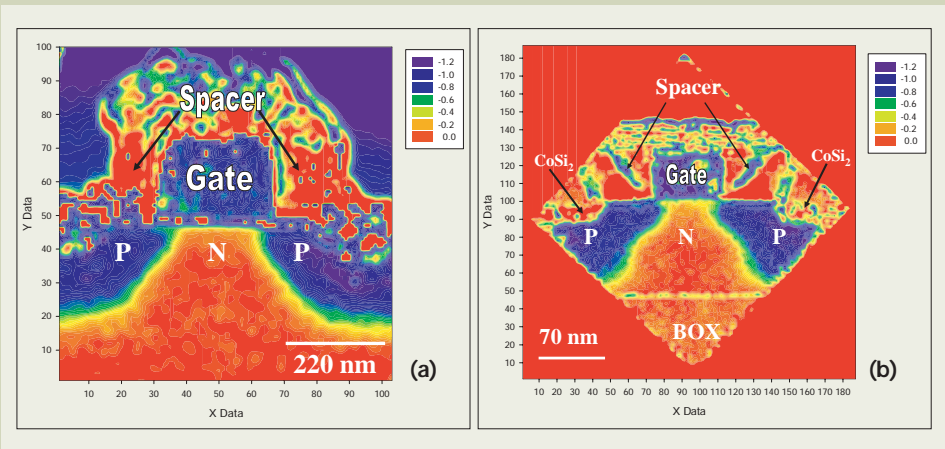[10] L. Reimer.: Transmission Electron Microscopy, Springer-Verlag, Berlin, p.59 (1989)

The Electron Backscatter Diffraction Technique – A Powerful Tool to Study Microstructures by SEM

Stefan Zaefferer

Max-Planck-Institute for Iron Research

In the last 10 years the electron backscatter diffraction (EBSD) technique has developed into a powerful tool for the crystallographic analysis of materials in the scanning electron microscope. In particular the emergence of computer algorithms for the fully automated analysis of diffraction patterns has pushed the technique to develop into a new kind of scanning microscopy technique, known as "orientation imaging microscopy, OIM[1]" or "automatic crystal orientation mapping, ACOM". The ACOM technique is based on the consecutive acquisition of electron diffraction patterns obtained from every point of a scan grid on a flat surface of a steeply inclined sample in the SEM. The automatic analysis of these EBSD patterns yields for every scan point the crystallographic orientation and phase and a value indicating the quality of the diffraction pattern. From these data the microstructure of the scanned area can be reconstructed. The resulting crystal orientation maps give a vast amount of information on the sample, including kind and distribution of different phases, size, form and defect condition of grains, kind and position of grain boundaries, local crystal orientation and misorientation distribution (texture) and others more. Furthermore, EBSD can be used to investigate the structure of crystals, i.e. lattice symmetry and lattice parameters and may therefore take over a large amount of crystallographic work that was performed before by TEM. The EBSD technique usually requires less complicated sample preparation and allows the observation of much larger areas, yet with a quite high spatial resolution. Although the EBSD technique can be applied with good success on a standard tungsten filament SEM it profits enormously - in terms of spatial resolution and orientation accuracy - from using a thermal field emission gun instrument with a high beam current. The present text briefly describes some of the physical fundamentals and the practical set-up of the technique before it presents a couple of application examples that illustrate some of its possibilities. All examples stem from problems of physical metallurgy – the author's field of expertise – although the technique is also intensively applied to the study of non-metallic, crystalline materials like semiconductors, ceramics and minerals.

Introduction

Electron backscatter diffraction patterns which are obtained from bulk samples have lots of similarities with Kikuchi diffraction patterns obtained from thin foils in the transmission electron microscope. **Figure 1a** displays a typical pattern: It consists of bright bands (the so called Kikuchi bands), on a relatively strong background. Each of the bands corresponds to a set of lattice planes in the crystal and from the angles between the bands and from their width the Miller indices of these lattice planes can be determined. Finally, from indexed bands the crystal orientation and phase can be calculated.

EBSD patterns were first observed in the scanning electron microscope by Venables and Harland in 1973 [1]. However, the technique did not receive much attention until Dingley [2] developed a computer program for manual indexing of diffraction patterns and replaced the photographic film that was used for pattern registration by a set-up of a phosphor screen and a TV camera. In 1992 Krieger-Lassen [3, 4] introduced a special software algorithm, the so-called Hough transform, for the automatic detection of the Kikuchi bands in EBSD patterns. Together with an automatic indexing algorithm he created a computer program for the fully automated determination of crystal orientations from EBSD patterns. This development enabled Adams *et al*. in 1993 to develop a new way of scanning microscopy, the "orientation imaging microscopy (OIM)" [5]. The publication of this work marks the breakthrough of the technique. The emergence of several commercial and non-commercial systems and an increasing number of users stimulated a strong development of both, software and hardware. Several recent texts give a good overview on the current state of the art, e.g. [6, 7]. The most complete is the collection of articles in the book of Schwartz *et al*. [8]. Overviews on still more recent developments are given by Humphreys [9] and Dingley [10]. It should be mentioned that EBSD – particularly in combination with energy dispersive x-ray spectroscopy (EDX) – also becomes a more and more used tool for crystallographic phase determination [11-13].

Physical and Technical Background

In the classical image EBSD patterns are created – as Kikuchi patterns in the TEM – in a two step process. In the first step the electrons entering into the crystal are quasi-elastically but incoherently scattered. This process can be regarded as the formation of an electron source inside of the crystal – electrons travelling in all directions, emerging from a small area in the crystal. These electrons may now be diffracted at the crystal lattice according to the Bragg equation. It can be easily shown that the loci of diffracted electrons emerging from a point source inside of the crystal are pairs of cones, centred about the lattice plane normal vectors with an opening angle of $180° - 2\theta$ and an angle of 2θ between them, as it is shown in **Fig. 2a**. Since the Bragg angle θ is rather small (in the order of 1° for 15 kV accelerating voltage) the cones are very large and each pair of cones thus intersects an observation screen, positioned somewhere tangential to the propagation sphere of the scattered electrons, in almost straight and parallel pairs of lines, the so-called Kikuchi lines. The distance between the two lines is approximately proportional to $\tan(\theta)$ while the position of their centre line can be understood as the gnomonic projection of the diffracting lattice plane onto the observation plane. The simple geometrical image of EBSD presented here does, of course, not account for any details in the pattern. These are treated, for example, in the paper by Wilkinson and Hirsch [14].

In order to observe the diffraction pattern one must allow the diffracted electrons to

Max-Planck-Str. 1 D-40237 Düsseldorf, Germany
E-mali : zaefferer@mpie.de

Fig. 1 Patterns of different quality obtained from an as-cast niobium sample. a) High resolution EBSD pattern (915 × 915 pixel). Exposure time 7 s, with background subtraction. b) Raw EBSD pattern for high speed mapping. Resolution 112 × 112 pixel, exposure time 15 ms, before background subtraction.

Fig. 2 a) Scheme for the formation of Kikuchi bands by diffraction of electrons from a point source inside of the crystal. b) Geometrical set-up of sample and pattern detector in the SEM. Note that the Kikuchi band displayed in a) corresponds to just one of the lines visible in the diffraction pattern in b).
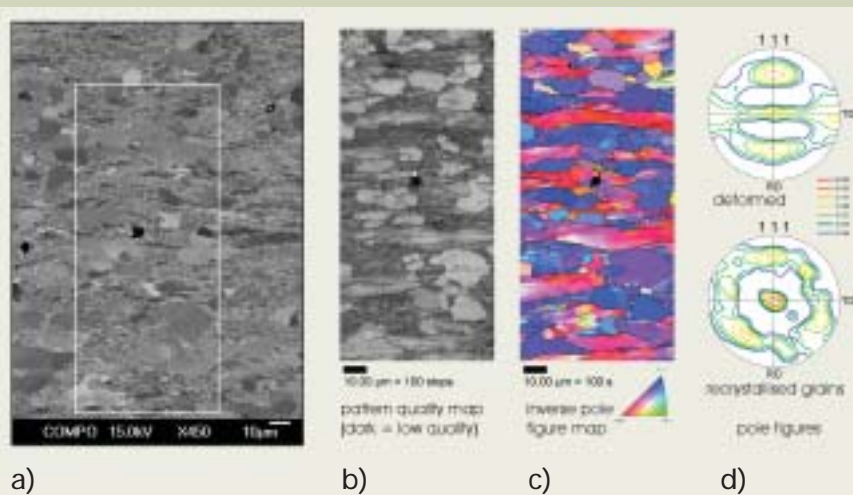
Fig. 3 Example of ACOM on a microstructure of a partially recrystallised IF steel. a) Electron channeling contrast image obtained with the backscattered electron (BSE) detector from the untilted sample. b) Diffraction pattern quality map of the observed area. c) Crystal direction map indicating the crystal directions pointing parallel to the sample normal direction (ND). Grain boundaries with misorientation larger than 15° are marked as black lines. d) (111) pole figures of the deformed and recrystallised partition of the sample, showing that recrystallisation strongly supports crystal orientations with (111) ∥ ND (centre of pole figure). (Courtesy of I. Thomas).

escape from the crystal. To this end the sample is strongly tilted, usually to about 60° or 70°. The observation screen, a retractable transparent phosphor screen, is positioned close to the tilted sample (usually between 20 and 40 mm away from the beam-sample intersection) as indicated in **Fig. 2b**. The phosphor screen is observed by a highly light-sensitive camera which transmits the acquired image to a computer for further processing. The same computer also controls the beam positioning and - in some cases - the beam focussing necessary for automatic crystal orientation mapping (ACOM). For ACOM the electron beam is moved stepwise over the sample and at every position a pattern is acquired and analysed. A typical result obtained by ACOM is presented in **Fig. 3**. The figure shows the microstructure of a partially recrystallised IF steel ([15]) as observed by electron channeling contrast and by ACOM. In the crystal orientation map similar colours stand for similar crystallographic directions pointing towards the sample normal. Grains with uniform orientations (i.e. recrystallised grains) appear in uniform colour while grains with internal orientation gradients show changing colours. In this way grain form and size, recrystallised and unrecrystallised areas, type of grain boundaries and the local texture (here displayed in form of pole figures separated for deformed and recrystallised areas) can be easily recognised and quantified. It should be mentioned that ACOM is – compared to other scanning techniques in the SEM – a rather slow technique. Although the map displayed in Fig. 3 has been acquired with about 30 measurements per second the complete map still requires several hours of measurement.

Experimental Requirements for EBSD

The quality of an EBSD measurement and the capabilities of an EBSD system are measured by means of a couple of parameters. These are the signal-to-noise ratio (SNR) observed in the pattern, the pixel resolution of the pattern, the spatial resolution and the acquisition and processing speed of the system. These parameters are controlled by a number of factors, including, under others, the sample (sample preparation, material, microstructure), the microscope (emitter type,
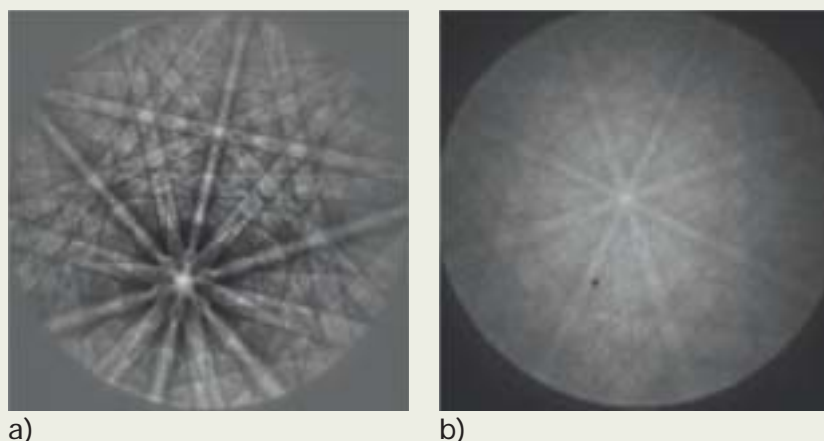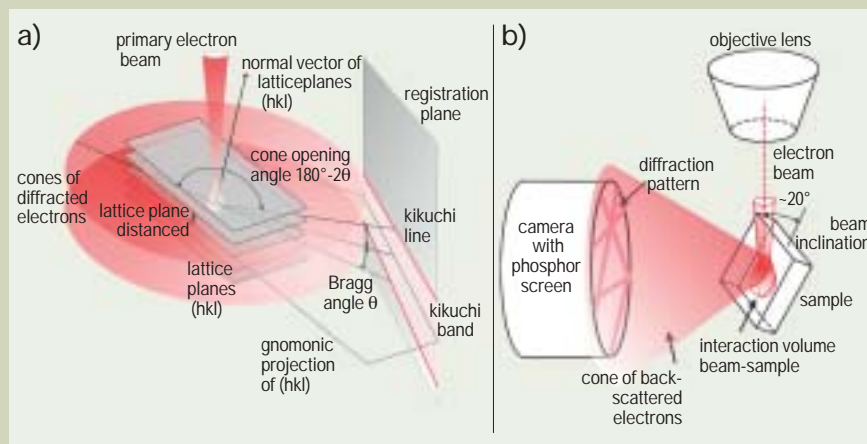
accelerating voltage, beam size and current, mechanical and electronic stability), the EBSD camera (light sensitivity, pixel resolution, read-out time) and the EBSD software (processing speed, robustness). In the following some of these factors are briefly discussed. A detailed treatment can be found in the work of Humphreys [9].

Sample conditions

In order to avoid shadowing the sample surface should be relatively flat. Since EBSD is a very surface sensitive technique (the signal stems, depending on the material, from a layer of less than ten to tens of nanometre thickness), it is, however, more important that the surface is free of any deformation layer created by mechanical polishing. Best polishing results are obtained by chemical or electrochemical procedures. However, hard materials can often also be prepared by a final polish with 50 nm-colloidal SiC. Difficulties almost always arise when multi-phase samples are to be prepared. In these cases often different polishing quality is obtained on different phases and surface reliefs may develop that disturb the acquisition of patterns. No universal preparation method can be given for these cases. Another important precondition for the sample is good electrical conductivity since a relatively high beam current is required to obtain clear patterns. On metals usually no problem arises as long as the sample is well contacted to the sample stage. Nevertheless, resin-mounted samples, even if they are well conductive, often lead to sample drift during longer measurements due to their reduced thermal conductivity. Non-conductive materials have to be coated with a thin layer of carbon (up to few tens of nanometres) or an even thinner layer (< 5 nm) of amorphous metal. The quality of an EBSD pattern (i.e. the SNR and the sharpness of the Kikuchi lines) also depend on the material observed. Generally, the quality increases with increasing atomic weight and increasing bonding forces of the material. Thus, usually, heavy metals show better patterns than light ones and covalently bonded materials show better patterns than those with metal bonding. Finally it must be mentioned that lattice defects (e.g. dislocations) disturb the formation of clear patterns. The higher the lattice defect density of the sample is, the worse the pattern quality is. This relationship, on the other hand, can be used to map the density of lattice defects in the sample.

Microscope

In principle, EBSD patterns can be obtained with every SEM. However, the quality of the obtained patterns and the achievable spatial resolution strongly depends on the microscope characteristics. Microscopes with tungsten filament deliver enough beam current but the beam spread is rather large. On the other hand, instruments with cold field emitter allow for a small beam size but the relatively small beam current as well as the reduced long-term stability are not optimum for EBSD. The best overall EBSD performance is obtained from a microscope with thermal field emission gun and high beam current, as it is the case, for example, with the JEOL JSM-6500F which offers a particularly high beam current at small

beam diameter due to its in-lens emitter. The high beam current allows reaching either a very high measurement speed at still acceptable noise level in the pattern (currently about 60 patterns per second can be acquired and analysed by the authors equipment) or the acquisition of very brilliant, detailed diffraction patterns at low speed (2 or more seconds of exposure time). Pattern examples for both conditions are displayed in Fig. 1. The small beam diameter is important to reach a high spatial resolution. Furthermore, the spatial resolution depends on the penetration depth of the beam into the material and is therefore influenced by the accelerating voltage and the investigated material. Humphreys [9] and Dingley [10] have made very detailed investigations on these parameters. Here we just mention that the spatial resolution in principle becomes better with decreasing accelerating voltage, however, currently an optimum is reached at about 15 kV. Lower voltages currently still cause problems with the sensitivity of the phosphor screen and the pattern analysis software. On iron the current author has determined a spatial resolution of approximately 30 nm at 15 kV using the JSM-6500F. On aluminum the resolution is significantly worse (values of 100 nm have been mentioned), on platinum values below 10 nm have been measured. A final point concerning the microscope is its mechanical and electronic stability. EBSD measurements require rather long measurement times (up to 12 hours for very large maps) with the stage at a highly tilted position. During this measurement time the beam current has to be stable and the beam position must be perfectly controlled. Furthermore, for high resolution measurements with step sizes of few tens of nanometres the stage drift must not exceed about 1 nm/min.

Camera

The EBSD camera is nowadays in most cases a digital, highly light-sensitive CCD camera. Often they are Peltier-cooled to reduce noise. Most cameras can be used in several binning modes, thus enhancing sensitivity and read out speed on cost of pixel resolution by comprising a certain number of pixels. In this way the camera may allow acquisition of highly resolved images (≈ 1000 × 1000 pixel) at slow acquisition speed or of low resolution images (≈ 100 × 100 pixel) with very high speed. Currently, some camera types are able to record and transmit more than 100 low-resolution images per second.

At the present state, it is certainly improvements of the camera which will allow the most significant improvements in terms of spatial resolution and SNR of an EBSD system. Phosphors with higher sensitivity for lower energy electrons, higher sensitivity of the chip, higher density of pixels and a flexible camera positioning in the chamber may be possible developments.

Software

A couple of commercial software packages are available, which partly rely on quite different software algorithms. Two parts in the measurement software are most essential for a reliable and robust measurement. The first is the line detection algorithm which uses the

already mentioned Hough transform. Several variations have been developed since the original work of Krieger-Lassen (e.g. [16]). Most of these are used for special cases, for example, for the precise detection of band width for the distinction of different phases or for indexing of complex crystal structures. A good control on the parameter of the Hough transform is an important feature. The second part is the indexing algorithm. The most important feature here is how the algorithm deals with false or imprecisely detected bands. Furthermore it is important how the algorithm deals with ambiguities (i.e. several possible orientation solutions). Values used to decide for the right solution are the number of votes that a certain solution receives for indexing of different band combinations or the angular deviations between recalculated and detected bands. It should be mentioned that a good indexing algorithm is able to enhance the physical spatial resolution of EBSD insofar as it allows to separate, with high confidence, the solutions stemming from the overlapping patterns of two neighbouring crystals.

Application Examples

The following chapter illustrates some of the capabilities of the EBSD and ACOM technique by means of two examples from physical metallurgy. The first, dealing with the problem of Goss texture formation in silicon steels mainly illustrates the possibilities to measure very large crystal orientation maps and gives an example how these data can be processed in order to extract important information from them. The second is an example on the combined application of ACOM and EDX elemental mapping to the investigation of the microstructure, phases and phase orientation relationship in an oxidation protection coating on a nickel-based superalloy. All measurements have been performed on a JEOL JSM-6500F SEM equipped with a DigiView digital EBSD camera (TSL/EDAX) and the OIM 3 (TSL/EDAX) software package.

The Goss texture formation in Si-steels

Silicon steel with 3 % Si is a soft magnetic material with low electrical conductivity that is mainly used in form of stacked laminations of sheets for electrical transformer cores. The easiest magnetisable crystal direction is the <100> direction and, in order to reduce magnetisation energy losses, one would like to have this direction parallel to the magnetic flux in the transformer core, as shown in **Fig. 4**. The required cube texture, {100}<001>[2], however, is technologically difficult to achieve. The best compromise between optimum texture and technological feasibility is the Goss texture, {110}<001>, which develops during secondary recrystallisation after a process consisting of warm rolling, cold rolling and primary recrystallisation [17]. The abnormal growth of Goss-oriented crystals, independently at different positions in the fine grained, weakly textured, primary recrystallised matrix is still one of the most surprising phenomena in physical metallurgy and has been subject of much debate in the last 60 years [18, 19]. **Figure 5** shows a growing Goss-oriented grain

in the recrystallised matrix. While the matrix grains have grain sizes in the order of 30 μm, the final Goss grains have sizes of several millimetre. It can be easily shown, that only 1 out of 1.000.000 matrix grains develops into a final Goss grain. In order to find these grains and, eventually, understand their particular properties a large number of grains has to be investigated and only the latest EBSD systems are able to perform the required amount of measurements. **Figure 6a** shows an EBSD map consisting of about 1.3 Mio. measurement points and about 60.000 grains. Many of these maps have been measured (each of which takes about 12 hours) in order to enhance the chance to find a vital Goss grain. What can be done with these mountains of data? One possibility is, to check whether Goss grains have any original size advantage. To this end the data are analysed by classifying the measured grains according to their grain size and to their angular deviation to the Goss orientation. This classification is displayed in **Fig. 6b**. The figure clearly shows, that there is no tendency of large grains to be close to the Goss orientation. Rather, large grains seem to have the same orientation distribution than the other grains. This conclusion, however, could be shown not to be correct: large grains have a certain preferred orientation, characterised by their <100> direction being parallel to the rolling direction of the material. Disregarding this result a size advantage of Goss grains could not be proofed [20] and we currently follow a different hypothesis for Goss grain growth.

The microstructure of superalloy oxidation protection coatings

Nickel-based superalloys are used as material for turbine blades in jet-engines. The material shows a microstructure that consists of a high volume fraction of cuboidal, coherent precipitations with $L1_2$ crystal structure (basic composition Ni_3Al) in a matrix with fcc structure. In order to obtain a high creep resistance 2nd generation superalloys are alloyed with important amounts of refractory elements like W, Ta, Mo and Re [21, 22] and turbine blades are often solidified as single crystals. The materials service temperature and life-time can be improved if an oxidation protection coating is applied to the surface for example by in-diffusion of aluminum in a process called pack-cementation [23]. The increased aluminum content close to the surface leads to a transformation of the $L1_2$ Ni_3Al phase into the more heat and oxidation resistant B2 NiAl phase. Unfortunately, the single crystal structure of the base material is not conserved in the coating. Instead, the coating shows a quite complex polycrystalline structure consisting of several layers with different composition, morphology and crystallographic texture [24, 25]. Furthermore, the increased Al content leads to precipitation of the refractory elements. The mechanical and thermal stability and quality of adhesion of the formed layer are strongly dependent on the details of the microstructure and texture and this can be perfectly investigated by EBSD, combined with EDX for the determination of elemental composition. Both techniques can be applied simultaneously but the EDX results from tilted samples usually
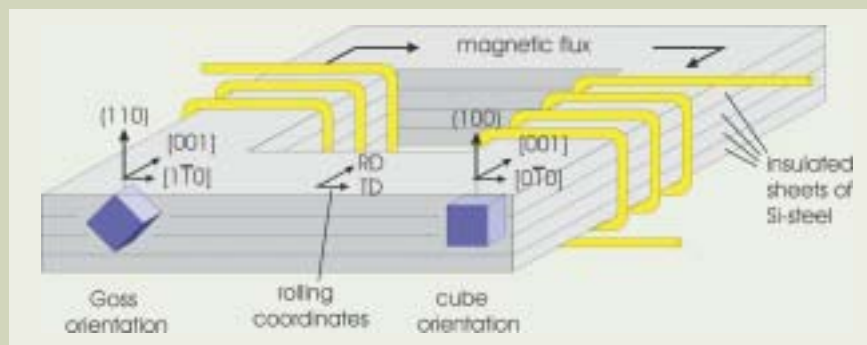

Fig. 4 Schematic drawing of the core of an electrical transformer, indicating the cube orientation {100}<001> and the Goss orientation {110}<001> as possible preferred crystal orientations. In case of the cube orientation the easiest magnetisable crystal direction, <100>, is everywhere parallel to the magnetic flux. In case of the Goss orientation only one half of the core is optimally oriented, the other one is parallel to <110>.
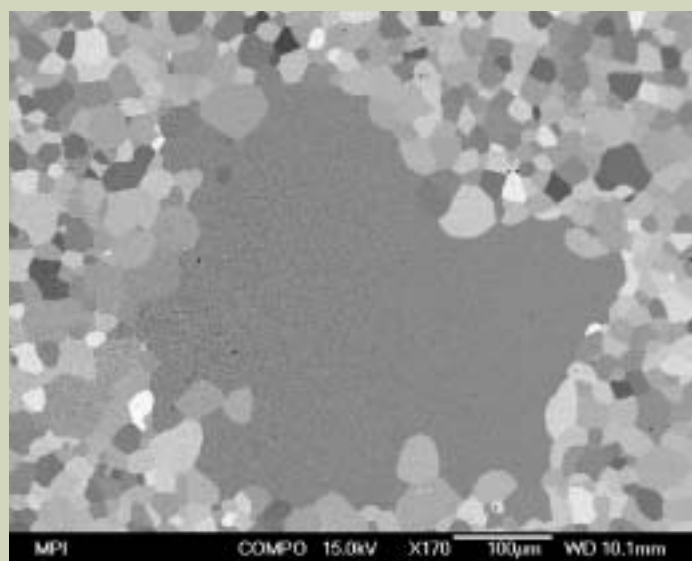

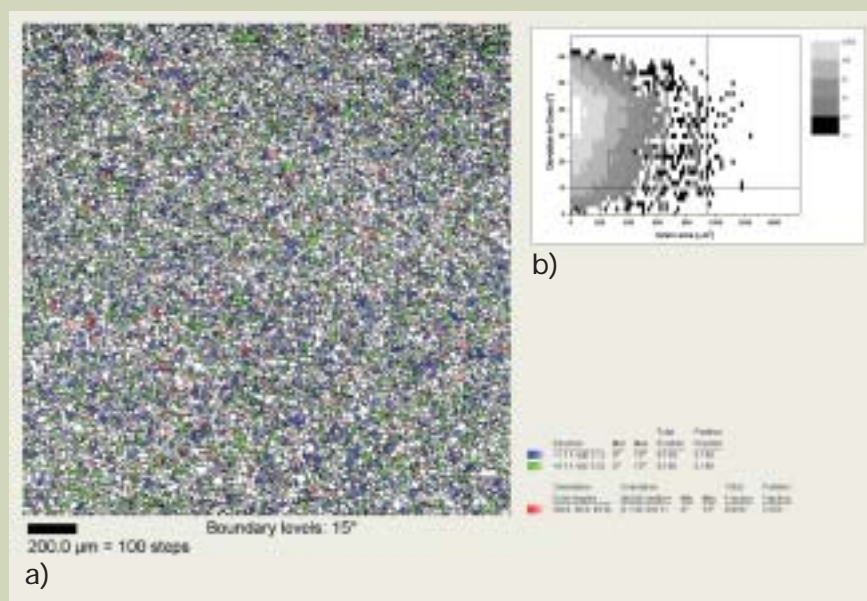Fig. 5 Channeling contrast image of a growing Goss grain in a primary recrystallised matrix.

Fig. 6 Results of ACOM on a primary recrystallised sheet of silicon steel. a) Large crystal orientation map, covering an area of approximately 2000 × 2000 μm² measured with a step size of 2 μm. About 60.000 grains are included. Blue marks γ-fibre grains (<111> ‖ ND) green marks α-fibre grains (<110> ‖ RD) and red marks Goss grains ((110)<001>). For all components a 15° spread is allowed. b) Chart representing the number of grains over their grain size and angular deviation to the Goss orientation. Horizontal and vertical lines indicate the limits for Goss grains and large grains, respectively.

cannot be quantified. Therefore, in the present case they have been carried out separately, whereby EDX spectral mapping was performed on the untilted sample. **Figure 7a** shows a backscattered electron image of the microstructure across the complete diffusion zone. Mainly atomic-number contrast reveals the position of the high-density precipitations. The ACOM map in **Fig. 7b**, in contrast, reveals the details of microstructure, including the phase and morphology of the grains. Detailed investigations [26, 27] reveal, that the whole diffusion zone is composed of 5 different layers, marked in Fig. 7b. The interface between L1$_2$ and B2 is situated in layer P1. It can be easily shown that the crystals of both phases are in Bain orientation relationship[3] with each other. From this relationship a
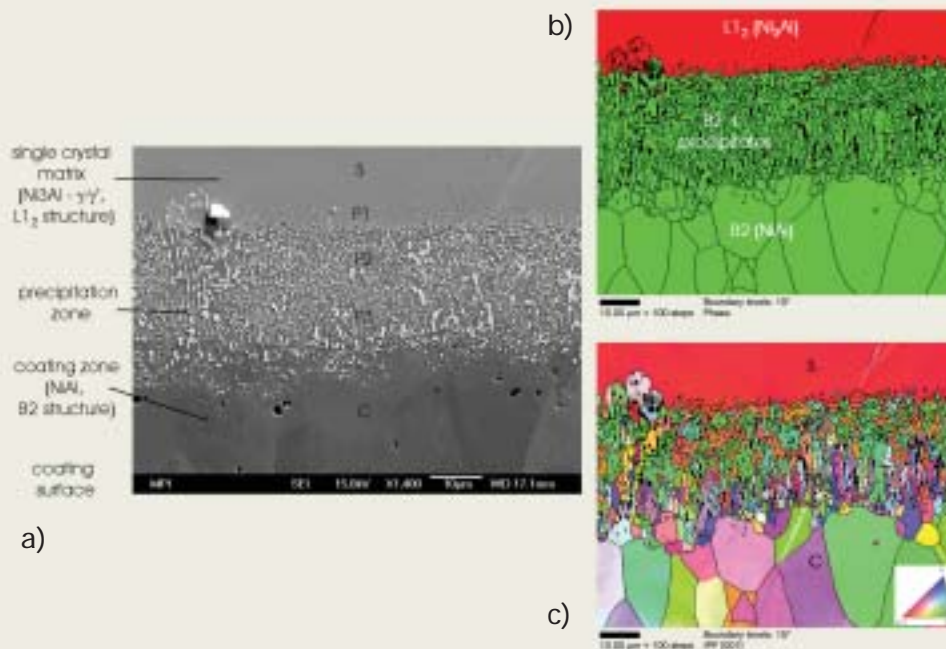

Fig. 7 Microstructure of the interface between a Ni-based superalloy single crystal (top) and an Al-rich coating formed by pack-cementation (bottom). a) BSE image showing mainly compositional contrast. The ACOM of the area marked in a) are shown in b) and c). b) is the phase distribution (showing fcc=Ni$_3$Al, bcc=NiAl,). c) is the crystal direction distribution. As reference direction serves the (001) direction of the matrix single crystal.
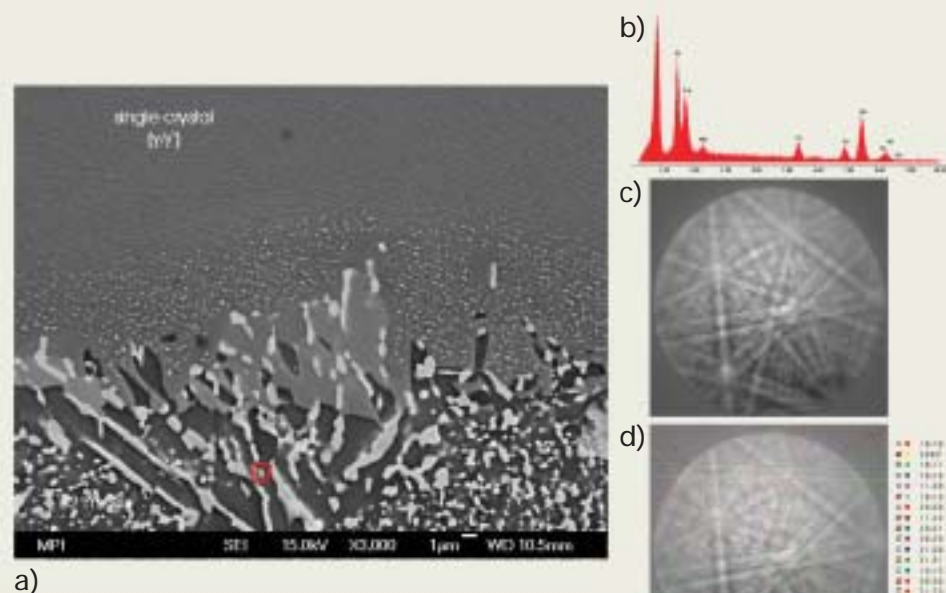

Fig. 8 Phase identification by EDX and EBSD for a precipitate in the diffusion zone of the material displayed in Fig. 7. a) BSE image of the interface. The circle marks the investigated particle. b) EDX spectrum obtained by spectral mapping. c) EBSD pattern. d) EBSD pattern overlaid with the indexing for hexagonal NiAlTa.

model for interface misfit stresses was developed, showing that mainly compression stresses arise. Layers P2 and P3 are characterized by elongated grains but different textures. Layer C finally is the actual protection layer.

The mechanical stability of the precipitation zone is strongly influenced by the strength of the precipitations. It is therefore of interest to determine their crystallographic phases. Due to the complex structure of most of these phases an automatic determination is not possible. Rather, some characteristic particles are determined manually but supported by the computer program Delphi (TSL/EDAX). First, the composition of the precipitation is determined from the quantitative EDX maps. The spectrum obtained from the marked position in **Fig. 8a** is shown in **Fig. 8b**. The spectrum reveals that the particle mainly contains Ni, Al and Ta. With this information an x-ray powder diffraction data base is searched for possible phases. A set of about 30 phases is determined. Next, the crystallographic information found in this data base is extracted and used to index an EBSD pattern obtained from the same position on the sample (**Fig. 8c**). Usually, the intensities stored for x-ray data do not fit with the electron intensities. Therefore the recognition of the correct indexing requires careful inspection of the pattern and the calculated solutions. Finally, the intensities can be adapted and the correct solution accepted. In the case presented here the hexagonal phase NiAlTa (powder diffraction file number 180045) was unequivocally determined. The fit between the calculated and measured pattern is shown in **Fig. 8d**.

Conclusions

In recent years EBSD has become an extremely powerful technique for the study of microstructure of crystalline materials. The currently optimum EBSD system consists of an SEM with a thermal field emission gun with a high and stable beam current and a flexible, highly sensitive digital CCD camera for pattern acquisition. An optimum system currently achieves spatial resolutions for crystal orientation and phase determination in the order of - depending on the material – 10 to 100 nm. The pattern acquisition and analysis rate may exceed 100 per second. Alternatively to a high acquisition rate very brilliant diffraction patterns, close to those obtained in TEM, may be obtained with few seconds of exposure time. Nevertheless, even with the highest acquisition speed the crystal orientation mapping (ACOM) technique for the measurement of orientation and phase maps stays a rather slow form of microscopy. Acquisition times up to 12 hours require a high stability of the microscope. However, the amount of quantitative data obtained by the mapping technique are unexceeded by other microscopic techniques. A couple of examples have demonstrated the possibilities: microstructures can be quantitatively characterised, for example, in terms of phase distribution, grain morphology, defect density, grain boundary character and microscopic and mesoscopic crystal orientation and misorientation distributions. Furthermore, the EBSD technique, particularly in combination with EDX, is more and more used for the crystallographic characterisation of crystals down to a size of 100 nm.

Future improvements of the technique in terms of spatial resolution, acquisition rate and pattern quality are mainly expected from optimisation of the detector system, i.e. phosphor screen and camera.

References

[1] Venables, J. A., Harland, C. J.: Electron backscattering patterns – a new technique for obtaining crystallographic information in the scanning electron microscope, *Phil. Mag*., **27**, 1193 – 1200 (1973)

[2] Dingley, D. J.: On-line determination of crystal orientation and texture determination in an SEM. Proc. Royal Microsc. Soc. **19**, 74–75 (1984)

[3] Krieger-Lassen, N. C.: Automated determination of crystal orientations from electron backscattering patterns, Ph. D. Thesis, Danmarks Tekniske Universitet, Lyngby (1994)

[4] Krieger Lassen, N. C., Juul Jensen, D., Conradsen, K.: Image processing procedures for analysis of electron diffraction patterns, *Scanning Microscopy.*, **6**, 115-121 (1992)

[5] Adams, B. L., Wright, S. I., Kunze, K.: Orientation imaging: the emergence of a new microscopy, *Metall. Trans*., **24A**, 819–831 (1993)

[6] Schwarzer, R. A.: Automated crystal lattice orientation mapping using computer controlled SEM, *Micron*., **28**, 249–265 (1997)

[7] Field, D. P.: Recent advances in the application of orientation imaging, *Ultramicroscopy, **67**, 1-9 (1997)

[8] Schwartz, A. J., Kumar, M. and Adams, B. L. (eds.): Electron Backscatter Diffraction in Material Science. Kluwer Acad./Plenum Publ., New York (2000)

[9] Humphreys, F.J.: Grain and subgrain characterisation by electron backscatter diffraction, *J. Mat. Sci.,* **36**, 3833–3854 (2001)

[10] Dingley, D. J.: Progressive steps in the development of electron backscatter diffraction and orientation imaging microscopy, *Journal of Microscopy*, **213**, 214–224 (2004)

[11] Michael, J. R., Goehner, R. P.: Crystallographic phase identification in the scanning electron microscope: backscattered electron Kikuchi patterns imaged with a CCD based detector, *MSA Bull*., **23**, 168 (1993)

[12] Small, J. A., Michael, J. R.: Phase identification of individual crystalline particles by electron backscatter diffraction, *J. Microsc.,* **201**, 59–69 (2001)

[13] Nowell, M. M., Wright,S. I.: Phase differentiation via combined EBSD and XEDS, *Journal of Microscopy*. **213**, 296-305 (2004)

[14] Wilkinson, A. J., Hirsch, P. B.: Electron Diffraction Based Techniques in Scanning Electron Microscopy of Bulk Materials, *Micron.,* **28**, 279 – 308 (1997)

[15] Thomas, I., Zaefferer, S., Friedel, F., Raabe, D.: High resolution EBSD investigation of deformed and partially recrystallised IF steel, *Adv. Eng. Mat.,* **5**, 566 – 570 (2003)

[16] Krieger-Lassen, N. C.: Automatic high-precision measurements of the location and width of Kikuchi bands in electron backscatter diffraction patterns, *Journal of Microscopy*, **190**, 375–391 (1998)

[17] Matsuo, M.: Texture control in the production of grain oriented silicon steels, *ISIJ Intern.,* **29**, 809-827 (1989)

[18] Moraviec, A.: Grain misorientations in theories of abnormal grain growth in silicon steel, *Scripta mater.,* **43**, 275–278 (2000)

[19] Homma H., Hutchinson B.: Orientation dependence of secondary recrystallisation in silicon–iron, *Acta mater.,* **51**, 3795–3805 (2003)

[20] Chen, N., Zaefferer, S., Lahn, L., Günther, K., Raabe, R.: Effects of topology on abnormal grain growth in silicon steel, *Acta mater*., **51**, 1755 – 1765 (2003)

[21] Caron, P., Khanb T.: Evolution of Ni-based superalloys for single crystal gas turbine blade applications, *Aerosp. Sci. Technol*., **3**, 513-523 (1999)

[22] Pollock, T. M., Kissinger, R. D., Bowman, R. R., Green, K. A., McLean, M., Olson M. L., Schirra, J. J., (ed.).: Superalloys 2000. TMS, Warrendale, PA (2000)

[23] Adam, P.: Fertigungsverfahren von Turboflugtriebwerken, Birkhäuser Verlag, Basel (1998)

[24] Wöllmer, S.: Untersuchungen an einer Nickelbasissuperlegierung mit niedrigem spezifischem Gewicht und an Oxidationsschutzschichten, PhD thesis, University Jena (2000)

[25] Wöllmer, S., Zaefferer, S., Göken, M., Mack, T., Glatzel, U.: Characterization of phases of aluminized nickel base superalloys, *Surface and Coating Technology,* **167**, 83 – 96 (2003)

[26] Zaefferer, S., Glatzel, U.: Orientation relationship of phases in a oxidation protection coating on a Ni-based superalloy single crystal. Proceeding of the 13th International Conference on Textures of Materials (ICOTOM 13) Seoul, Korea, editor Lee, S. 1531 – 1536 (2002)

[27] Zaefferer, S., Glatzel, U.: EBSD investigation of orientation relationships of phases in an oxidation protection coating on a Ni-based superalloy single crystal; Proceedings of Materials Week 2002, DGM e-book (2002)

Notes

1. The term "OIM" of the crystal is nowadays used as registered trade mark of TSL/EDAX.
2. These values indicate the Miller indices of the crystal plane parallel to the normal direction, ND, and the indices of the crystal direction parallel to the rolling direction, RD, of the sheet, respectively.
3. $(110)_{B2} \parallel (111)_{L12}$ and $[001]_{B2} \parallel [1\text{-}10]_{L12}$.

Growth and Encystment of the Ciliate *Tetrahymena* sp. Found in a Dead Mosquito's Larva

Tadao Takahashi[†, 1], Norikazu Miyoshi[†, 2], Takeo Suzuki[††] and Toshihiko Sunahara[†††]

†**Biological Laboratory, Faculty of Health and Social Welfare Science, Nishikyushu University**
††**Sales Division, JEOL Ltd.**
†††**Department of Microbiology, Saga Medical School**

A ciliate was found in a dead larva of the mosquito, *Aedes (stegomyia) albopictus* that was collected at a bamboo grove in the suburb of Saga City, Kyushu, in September 1999. Morphological and ecological characters of this ciliate were very similar to those of the ciliate, *Lambornella stegomyiae* belonging to the family Tetrahymenidae [4]. It was found that the ciliate grew very well in lettuce infusion including a small piece of meat.

The purpose of this work is to clarify the life history of this ciliate and its systematic relationship with the ciliates of genus *Lambornella*. As the first step of this work, we examined the morphological features in the growth and encystment of this ciliate. These experiments indicated that the present ciliate belongs to the genus *Tetraymena*. Moreover, it was also found that large numbers of cysts were formed in the stationary phase of growth. In the cyst formation, the oral apparatus broke down and absorbed to cytoplasm, and the cells transformed to round and to be covered by cyst wall, while the basal bodies of somatic cilia were retained on the cell surface. Observation of this process using a scanning electron microscope (SEM) revealed that the cilia of a given cell surface area were drawn into cytoplasm, and then such a bare cell surface was begun to be gradually covered with the cyst wall.

Introduction

In September 1999, a ciliate was found in the abdominal cavity of a dead larva of the mosquito, *Aedes (stegomyia) albopictus* collected at a bamboo grove in the suburb of Saga City, Kyushu, Japan. When the ciliate was isolated to a container with lettuce infusion containing a piece of meat, the ciliate grew very well. Now, two stokes of this ciliate are maintained in our laboratory. This ciliate is very similar to *Lambornella stegomyiae* belonging to the family Tetrahymenidae, because of the morphological and ecological features that they live in the abdominal cavity of dead mosquito's larva [4]. Culicidian mosquitoes, such as *Culex* sp. and *Aedes* sp., are known as a vector of dengue fever and other virus type fevers in South Africa and South Eastern Asia [1, 3, 13, 18]. It has been reported that the ciliate *L. stegomyiae* attacked the living larva of such mosquitoes, invaded hosts' abdominal cavities, multiplied, and then finally killed the hosts [1, 3, 5, 6, 8, 9, 13, 14, 15]. Although the present ciliate lived in the abdominal cavity of a dead mosquito's larva, our preliminary experiments showed that they did not attack the living mosquito's larva nor invade their abdominal cavities. However, it was verified that if a dead larva of mosquito was given to this ciliate, the ciliate would invade into mosquito's abdominal cavity and would proliferate there (Sunahara, unpublished data). It, therefore, would be interesting to clarify the life history of this ciliate and the systematic relationship between this species and the ciliates of genus *Lambornella*. As the first step of the investigation, we examined characters of growth and morphological features during cyst formation in this ciliate.

Materials and Methods

Cells

Stock A5, which was established in our laboratory, was mainly used in this work. Stock cultures of A5 were maintained at 23 ± 1°C in lettuce infusion (0.5 g dried lettuce powder/1000 mL DW, boiled for 5 minutes) including a piece of raw beef or chicken meat (1.2 g/1000 mL). Two days before the beginning of an experiment, cells of the stock culture were transferred to a newly prepared culture medium and were maintained at 23 ± 1°C.

Growth

To examine the growth of the ciliate, the exponentially growing cells (10 cells/mL as initial cell density) were transferred to a 200 mL Erlenmeyer flask with 50 mL culture medium, and then they were maintained at 23±1°C. For estimation of cell densities in the culture, known volume of aliquots of cell suspension were put on a cell counting plate after enough agitation of the culture for obtaining even distribution of cells. Subsequently, they were fixed with a few drops of Bouin's fluid (saturated piclic acid : formalin : acetic acid = 15:5:1 mixture), and then they were counted by using a counter under the dissecting microscope.

Deciliation

Deciliation of cells was performed following Ogura's ethanol method [10]. The cells were transferred to a test tube containing Ogura's adapting solution (1 mM $CaCl_2$, 0.5 mM KCl, 0.5 mM KOH, 1 mM HEPES, pH 7.4 with HCl) for 15 to 30 minutes. Subsequently, these cells were transferred to another test tube containing Ogura's adapting solution with 5% of ethanol, and then the test tube was given strong shakes for one to two minutes to remove the cilia. These deciliated cells were resuspended in distilled water.

Induction of encystment

The stationary phase of culture was filtrated with Kimwipe to remove large debris in the culture, and then the cells were collected by centrifugation (1200 rpm, 5 minutes). Such concentrated cell suspension was diluted 10 to 20 times with culture medium or CFF (cell-free fluid). These cell suspensions were transferred to depression slides with 100 μL each, and

†, 1 Corresponding author. 4490-9 Kanzaki, Kanzaki, Saga 842-8585, Japan
E-mail: ttadao@nisikyu-u.ac.jp

†, 2 Present address. Department of Upland Farming National Agricultural Research Center for Tohoku Region.
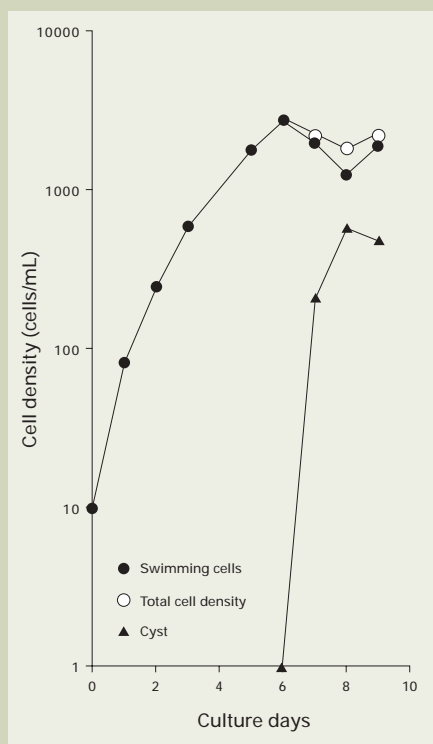
Fig. 1 Growth curve of the ciliate *Tetrahymena* sp. cultured at 23°C in a lettuce infusion containing a piece of raw beef.
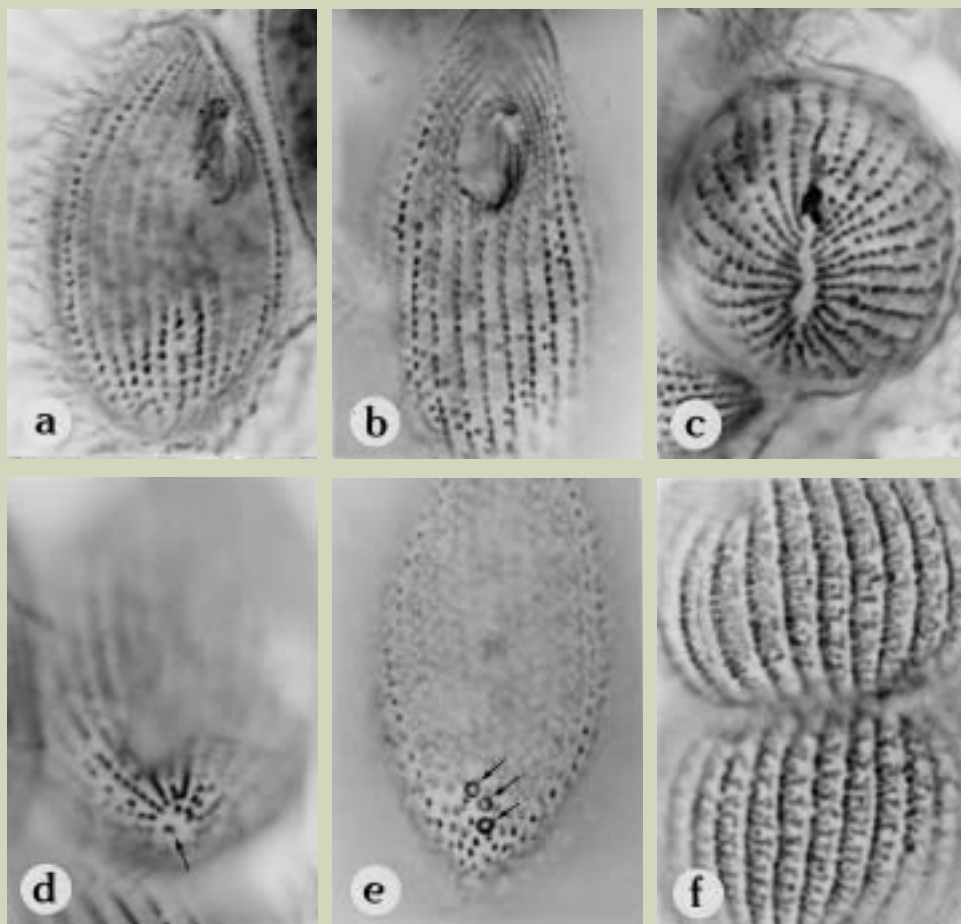

Fig. 2 Cortical structures of vegetative (a to f) and encystment cells (g to i). Bar = 10 μm. All micrographs are the same magnification.
a and **b:** Non-dividing cell.
c: Anterior pole region of a non-dividing cell.
d: Posterior pole region of a non-dividing cell. Allow indicates a basal body of the caudal cilium.
e: Posterior region of a non-dividing cell. Allows indicate contractile vacuole pores.
f: Dividing cell.
g: Breaking down of the oral apparatus at early stage of encystment.
h and **i:** Spherical encysting cell. The oral apparatus is already disappeared, while basal bodies of somatic cilia are retained.

maintained at 23 ± 1°C. Thereafter, the rate of cyst formation was examined at regular intervals.

Preparation of CFF

CFF (cell-free fluid) was prepared by following procedure. The stationary phase of culture was filtrated with No. 2 filter paper (Advantec) to remove large debris in the culture. Then, the filtrated cell suspension was centrifuged for removing the most of cells (1500 rpm, 10 minutes). This rough cell-free fluid was transferred to an aspiratory filtration equipment (Nalgen, 500 mL) with DP70 filter paper (Advantec, 45 mm in diameter) and was filtered by an aspirator (WP-15, Yamato). The filtered fluid was filtered again using the same equipment with CMF filter paper (Advantec, pore size 10 μm, 45 mm in diameter), and then the filtrated fluid was finally filtered using a millipore filter (Advantec, pore size 0.45 μm, 45 mm in diameter).

Silver impregnation

To know the morphological features of the ciliate, the cells were impregnated by the Chatton-Lwoff wet silver nitrate method after the modification of Gillies and Hanson [7].

Specimen preparation for SEM

The cell suspension was filtrated with Kimwipe to remove large debris in the culture, and then the cells were collected by centrifugation (1200 rpm, 5 minutes). These cells were washed twice with distilled water. These cells were fixed with Párducz's fixative (2% OsO_4 : saturated $HgCl_2$ =6:1 mixture) for about one minutes at room temperature, and washed twice with double de-ionized water (DDW). Then SEMpore (made by JEOL), equipped with silicone ring on the holder, was installed on a SEMpore holder (made by JEOL) joining a 50mL disposable syringe, and after its surface was washed with DDW it was coated with 0.1% poly-lysine hydrobromide solution (MW 70000 - 150000, Sigma). Then fixed and washed ciliates were transferred gently to a drop of DDW (approx. 20 μL) on the SEMpore. After waiting for one to two minutes, several drops of t-butanol were dripped on the specimen, and DDW of the specimen was completely replaced with t-butanol after treating for

about 30 minutes. The t-butanol on this SEM-pore was completely frozen using liquid nitrogen. The frozen specimen was set in the specimen chamber of a SEM (JEOL JSM-5500LV) as it was. Then, it was allowed to dry up by waiting for about two hours in the low vacuum mode (LV mode, pressure in the specimen chamber 30 Pa, accelerating voltage 15 kV, spot size 40 to 50). The dried specimen was coated with platinum to a thickness of about 25 nm using an ion sputtering system (JEOL JFC-1600). The specimen was observed in the high vacuum mode (HV mode, accelerating voltage 5 kV, spot size 15 to 20) using a SEM (JEOL JSM-5500LV) at Nishikyushu University.

Results and Discussion
Growth curve

When the cells were kept at 23 ± 1°C in lettuce infusion including a piece of meat, they grew logarithmically until day 2 of the culture, and then continued to proliferate until day 6, followed by the stationary phase of growth (**Fig. 1**, ○). The maximum cell density reached up to 2217 cells/mL at day 6 of the culture, while the encysting cells appeared in the culture after day 7 (**Fig. 1**, ▲). In this process, it had not been known whether the ciliates directly engulfed the pieces of meat. They, however, proliferated around the piece of meat. Furthermore, naturally contaminated bacteria also proliferated around the piece of meat. Our preliminary experiments have indicated that the ciliate does not grow in a lettuce infusion including bacteria *Enterobacter aerogenes* as food organisms without a piece of meat. Therefore, it is difficult to consider that this ciliate grows by ingesting the bacteria around the meat. Since it is well known that the ciliates belonging to the genus *Tetrahymena* release some kinds of digestive enzyme into the culture medium, it is highly possible that this ciliate also release some sort of digestive enzyme [2, 11, 12]. This problem remains to be analyzed in the future.

Morphology of swimming cells

The swimming cell is a long ellipsoid. Mean cell length and width was 57.0 ± 12.2 μm (± SD) and 29.3 ± 14.0 μm (±SD) (n=500), respectively. The oral apparatus was located in the anterior 1/4 to 1/5 ventral region of the cell and was constructed by three membranelles and one paroral membrane. The most left membranelles, which is called the first membranelle, is the largest, while the most right one, which is called the third one, is the most small of them. In the first and second membranelles their anterior potions slightly bend to the right side, that is, to inner side of the oral apparatus (**Fig. 2a**)*. The number of post oral kineties (POM's) is typically two (Fig. 2a, **Fig. 3c**). Furthermore, in the apical region of this ciliate there is a dorsoventrally oriented and non-ciliated strip of area (**Fig. 2c, 2i**). On the contrary, in the ciliate of the genus *Lambornella*, the second membranelle is the largest among three membranelles, and curves inverted S-shape. Furthermore, the number of POM's is three or more. From these morphological characters, the present species might belong to the genus *Tetrahymena*, not to the genus *Lambornella*.

It was also found by observation of the silver impregnated specimen that the posterior end of the cell was a non-ciliated, small circular bare area. In the center of this area, only one basal body was observed (**Fig. 2d**). It could not be confirmed by observation of living ciliates whether the ciliate has a caudal cilium in the posterior end of the cell. However, it could be confirmed using a SEM that the ciliate has a caudal cilium of which length is the approximately same as that of somatic cilia (**Fig. 3e, Fig. 4b**). One to four contractile vacuole pores located at 1/4 to 1/5 posterior right region of the cell (**Fig. 2e, Fig. 3f**). By using a SEM, it could be observed very curious character that many cilia of the anterior ventral region were oriented toward the one side like brush (**Fig. 3b**). The metachronal beating of the cilia also could be observed using a SEM (**Fig. 3a**).

Encystment

This ciliate often formed cysts during culture. Many cells began to encyst in the early stationary phase, and almost all cells finally encysted in the late stationary phase. These cysts were easily excysted when they were transferred to a newly prepared culture medium containing a piece of meat. From these facts, it was suggested that this ciliate proliferated by cell divisions under the good conditions for the growth, while they might undergo encystment under certain environmental conditions, such as drying, deficient of food, and others. From the observation of living encysting cells it was revealed that the cells tended to gather on the bottom of container and to rotate there prior to cyst formation. Cells of these stages were collected and stained by Chatton-Lwoff silver impregnation method. From the observation of these impregnated cells, it was found that the cells gradually shortened along the longitudinal axis, and then their oral membranelles gradually broke down and degraded (**Fig. 2g**). Then the cell became a round cyst. In these processes, the number of membranellar basal bodies gradually decreased, and they finally disappeared (**Fig. 2h,** 2i). On the contrary, the basal bodies of the somatic ciliary rows were not extinct even at the final stage of encystment (Fig. 2h, 2i). Since this staining method did not reveal whether each of these basal bodies bore
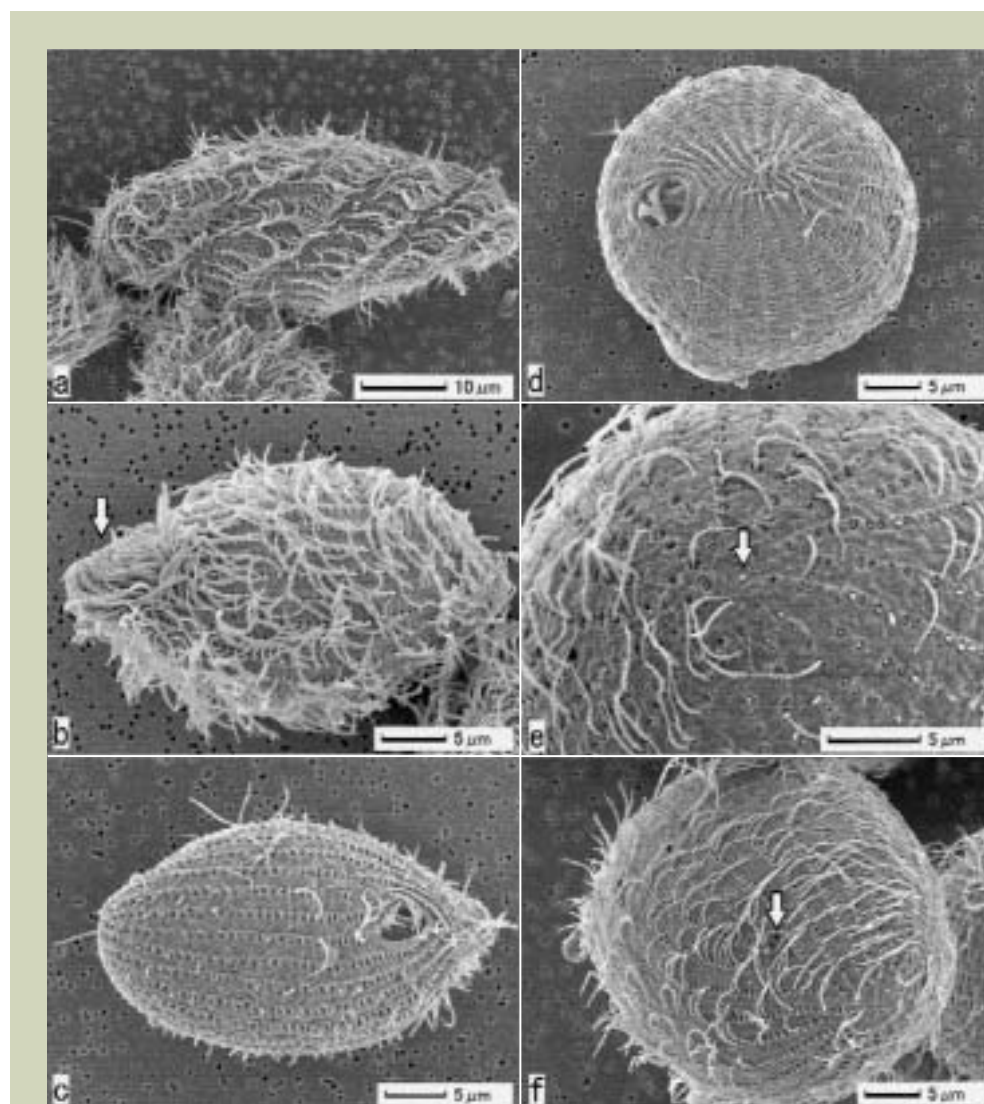

Fig. 3 The vegetative cell was visualized by scanning electron microscopy.
a: A swimming cell. The cilia show metachronal beating. **b:** At the anterior ventral region (arrow), the cilia tend to be often oriented in the same direction like brush. **c:** A deciliated swimming cell. It can be seen clearly that the cell has two rows of POM's. **d:** Anterior pole region of a deciliated non-dividing cell. **e:** Posterior pole region of a deciliated non-dividing cell. Allow indicates a caudal cilium. **f:** Posterior region of a deciliated non-dividing cell. Allow indicates a contractile vacuole pore.

cilium, the morphogenetic events of encystment were examined by scanning electron microscopy. The observations revealed that in the rounded cells gathering on the bottom of container their cilia beat nearly perpendicularly right-ward against the longitudinal axis of the cell (**Fig. 4a, 4b**). This suggested that the cells were rotating clockwise on the bottom of container. In a given area of the rounding cell, several cilia were gradually drawn into the cell (**Fig. 4c, 4d**). Subsequently, this non-ciliated bare area began to covered with cyst wall, although the remainder cortical area was covered with many cilia, yet (**Fig. 4e**). Finally, the cell became completely spherical cyst of which surface was entirely covered with cyst wall. Furthermore, it was found that there were many ridge-like furrows on the cyst wall, which might be consistent with ciliary rows.

It is important to establish the inducing method of the cyst formation to analyze the encystment inducing factors and to observe the more detail morphogenetic events. As preliminary experiments, we tried to induce the cyst formation by the newly prepared culture medium containing bacteria and CFF (cell-free fluid) obtained from stationary phase of culture. Our preliminary experiments revealed that the cells tend to easily transform the cysts, when the cells were transferred to encystment inducing medium with large surface-volume ratio (the wide surface area and shallow in depth). We, thus, tried to induce the cyst formation by the following procedures. 100 μL of cell suspension was transferred to a well (22 mm in diameter, 8 mm in depth) of the depression slide and was maintained at 23 ± 1°C. When the encystment was induced by culture medium containing bacteria, the mean cyst formation rate was 3.8 ± 0.8% (± SD) at 21 hour, 3.3 ± 2.7% at 27 hour and 20.1 ± 10.6% at 45 hour after the onset of induction, respectively. On the contrary, when the encystment was induced by CFF, the mean cyst formation rate was 18.1 ± 8.8% at 21 hour, 18.2 ± 8.9% at 27 hour and 43.1 ± 16.4% at 45 hour after the onset of induction, respectively. It was suggested that the present ciliate did not grow in the bacterized lettuce infusion, but the cyst formation occurred slowly under the condition of the presence of bacteria in the culture medium. On the other hand, when the encystment was induced with CFF, which was removed *Tetrahymena* cells and bacteria, the cyst formation occurred at higher rate than using culture medium with bacteria. These results suggested that starvation, that is no food supply, or some substance(s) contained in CFF might be important for inducing cyst formation in this ciliate. It has been reported that in the ciliate *Euplotes* a kind of low molecular weight protein released from the cell might play an important role in the encystment [16, 17]. However, in the present species, it may be important for encystment that the amount of cell suspension is small with large surface-volume ratio, no food supply, and no existence of bacteria. Therefore, it could not exclude the possibility that in this ciliate the mechanisms of cyst formation differ from those of *Euplotes*. Thus, it should be urgently established the encystment inducing method, which may be required high rate and rapid encystment.

References

[1] Arshad, H. H. and Sulaiman, I.: *J. Invertebr. Pathol.,* **66**, 303-306 (1995)
[2] Banno, Y, Yano, K. and Nozawa, Y.: *J. Protozool.,* **29**, 91-98 (1982)
[3] Broberg, L. E. and Bradshaw, W. E.: *J. Med. Entomol.,* **34**, 38-45 (1997)
[4] Corliss, J. O.: In Biology of *Tetrahymena*. Elliott, A. M. (Ed.), Dowden Hutchinson & Ross, Inc., Pennsylvania. Chapt. 1, pp. 1-55 (1973)
[5] Corliss, J. O. and Coasts, D. W.: *Trans. Amer. Micros. Soc.,* **95**, 725-739 (1976)
[6] Egerter, D. E., Anderson, J. R. and Washburn, J. O.: *Proc. Natl. Acad. Sci. USA,* **83**, 7335-7339 (1986)
[7] Gillies, C. G. and Hanson, E. D.: *Acta Protozool.,* **6**, 13-31 (1968)
[8] Keilin, D.: *Parasitology,* **13**, 216-224 (1921)
[9] Mahadevan, V. S., Ong, K. K., Ghani, A. and Ong, Y. F.: *J. Vect. Ecol.,* **21**, 89-93 (1996)
[10] Ogura, A.: *Cell Stract. Funct.,* **6**, 43-50 (1981)
[11] Suzuki, K.-M., Hosoya, N., Takahashi, T., Kosaka, T. and Hosoya, H.: *J. Biochem.,* **121**, 642-647 (1997)
[12] Tiedke, A. and Rasumussen, L.: *J. Cell. Physiol.,* **136**, 554-556 (1998)
[13] Washburn, J. O., and Anderson, J. R.: *J. Invertebr. Pathol.,* **48**, 296-309 (1986)
[14] Washburn, J. O., Gross, M. E., Mercer, D. R. and Anderson, J. R.: *Science,* **240**, 1193-1195 (1988)
[15] Washburn, J. O., Mercer, D. R. and Anderson, J. R.: *Science,* **253**, 185-188 (1991)
[16] Yonezawa, F.: *J. Sci. Hiroshima Univ., Ser. B, Div. 1,* **32**, 73-82 (1985)
[17] Yonezawa, F.: *J. Sci. Hiroshima Univ., Ser. B, Div. 1,* **32**, 245-254 (1986)
[18] Yoshida, Y. Illustrated Human Parasitology 5th ed., Nanzando Co. Ltd., Tokyo (1997)

* The directions right and left of the ciliate are defined as follows: right and left of the ciliate refer to observer's right and left, assuming that he stands inside the ciliate so that his anterior-posterior axis coincides with that of the ciliate.
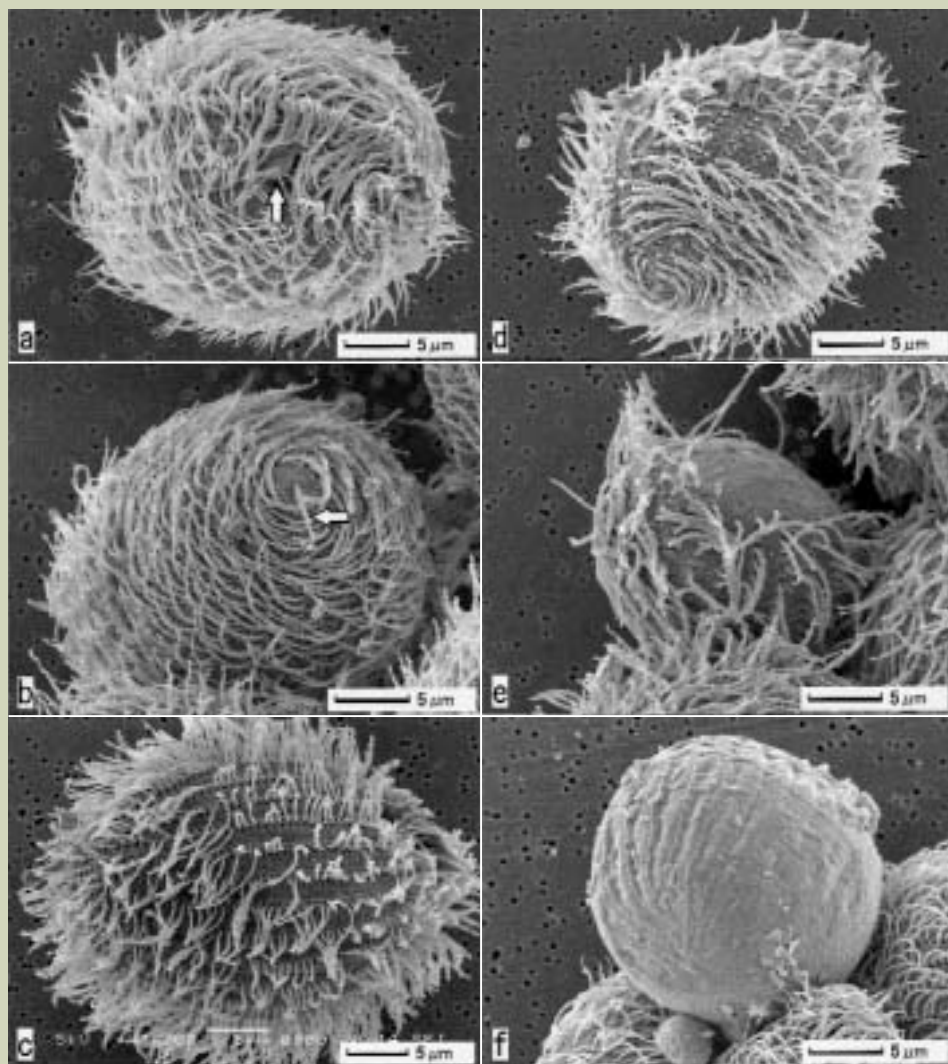

Fig. 4 The encysting cell was visualized by scanning electron microscopy.
a: A cell begins to be shortened along the longitudinal axis. Allow indicates an oral apparatus.
b: Posterior pole region of an early encysting cell which undergoes rotating movement on the bottom of a container. Allow indicates a caudal cilium. **c:** Beginning the absorption of cilia.
d: The cilia are gradually drawn into cytoplasm. **e:** The bare cell surface is begun to be gradually covered with the cyst wall. **f:** A mature cyst. There are many ridge-like furrows on the cyst wall.

ALCHEMI Studies on Quasicrystals

Koh Saitoh[†]**, Michiyoshi Tanaka**[††]**, An Pang Tsai**[††] **and Chris J. Rossouw**[†††]

[†]**National Institute for Advanced Industrial Science and Technology**
[††]**Institute of Multidisciplinary Research for Advanced Materials, Tohoku University**
[†††]**Commonwealth Scientific & Industrial Research Organisation**

Introduction

Many microscopists using a transmission electron microscope (TEM) might have experienced that the energy dispersive X-ray (EDX) spectrum, which is obtained from the same crystalline thin film, varies depending on the crystallographic orientations. This is due to the channeling effect of incident electrons. That is, incident electrons, which excite atoms in a crystal, may channel preferentially on a specific site in a unit cell due to strong dynamical diffraction. The channeled site varies with the crystallographic orientation, and thus, X-ray emission rates vary as the channeled site varies. An important point is that the orientational dependences of the intensities of X-rays emitted from the excited atoms are the same if the crystallographic sites of these atoms are equivalent. In 1982, Taftφ and Spence developed a technique to determine crystallographic sites by investigating the orientational dependences of the X-ray emission counts. They called this technique atom location by channeling-enhanced microanalysis (ALCHEMI) [1]. For instance, the crystallographic site of a substitutional impurity atom can be determined by comparing the characteristic X-ray intensity of the impurity atom with that of each host atom.

The original ALCHEMI required measurement of intensities of EDX spectra obtained under different diffraction (or channeling) conditions. The number of spectra needed for this measurement depends on the number of different sublattice sites over which a dopant atom is distributed. The angular-scanning technique of the incident electron beam was first introduced to the ALCHEMI method by Bielicki [2]. This technique displays two-dimensional channeling patterns obtained by a systematic angular scan of the electron beam, and it is shown that the contrast in the obtained patterns varies between different sublattice sites. Rossouw *et al.* [3] described that the angular-scanning ALCHEMI patterns around low-index zone axes provide more reliable and accurate results about the site occupation than the conventional ALCHEMI patterns, because

[†]Tsukuba Central-5 Higashi 1-1-1, Tsukuba Ibaragi, 305-8565, Japan
  E-mail : saitoh.koh@aist.go.jp

a number of intensity data (~ 5000 data) are used. Rossouw *et al.* [4] showed that visual inspection of the channeling pattern may be sufficient to reveal the sublattice site distribution of 1 atomic percent impurity atoms.

Here, we show an experimental example obtained from GaAs, which has the zinc-blend type structure. Ga atoms and As atoms are projected onto different positions in the [110] projection but onto an equivalent position in the [111] projection. Thus, it can be expected that the orientational dependences of the characteristic X-ray emission rates (channeling patterns) of Ga and As are different in the [110] projection but the same in the [111] projection. **Figures 1 (a)** and **1 (b)** show the channeling patterns of Ga and As taken around the [110] incidence using Ga-K and As-K emissions. The angular ranges in the horizontal and vertical directions are approximately 100 mrad and 70 mrad, respectively. **Figure 1 (c)** shows the ratio pattern of Ga/As, which enhances the difference in contrast between the Ga and As patterns. A specific contrast seen in the ratio pattern clearly shows that the channeling patterns produced by Ga-K and As-K are different, confirming that Ga and As are projected onto different positions in this projection. **Figures 2 (a)** and **2 (b)** show the channeling patterns taken around the [111] incidence using the same X-ray emissions as Figs. 1 (a) and 1 (b). **Figure 2 (c)** shows the ratio pattern of Ga/As. The ratio pattern is dominated by the noise signal, showing no specific contrast. This pattern confirms that Ga and As are projected onto an equivalent position in this projection.

Quasicrystals are new types of solids, which are neither ordinary crystals due to their non-crystallographic rotational symmetry such as 5-fold rotation symmetry, nor amorphous solids by their long range order. **Figure 3** shows an electron diffraction pattern of a decagonal quasicrystal of $Al_{72}Ni_{20}Co_8$. It can be seen that the pattern shows sharp reflection spots and has tenfold rotation symmetry. Quasicrystals have been discovered in various intermetalic compounds so far. Most quasicrystals are ternary alloys composed of Al and two kinds of transition metals (TMs), whereas their crystalline approximants are often binary alloys of Al and a TM. It is considered that the second TM element in qua-

sicrystals plays an important role in stabilizing the quasicrystalline structure. Thus, it is worth investigating the location of the second TM atoms, that is, whether the first and second TM atoms are located at the same or different kind of sites.

Using high-angle annular dark-field scanning transmission electron microscopy (HAADF-STEM), the arrangements of the TM atoms have been shown for various decagonal quasicrystals [5-12]. However, the TM atoms were not clearly distinguished in the HAADF-STEM images, because their atomic numbers are too close. The original ALCHEMI method had been applied to an icosahedral quasicrystal of Al-Cu-Fe by Shindo *et al* [13]. They found that Al occupies a set of sublattice sites different from that of TMs. However, they could not distinguish whether Cu and Fe are mutually ordered or disordered.

In the present paper, the 2D angular-scanning ALCHEMI method was applied to decagonal quasicrystals to reveal the chemical order between transition metal atoms. A simulation study using structural models with and without chemical order was also made to confirm the present results.

Experimental

An alloy with a nominal composition of $Al_{72}Ni_{20}Co_8$, $Al_{70}Ni_{18}Co_{12}$, $Al_{70}Ni_{15}Fe_{15}$ and $Al_{66}Cu_{17}Co_{17}$ were investigated in the present study. A fundamental lattice phase of $Al_{72}Ni_{20}Co_8$ and a superlattice phase of $Al_{70}Ni_{18}Co_{12}$ were prepared by annealing the ingots with the same nominal compositions at 900°C for 47 h, followed by quenching in cold water [14-16]. Decagonal $Al_{70}Ni_{15}Fe_{15}$ was prepared by the melt-quenching technique using a single roller melt spin apparatus rotating at 3000 rpm[17]. Decagonal $Al_{66}Cu_{17}Co_{17}$ was prepared by the Bridgeman method from an ingot with a nominal composition of $Al_{65}Cu_{7.5}Co_{27.5}$ [18]. The specimens were crushed and glued on Cu or Mo grids for electron microscopy. The present ALCHEMI study was carried out using a JEM-2010FEF electron microscope operated at an accelerating voltage of 100 kV. The microscope is fitted with an Oxford LINK ultra thin window EDX detector for measuring characteristic X-

ray emissions. Al and TM count windows were set on each K-edge peak. 64×54 EDX spectra were measured at an angular scan range of about 100 mrad along the x-axis and about 70 mrad along the y-axis, and displayed as two dimensional patterns for each element. The electron probe size on the specimen was 200 - 400 nm in diameter. The angular convergence of the electron beam was 1.8 mrad. During the experiment, no damages of the specimens due to electron beam illumination were observed.

Results and Discussion

$Al_{72}Ni_{20}Co_8$

Figures **4 (a)**, **4 (b)** and **4 (c)** show channeling patterns of $Al_{72}Ni_{20}Co_8$ using characteristic K X-rays of Al, Ni and Co, respectively, where the electron beam was scanned around the decagonal zone axis. Figure 4 (a) shows a bright spot at the zone-axis incidence indicated by the arrow and weak bright bands, each of which is sandwiched by two dark lines and runs through the zone-axis position. The bands are rotated by 36 degrees to each other, forming tenfold rotation symmetry about the zone-axis position. Figure 4 (b) shows slightly bright lines radiating from the zone-axis center and a bright spot at the center. Figure 4 (c) also exhibits a pattern similar to Fig. 4 (b). The difference between Fig. 4 (a) and Figs. 4 (b) and 4 (c) indicates that each Al atom occupies a site different from that of Ni and Co. Figures **4 (d)**, **4 (e)** and **4 (f)** show the intensity ratio patterns of Ni/Al, Co/Al and Co/Ni, respectively. The ratio patterns of Ni/Al and Co/Al show similar specific radial lines, indicating more clearly that the Al site is different from the Ni and Co sites. On the other hand, the ratio pattern of Co/Ni shows extremely weak contrast on the noise background. This implies that, to a good approximation, Co and Ni occupy the same sites, or that Co and Ni are chemically disordered.

Other channeling patterns taken in different crystallographic orientations show the same feature as mentioned above, that is, TM/Al patterns show certain contrast and Co/Ni patterns show almost no contrast. Therefore, we conclude that, to a good approximation, Al
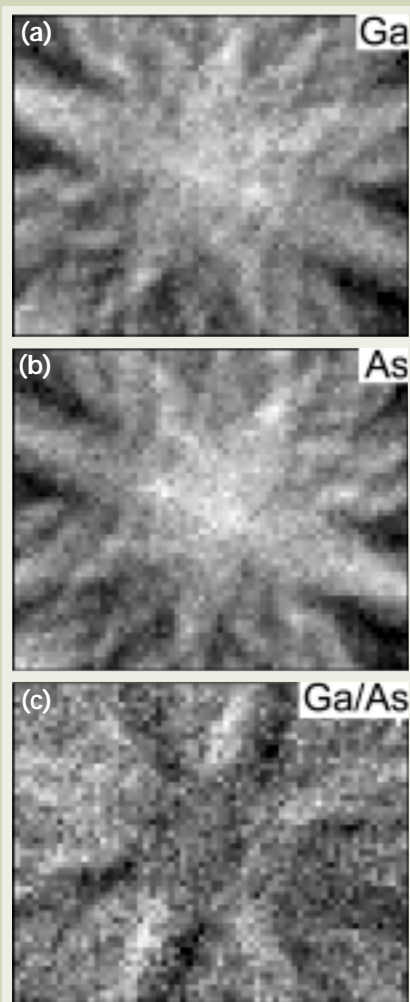

Fig. 1 Channeling patterns of GaAs taken around the [110] zone-axis incidence using X-ray emissions of (a) Ga-K and (b) As-K. The ratio pattern of Ga/As is shown in (c), which clearly shows the difference between the Ga and As patterns, indicating that Ga and As atoms are projected onto different positions in this projection.
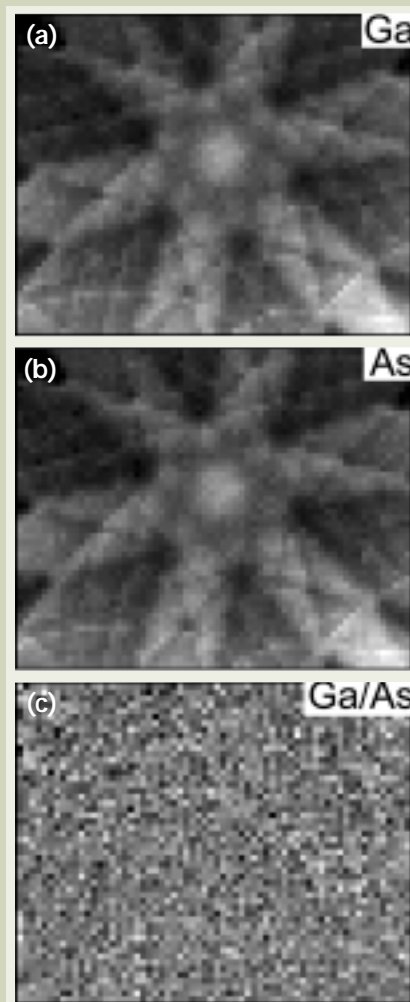

Fig. 2 Channeling patterns of GaAs taken around the [111] zone-axis incidence using X-ray emissions of (a) Ga-K and (b) As-K. The ratio pattern of Ga/As is shown in (c), which is dominated by noise, indicating that Ga and As atoms are projected onto the same position in this projection.
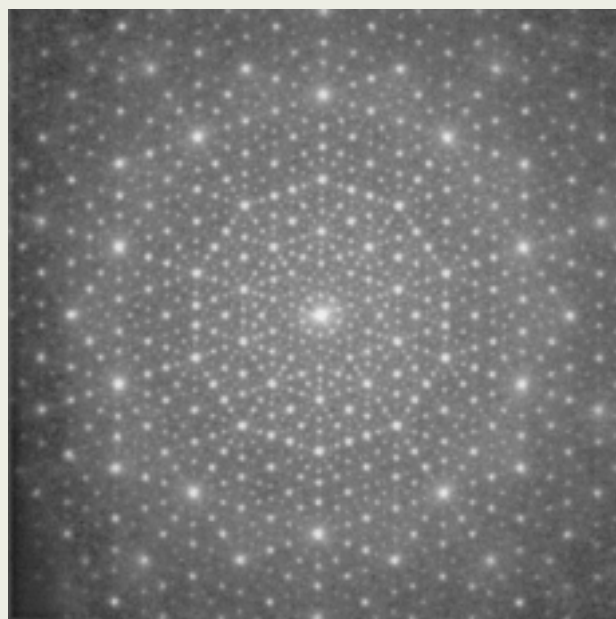

Fig. 3 A selected-area electron diffraction pattern of a decagonal quasicrystal of $Al_{72}Ni_{20}Co_8$ taken at an incidence along the decagonal axis. The pattern shows sharp reflection spots and has tenfold rotation symmetry.

atoms occupy a set of specific sites different from TMs, and that Co and Ni atoms occupy the same site in disorder [19, 20].

In order to confirm the chemical disorder between Ni and Co, we simulated the channeling patterns of $Al_{72}Ni_{20}Co_8$ by using the two structural models with and without chemical disorder. **Figures 5 (a)** and **5 (b)** show the atom clusters of the two structural models with and without chemical disorder, respectively [21, 22]. The simulations were made for hypothetical crystalline structures with periodic arrangements of the clusters, which approximate a real quasicrystalline structure. Channeling states formed by the incident electron beam with different orientations were calculated on the basis of the multislice algorithm. X-ray emission rates were calculated by integrating the product of the inelastic scattering cross section of the excited atom and the amplitude of the channeling state over the unit cell and over the specimen thickness. Channeling patterns were calculated at an accelerating voltage of 200 kV with the specimen thickness of 100 nm. **Figures 6 (a), 6 (b)** and **6 (c)** show simulated channeling patterns of Al-K, Ni-K and Co-K emissions respectively, by using the chemical disorder model at incidences around the decagonal zone-axis. **Figures 6 (d), 6 (e)** and **6 (f)** show the ratio patterns of Al/Ni, Al/Co and Ni/Co, respectively. It can be seen that the ratio patterns of Al/TMs clearly show a specific contrast, but that of Ni/Co does not show any contrast. This feature is consistent with the experimental result as mentioned above. **Figures 7 (a)** to **7 (f)** show simulated channeling patterns of Al-K, Ni-K and Co-K emissions by using the chemical disorder model and their ratio patterns of Ni/Al, Co/Al and Co/Ni. It can be seen that the ratio pattern of Ni/Co clearly show a specific contrast, even for an 8 atomic percent of the Co content. This simulation analysis strongly supports that Ni and Co occupy the same site. It should be pointed out that the present result is consistent with the fact that $Al_{72}Ni_{20}Co_8$ is a Hume-Rothery electron compound, in which the composition of Ni and Co atoms adjusts the electron atom ratio (*e/a*) of the alloy [23, 24].

$Al_{70}Ni_{18}Co_{12}$ and other quasicrystals

We applied the ALCHEMI technique also to other decagonal quasicrystals to reveal their chemical order. A superlattice-ordered decagonal quasicrystal of $Al_{70}Ni_{18}Co_{12}$ had been believed to have an atomic chain of an alternative sequence of Ni and Co along the decagonal axis, and thus, have a chemical order between Ni and Co. **Figures 8 (a), 8 (b)** and **8 (c)** show channeling patterns of $Al_{70}Ni_{18}Co_{12}$ using characteristic K X-rays of Al, Ni and Co, respectively, where the electron beam was scanned around the decagonal zone axis. The Al pattern shows a bright spot at the zone-axis incidence position and slightly bright bands radiating from the zone-axis position. The Ni pattern shows a dark spot at the zone-axis position and pairs of slightly bright lines radiating from the zone-axis position. The Co pattern shows a feature similar to that of the Ni pattern. The difference between the Al pattern and the TM patterns indicates that

the Al site is different from the Ni and Co sites, similar to the case of $Al_{72}Ni_{20}Co_8$. The ratio patterns of Ni/Al (**Fig. 8 (d)**) and Co/Al (**Fig. 8 (e)**) clearly show the difference between the Al and TM patterns. The ratio pattern of Co/Ni (**Fig. 8 (f)**) is dominated by noise, showing no specific contrast. This indicates that Ni and Co atoms randomly occupy the same site. Channeling patterns taken at different crystallographic orientations show the same feature as mentioned above, that is, TM/Al patterns show certain contrast and Co/Ni patterns show almost no contrast. Therefore, for $Al_{70}Ni_{18}Co_{12}$, we conclude that Al atoms occupy a set of specific sites different from TMs, and that Co and Ni atoms occupy the same site in disorder [25].

We also found that an $Al_{70}Ni_{15}Fe_{15}$ decagonal quasicrystal has the same feature of chemical order as that of Al-Ni-Co. An Al-Cu-Co decagonal quasicrystal, however, was found to have a chemical order between Cu and Co as well as that between Al and TMs [26]. This might be due to a unique character of the electronic structure of Cu. That is, the electronic

structure of Cu has an intermediate character between the electronic structures of Al and Co, and thus Cu may be able to substitute for both Al and Co, whereas the electronic structure of Co is rather different from that of Al, and thus Co may not be able to substitute for Al. In fact, a Monte Carlo simulation study using pair potentials showed that a stable structure possesses a strong chemical order between Cu and Co [27]. This fact is consistent with our ALCHEMI results.

Conclusion

The 2D angular-scanning ALCHEMI technique was applied to quasicrystals. It was shown that the quasicrystals show characteristic channeling patterns at incidences of particular zone axes as ordinary crystals do. From the qualitative analysis of the channeling patterns, we successfully obtained information on the crystallographic sites of the constituent elements such as chemical order. In quasicrystals, information on chemical order is very important not only for determining the struc-
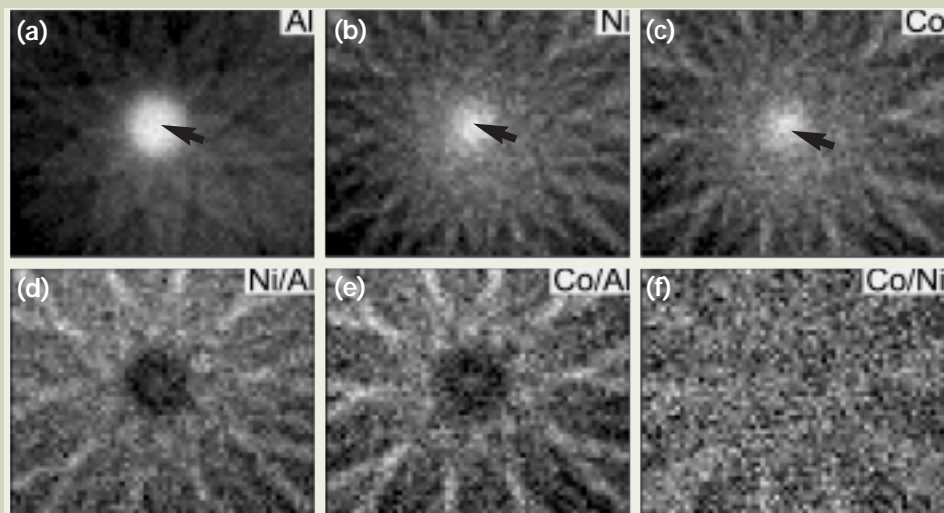

Fig. 4 Channeling patterns of an $Al_{72}Ni_{20}Co_8$ decagonal quasicrystal taken around the decagonal zone-axis using emissions of (a) Al-K, (b) Ni-K and (c) Co-K. The zone-axis center is indicated by the arrow in each pattern. Ratio patterns of Ni/Al, Co/Al and Co/Ni are shown in (d-f). The Al pattern shows different contrast from those of TM as clearly seen in (d) and (e). Only faint contrast on the noise in (f) indicates that Co and Ni are distributed randomly across the same set of sublattice sites.
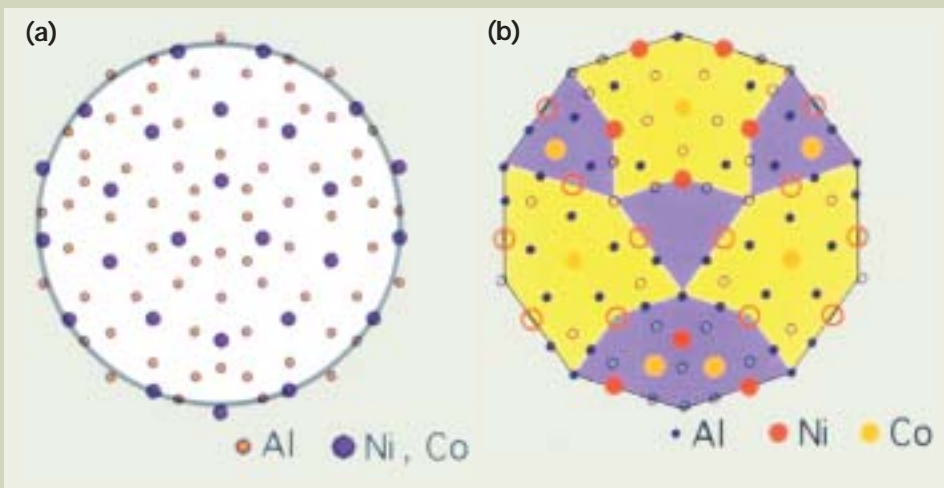

Fig. 5 Structural models of atom clusters of $Al_{72}Ni_{20}Co_8$ (a) without any chemical order between Ni and Co and (b) with a chemical order between the TMs.

ture but also for revealing the formation mechanism of the unique structures of the quasicrystals. One of the problems of ALCHEMI at the present time is the low efficiency of the X-ray detection. Improvement in the detection solid angle and counting rate is needed for more accurate quantitative analysis. In the future, ALCHEMI will be applied not only for the determination of the site of dilute impurities but also for the structural analysis of structurally complex materials such as quasicrystals and even for holography [28].
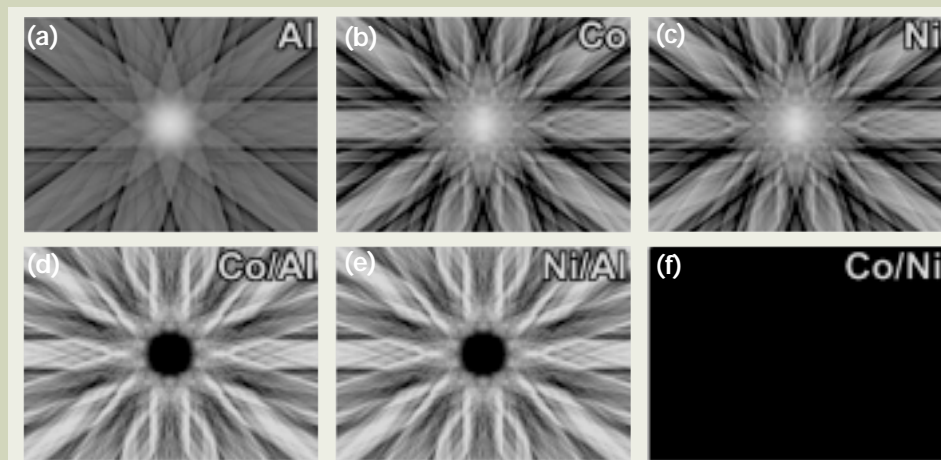

Fig. 6 Channeling patterns simulated from the model without chemical disorder between TMs (Fig. 5(a)). The ratio patterns of TMs/Al show a specific contrast and Co/Ni shows no contrast, being consistent with the experimental result.
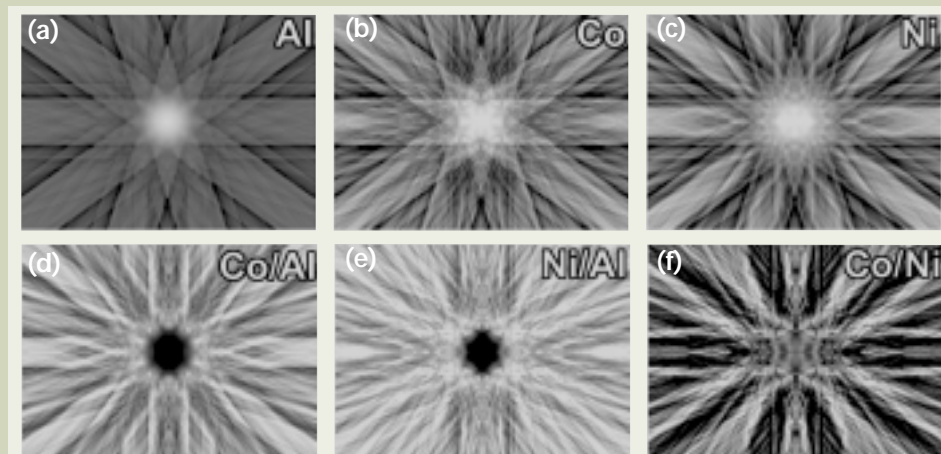

Fig. 7 Channeling patterns simulated from the model with a chemical order between TMs (Fig. 5(a)). Not only the ratio patterns of TMs/Al but also the ratio pattern of Co/Ni show a specific contrast even for a small Ni content of the model, being inconsistent with the experimental result.
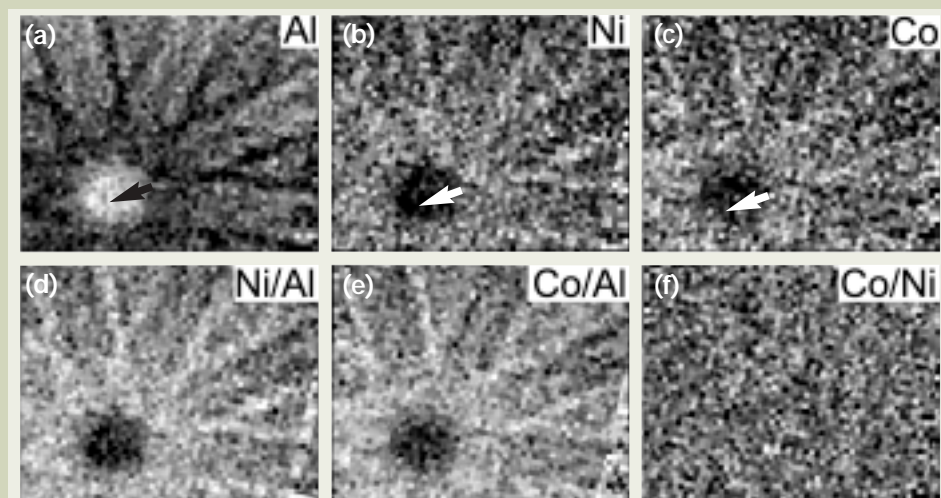

Fig. 8 Channeling patterns of an $Al_{70}Ni_{18}Co_{12}$ decagonal quasicrystal taken around the decagonal zone-axis using emissions of (a) Al-K, (b) Ni-K and (c) Co-K. The zone-axis center is indicated by the arrow in each pattern. Ratio patterns of Ni/Al, Co/Al and Co/Ni are shown in (d-f). Al contrast differs from TM contrast (d and f), and extremely faint contrast on the noise in (f) indicates that a chemical order between Al and TM and chemical disorder between Co and Ni.

References

[1] J. Taftφ and J. C. H. Spence, *Ultramicroscopy*, **9**, 243 (1982)

[2] T. A. Bielicki, *Inst. Phys. Conf. Ser.,* **68**, 67 (1984).

[3] C. J. Rossouw, P. S. Turner, T. J. White and A. J. O'Connor, *Philos. Mag. Lett.,* **60**, 225 (1989)

[4] C. J. Rossouw, C. T. Forwood, M. A. Gibson and P. R. Miller, *Philos. Mag.,* A 74, 77 (1996); ibid, *Philos. Mag.,* A 74, 57 (1996)

[5] K. Saitoh, K. Tsuda, M. Tanaka, K. Kaneko and A. P. Tsai, *Jpn. J. Appl. Phys.,* **36**, L1400 (1997)

[6] K. Saitoh, K. Tsuda, M. Tanaka and A. P. Tsai, *Jpn. J. Appl. Phys.,* **38**, L671 (1999)

[7] K. Saitoh, K. Tsuda, M. Tanaka and A. P. Tsai, *J. Electron Microsc.,* **50**, 197 (2001)

[8] Y. Yan, S. J. Pennycook and A. P. Tsai, *Phys. Rev. Lett.,* **81**, 5145 (1989)

[9] K. Hiraga, T. Ohsuna, W. Sun and K. Sugiyama, *Mater. Trans.,* **42**, 2354 (2001)

[10] K. Hiraga, *Adv. Imag. Elect. Phys.,* **122**, 1, (2002)

[11] E. Abe, K. Saitoh, H. Takakura, A. P. Tsai, P. J. Steinhardt and H.-C. Jeong, *Phys. Rev. Lett.,* **84**, 4609 (2000)

[12] E. Abe, S. J. Pennycook and A. P. Tsai, *Nature,* **421**, 347 (2003)

[13] D. Shindo, K. Hiraga, T. Williams, M. Hirabayashi, A. Inoue and T. Masumoto, *Jpn. J. Appl. Phys.,* **28**, L688 (1989)

[14] S. Ritsch, C. Beeli, H.-U. Nissen, T. Goedecke, M. Scheffer and R.Lueck, *Philos. Mag. Lett.,* **74**, 99 (1996)

[15] S. Ritsch, C. Beeli, H.-U. Nissen, T. Goedecke, M. Scheffer and R. Lueck, *Philos. Mag. Lett.,* **78**, 67 (1998)

[16] A. P. Tsai, A. Fujiwara, A. Inoue and T. Masumoto, *Philos. Mag. Lett.,* **74**, 233 (1996)

[17] A. P. Tsai, A. Inoue and M. Masumoto, *Mater. Trans. JIM,* **30**, 150 (1989)

[18] J. Q. Guo, E. Abe, T. J. Sato and A. P. Tsai, *Jpn. J. Appl. Phys.,* **38**, L1049 (1999)

[19] K. Saitoh, M. Tanaka, A. P. Tsai and C. J. Rossouw, *J. Phys. Soc. Jpn.,* **69**, 2379 (2000)

[20] K. Saitoh, M. Tanaka, A. P. Tsai and C. J. Rossouw, *Ferroelectrics,* **250**, 207 (2001)

[21] K. Saitoh, K. Tsuda and M. Tanaka., *J. Phys. Soc. Jpn.,* **67**, 2578 (1998)

[22] P. J. Steinhardt, H.-C. Jeong, K. Saitoh, M. Tanaka, E. Abe and A. P. Tsai, *Nature,* **396**, 55 (1998)

[23] N. F. Mott and H. Jones, The Theory of the Properties of Metals and Alloys, Dover, New York, (1958)

[24] A. P. Tsai, A. Inoue and T. Masumoto, *Mater. Trans. JIM,* **30**, 463 (1989)

[25] K. Saitoh, M. Tanaka and A. P. Tsai., *J. Non-Cryst. Solids,* **334**, 202 (2004)

[26] K. Saitoh, M. Tanaka and A. P. Tsai, in preparation.

[27] E. Cockayne and M. Widom, *Phys. Rev. Lett.,* **81**, 598 (1998)

[28] J. C. H. Spence and C. Koch, *Phys. Rev. Lett.,* **86**, 5510 (2001)

Electron Spin Resonance Spectroscopy in Food Radiation Research

Mitsuko Ukai

Department of Food Science, Hokkaido University of Education

A review of ESR techniques for studying the properties of radicals induced in γ-irradiated foods is presented. In particular, the relaxation detecting method, as well as long-range field scan scheme, are illustrated in the case of radicals observed in irradiated pepper. The determination method for spin concentration of radicals is given for the quantitative estimation of quantum yield of radiation on foods.

Introduction

The use of the sterilization technology such as irradiation of various electromagnetic waves and rays of elementary particles is gaining wide applications. It allows extension of the shelf life of foods [1]. In practice, dried-food and agricultural products are over treated, and researchers suggest that dosage should be reduced to the levels much below that recommended by FAO/IAEA/WHO Standards for irradiated foods, *i.e.*, 10 kGy [2].

It has been seen that while irradiation kills pathogens, it can induce free radicals that could threaten health. Electron spin resonance (ESR) spectroscopy techniques have been applied for the evaluation of irradiation treatment to a wide variety of foods [3-8]. ESR techniques are specific, rapid and simple to detect radicals contained in the foods. The greatest advantage of ESR is that it is a nondestructive testing method. Thus, it allows the food samples to be reanalyzed and reconfirmed. In fact, ESR has been accepted as a standard method (Committee Europe de Normalization: CEN) in the EU community. ESR has become increasingly popular in food control laboratories all over the world.

Here, we will reveal the existence of free radicals in irradiated pepper using various ESR techniques. Thereby, we can determine the existence of the radiation-induced free radicals in the pepper by comparison with non-irradiated pepper. We shall further estimate the spin concentration in irradiated pepper.

Experimental
Materials

The pepper specimen in the present study is black pepper commercially available in Japan,

Hakodate 040-8567, Japan
E-mail : mitsuko@cc.hokkyodai.ac.jp

bottled in glass (18 g) and stored at room temperature. The specimen was sealed in the ESR sample tube (JEOL) with the amount of 300 mg in either vacuum or air.

Irradiation conditions

Irradiation was carried out at the Japan Atomic Energy Research Institute (Takasaki Research Institute) at room temperature (*ca.* 300 k). The dose level of the γ-ray was controlled by the irradiation period. We selected the three dose levels, *i.e.*, 10, 30 and 50 kGy following the FAO/IAEA/WHO Standards.

ESR spectroscopy

ESR measurements were carried out using two ESR spectrometers (JEOL, JES-FE1XG and JES-FA200). All the ESR spectra were recorded at the X-band (9.3 GHz). For careful detection of all the radical species in the pepper, we employed two kinds of field sweep, 250 ± 250 mT and 340 ± 100 mT. In order to determine the electron relaxation behavior of radicals in the pepper, we varied the microwave field strength 1–196 mW to obtain progressive saturation behavior (PSB). Field modulation/demodulation was operated at 100 kHz. All the ESR measurements were done at room temperature.

Spin concentration was determined using TEMPOL (2.2.6.6-Tetramethylpineridine-N-oxyl) as a standard sample.

Results
Spectral feature of ESR signals

Figure 1 shows the ESR spectrum of the black pepper before irradiation. It consists of three signal components. The signal found at g = 4.0 originates from a transition metal ion, *i.e.*, Fe^{3+}. The sharp intense signal found at g = 2.0 is due to the organic free radical that has resulted from either biochemical or radiation induced

reactions [4]. Furthermore, we detected a huge sextet of hyperfine lines that is attributable to Mn^{2+} ion.

Hyperfine structure of Mn^{2+} ion in pepper

To evaluate hyperfine constant (hfc) of Mn^{2+} ion in the pepper samples, we employed two methods, either taking the summits or the maximum slope of each peak. Those methods yielded the identical hfc of *ca.* 7.4 mT for various peppers. This value is similar to the hfc for Mn^{2+} ion in various metallo-proteins, such as Mn superoxide dismutase [9].

Progressive saturation behaviors

Figures 2A and **2B** demonstrate variations of the peak intensities of P_1 and P_2 shown in Fig. 1. Both figures show that the P_1 signal saturates more readily than P_2. **Figure 2C** shows the intensity ratio between P_1 and P_2. The peak intensity of the organic free radical component decreases in a monotonic fashion. In fact, Fig. 2 indicates that P_1 saturates promptly as compared with P_2. This suggests that P_1 has a character of an organic free radical, because P_2 is attributed to Mn^{2+} that may possess the shorter relaxation times.

Irradiation effects

Figure 3 shows the ESR spectra of the black pepper after the γ-irradiation with 10, 30 and 50 kGy. The sharp intense signal at g = 2.0, *i.e.*, the P_1 signal increases with the degree of irradiation.

Two new peaks were induced symmetrically on the both sides of the P_1 signal by the irradiation (indicated by arrows in the bottom figure).

According to the theory of radical production in solid by irradiation, a linear relationship is expected between the irradiation dose and the radical yield. Thus the linear extrapolation

Fig. 1 An ESR spectrum of black pepper before irradiation. The spectrum was recorded by the magnetic field swept over 500 mT.

yields an irradiation dose that may be used for the sterilization.

Figure 4 demonstrates the PSB of the irradiated black pepper, which is more complicated than that of the non-irradiated pepper shown in Fig. 2. This is due to the production of new radicals by the irradiation.

Spin concentration

Figure 5 shows the spin concentration of the organic free radical in the irradiated black pepper obtained using the standard TEMPOL spectrum. Comparing the doubly integrated value (indicated by red line) of the two original spectra, the amount of the radical in the irradiated pepper was determined to be 2.4–2.8×10^{16} spins/g [10].

Discussion

ESR evidences of multi-component radical species in pepper

As described above in the result section, we have found signals composed of three species in the X-band ESR spectrum of the black pepper before γ-irradiation. First, we noted a signal at g = 2.0 that is due to an organic free radical [5-9]. Unlike other two signals, the P_1 signal quite readily saturates, and thus possesses a long relaxation time, which reflects the existence of an organic free radical.

Second, we observed a signal at g = 4.0, and no other low field signals at g = 6.0 nor 3.0. This indicates that ferrous (Fe^{3+}) ion may exist. Theoretically, the signal which appears at g = 4.28 is known to be the ESR signal due to the E-tensor term of Fe^{3+} ion [9]. Since there is no signal at g = 6.0, Fe^{3+} ion is due to the non-hem origin.

Third, we found a huge sextet of hyperfine lines centered at g = 2.0, which is clearly due to Mn^{2+} ion. The evaluated hyperfine coupling constant was *ca*. 7.4 mT, which is similar to the
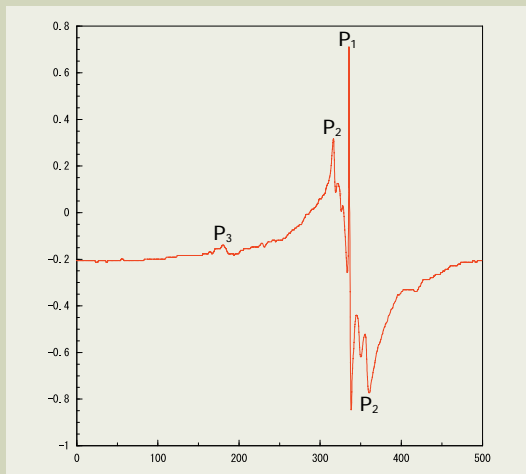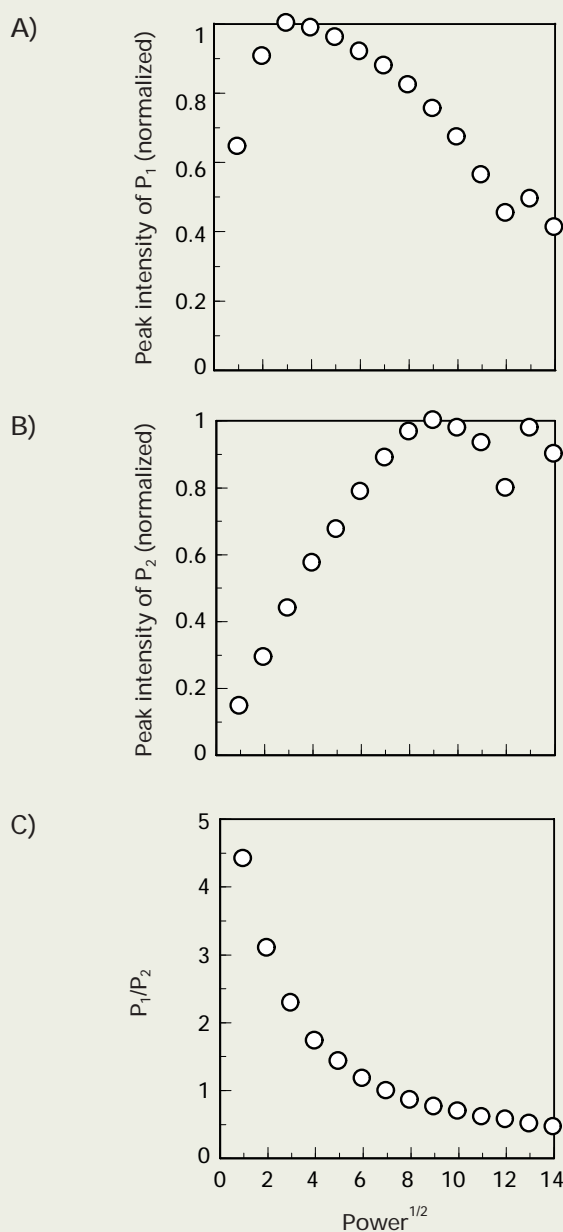

Fig. 2 Progressive saturation behaviors of ESR signals from the unirradiated black pepper. A) P_1, B) P_2 signals and C) a ratio of P_1/P_2 are plotted as a function of the root of microwave power.

isotropic coupling of Mn^{2+} ion dispersed in MgO powder (*ca*. 8.7 mT). The residual difference is due to the modified ligand field.

The three signal species found in the black pepper before irradiation behave independently under the progressive power saturation [11]. Namely, there are essentially no inter-radical interactions. This fact somewhat contradicts the comments made by Stewart [3] who suggested that the resonance position of Mn^{2+} signal interferes with the P_1 signal.

ESR evidences of the irradiated black pepper

Upon irradiation, two new peaks were found at the symmetric positions of the both sides of the P_1 signal (shown in Fig. 3). The similar kind of signal has been reported by Raffi *et al.* [4] who have observed in the ESR spectra of the strawberries irradiated with the dose of 2 kGy. Unlike the pepper sample, the irradiated strawberries showed only one peak in the lower field with respect to the P_1 peak position (see Fig. 3 in Ref. 4).

Although the two signals appeared simultaneously after irradiation, their relaxation behaviors are not the same as seen in the PSBs of the organic free radicals [5, 6]. This is due to the ESR signals that originated from the different radicals. To identify radical species, further ESR data should be collected by electron nuclear double resonance spectroscopy.

Radiation effects were also visible judging from the variation of the peak intensity of the P_1 signal as a function of the radiation dose. A linear dependence of peak intensity at various dosage of the radiation was observed. We could estimate the initial dosage for the unknown sterilization process by the linear interpolation method, based upon the ESR spectra of the black pepper before irradiation [6].

On the protocol for ESR detection of irradiated foods

Table 1 shows two protocols for the ESR detection of irradiated foods containing cellulose. The parameter values in an ESR protocol were examined by the CEN experts in the beginning of 1990s, and have been finally authorized and used in the EU community.

As seen in the PSBs of the black pepper, the microwave power saturation curves of each signal differ greatly before and after irradiation. This means that one cannot fix the certain value of microwave power, such as 0.4 mW recommended by the CEN protocol. Instead, we would propose the microwave power value at which the intensity ratio of P_1/P_2 meets the threshold or maximum value. Thereby, radical quantity can be measured with high precision when one uses the intensity ratio as a universal constant, because the intensity ratio is uniquely defined in an ESR spectrum.

Perspectives

Among many techniques for irradiated food researches, ESR techniques are the most sensitive method. In particular, ESR techniques for determination of spin concentration and PSB play an important role in food irradiation research and detection method of irradiation

dose in irradiated foods.

Conclusions

1) Using ESR spectroscopy, we revealed three radical components in the commercially available pepper in Japan. However, we found four distinct signals in the same pepper after the irradiation.
2) The ESR spectrum of the non-irradiated pepper is composed of a sextet line centered at g = 2.0, a singlet at the same g-value and a singlet at g = 4.0. The first one is attributable to a signal of Mn^{2+} ion (hfc: 7.4 mT). The second one is due to an organic free radical. The third one is due to the Fe^{3+} ion. Upon irradiation, two new peaks were found at the symmetric positions of the both sides of the organic free radical.
3) The PSB of the ESR microwave power demonstrated a quite different saturation behavior of the radicals. The peak intensity of the free radical component decreases in a monotonic fashion, whereas the Mn^{2+} component substantially keeps its intensity constant. The PSB of the pair peaks that appeared upon irradiation was quite different from that of organic free radicals.
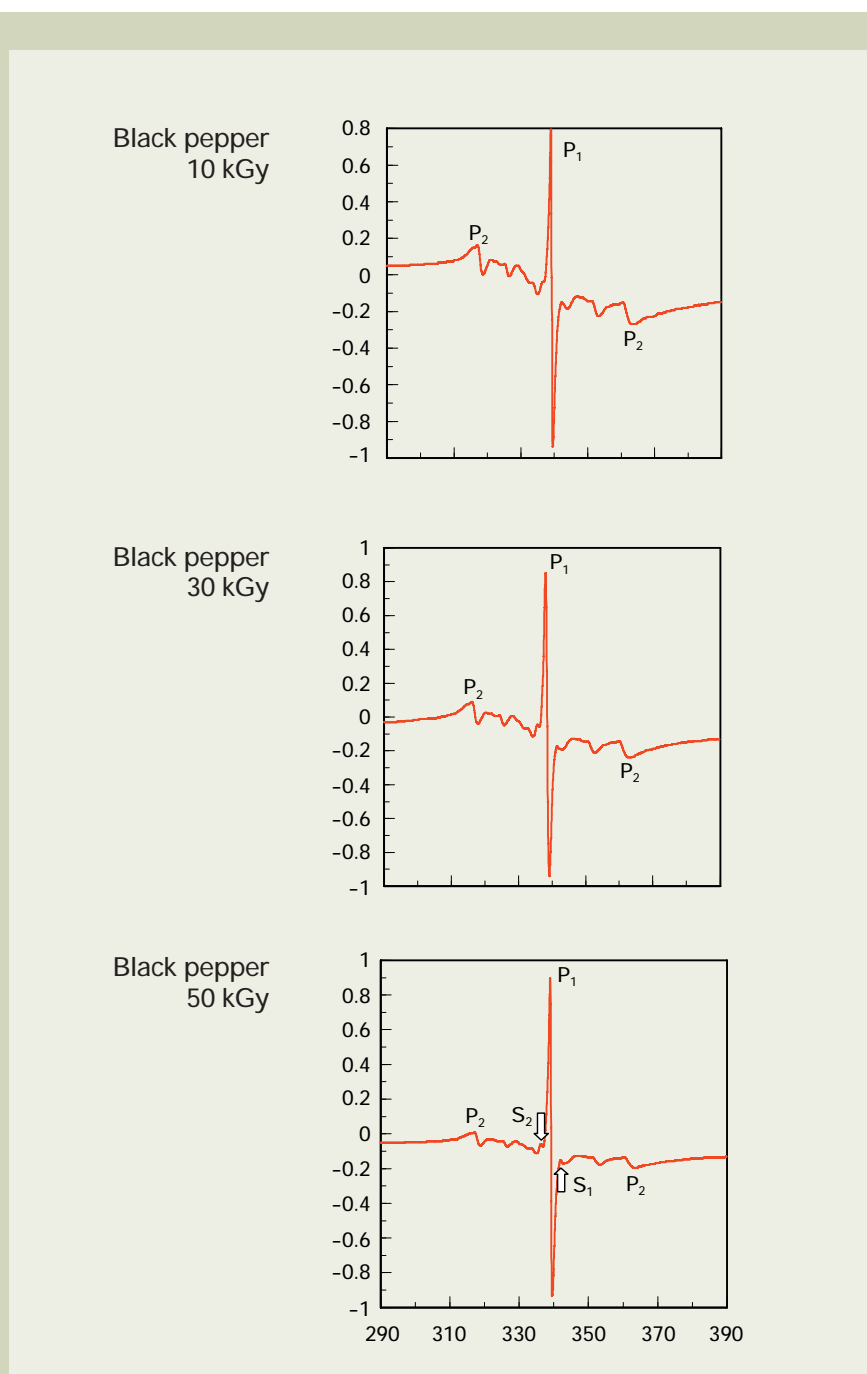

Fig. 3   ESR spectra of black pepper at various irradiation dose levels recorded in the vicinity of g = 2 region.

4) We proposed a new protocol for the ESR detection of irradiated black pepper using the saturation behavior at various microwave power levels. This calls for the major modification of the CEN protocol used in the EU community.

Acknowledgements

References

[1] Farkas, J.: *Radiat. Phys. Chem.*, **25**, 271-280 (1985)
[2] Joint FAO/IAEA/WHO Expert Committee, Wholesomeness of Irradiated Food, *WHO Geneva No. 659* (1981)
[3] Stewart, E. M.: Detection Methods for Irradiated Foods, in Food Irradiation: Principles and Applications (Eds. R. A. Molins), Chap. 14, 347-386 (John Wiley & Sons, New York) (2001)
[4] Raffi, J. et al.: *Appl. Magn. Reson.*, **10**, 357-373 (1996)
[5] Ukai, M. et al.: *Radioisotopes*, **51**, 501-504 (2002)
[6] Ukai, M. et al.: *Appl. Magn. Reson.*, **24**, 1-11 (2003)
[7] Ukai, M. et al.: *J. Food Science*, **68**, 2225-2229 (2003)
[8] Ukai, M. et al.: *Appl. Magn. Reson.*, **25**, 95-103 (2003)
[9] Kotani, M. et al.: Magnetic Resonance in Biochemical Research, 77-96 (Gordon Beach Co., New York) (1977)
[10] Ukai, M.: to be published
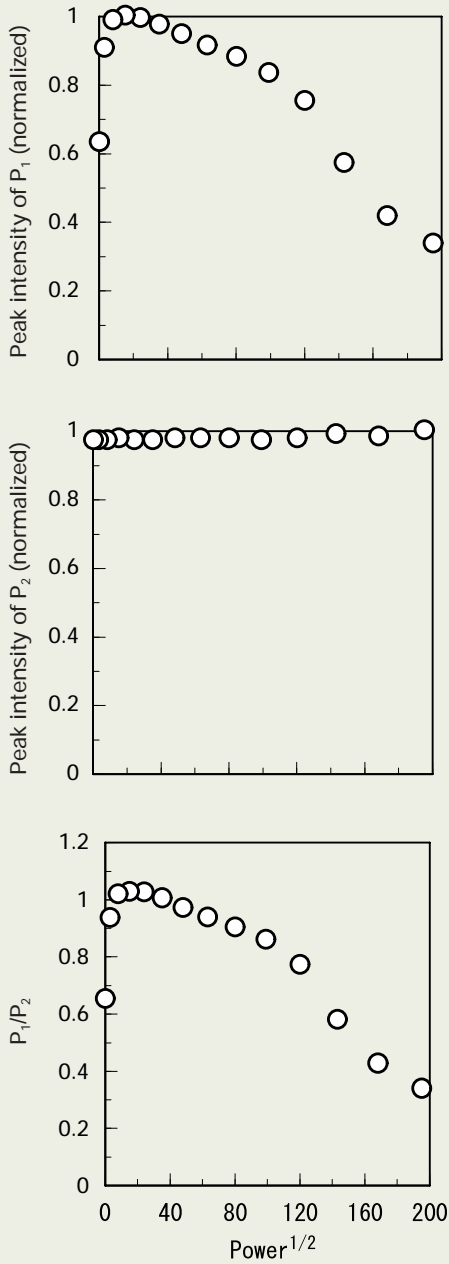[11] Poole, Jr. C. P.: Electron Spin Resonance (Wiley-Interscience, Canada) (1983)

Fig. 4 Progressive ESR saturation behaviors of the P_1 and P_2 signals of the black pepper after irradiation of 10 kGy.
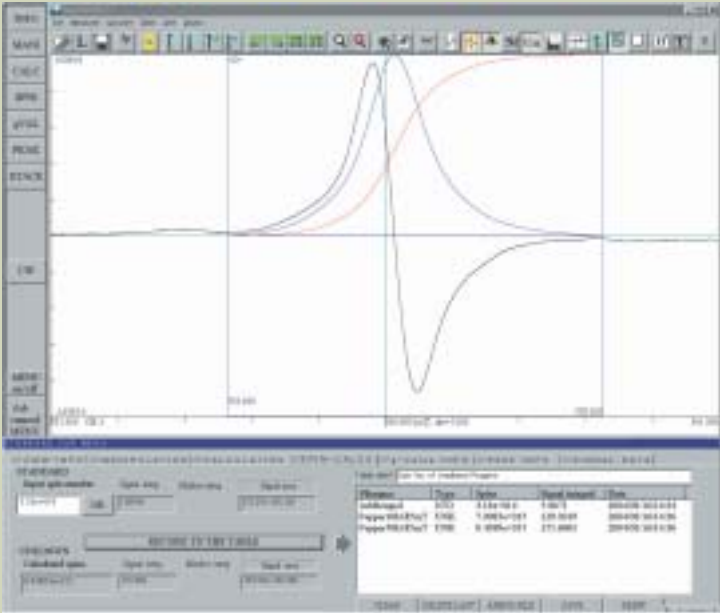

Fig. 5 Spin concentration of the P_1 signal from the irradiated black pepper.

Table 1 Comparison between the new protocol and the CEN protocol fixed for ESR of irradiated foods.

	New protocol	CEN protocol
Sample preparation	300 mg	100 mg
Magnetic field	250 ± 250 mT 340 ± 100 mT	348 mT
Microwave power	Variable $0 \sim 196$ mW	0.4 mW

Cross Section Specimen Preparation Device Using Argon Ion Beam for SEM
−Cross Section Polisher (CP) SM-09010−

Masateru Shibata

Application & Research Center, JEOL Ltd.

Scanning Electron Microscopes (SEMs) have been used for various applications, such as research and development and failure analysis. There are many cases where not only observation of a specimen surface – but also observation of a cross section – is important. Preparation of a cross section depends on the specimen structure, observation purpose, and materials. Various preparation methods are put into practice: cutting, mechanical polishing, microtome, and FIB (Focused Ion Beam) are the major methods. In this discussion, we evaluate a new cross section specimen preparation method using an argon ion beam (hereinafter called the Cross-section Polishing or CP method). We have found that this method is extremely useful for observation of layer structures, interfaces, and crystalline structures of metals, ceramics, and composites. Here, we introduce examples of applications to various types of specimens.

Introduction

Observation of cross sections of complex materials is important to obtain the size of crystal grains, the layer structures, the film thicknesses of reaction layers and the existence of voids. In cross sectional observation, mechanical polishing is generally used to prepare a specimen. However, it is difficult to polish a junction of materials with different hardnesses or a reaction layer formed in the junction into a flat mirror surface by mechanical polishing. Mechanical polishing has several problems as shown in **Fig. 1**: a) if it is applied to materials having different hardnesses, the polished surface becomes uneven as the soft portion is cut faster and more easily, b) if it is applied to soft materials, there are some cases where pieces of hard polish are buried in the material being polished, c) for soft materials, if the material has a void, the material around the void stretches and deforms, d) if the material has a void, pieces of polish get stuck in the void, e) for metals, due to distortion caused by mechanical polishing on the polished surface, the information about the crystal becomes difficult to obtain.

The FIB method is one of the methods known to resolve these problems, and its applications in various fields have been reported. The FIB method is effective for cross section specimen preparation of micro area and thin film specimen preparation, however, it is not effective for preparation of a wide surface area of a specimen.

The CP method that we are introducing here does not incur those problems of mechanical polishing mentioned before, and it enables one to prepare a wider area of a specimen than the FIB method. In addition, required skill is minimal compared with other specimen preparation methods, making it simple for anyone to pre-

a) On material with different hardnesses, the polished surface becomes uneven as the soft portion is cut faster and easier.

b) On soft material, pieces of hard polish can be buried in the material being polished.

c) On soft material with a void, the material around the void stretches and deforms.

d) On material with a void, pieces of polish get stuck in the void.

e) On metals, due to distortion caused by mechanical polishing on the polished surface, information about the crystal becomes difficult to obtain.

Fig. 1   Problems associated with mechanical polishing.

pare a cross section specimen.

Instrument Outline

The appearance of the instrument is shown in **Fig. 2**, and the principal specifications are listed in **Table 1**. Because it employs the Penning type argon ion gun which has a long life, it can obtain high current density. It enables one to prepare cross sections consistently. The accelerating voltage is changeable between 2 and 6 kV and the use of low-energy argon ions minimizes damage to the specimen. A turbo-molecular pump and a rotary pump have been employed for the evacuation system and the instrument can be placed wherever the space of an office desk is available.

Features of the Cross Section Polisher

- Provides a good cross section of even a composite of soft and hard materials.
- Minimizes distortion of the polished surface, enabling one to observe crystalline contrast clearly.
- Polishes an area several hundred micrometers in width, much larger than the FIB method can polish.
- As it is not mechanical polishing, polish never embeds in the polished surface.
- Low running cost
- Ease of operation
- Eco-friendly, free of drainage and waste liquids

Application Examples
Card edge connector

Figure 3 shows the cross section SEM micrograph of a card edge connector prepared by the CP method. The cross section prepared by mechanical polishing is shown in **Fig. 4** for
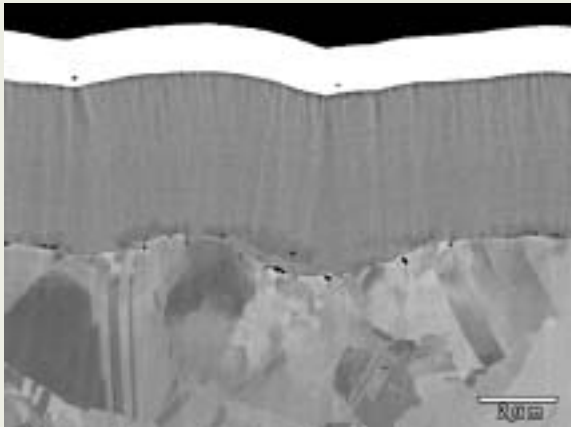

Fig. 2   Cross section polisher (CP) SM-09010.

Table 1 Principal specifications

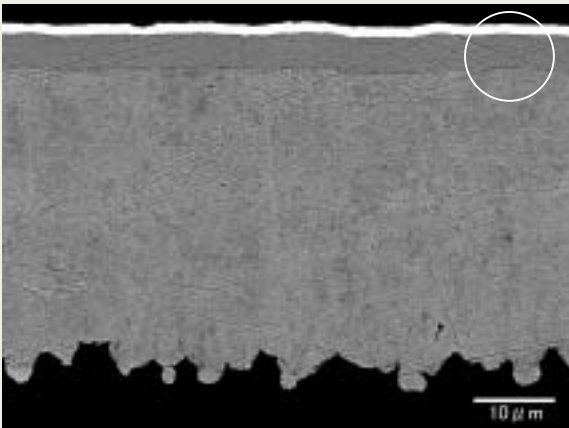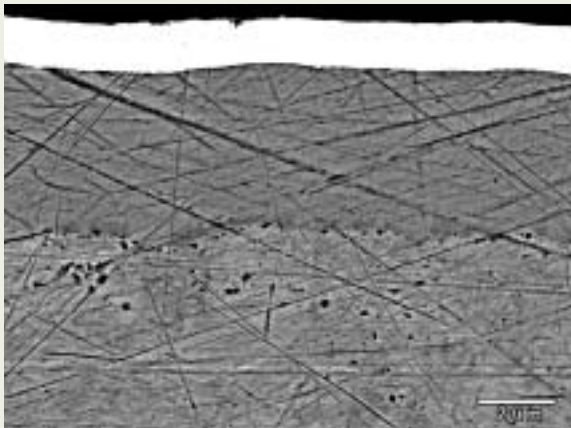| Ion gun	Penning type argon ion gun
Accelerating voltage	2 to 6 kV
Ion beam diameter	500 μm (FWHM)
Milling rate	1.3 μm/min (6 kV, silicon, 100 μm from edge)
Maximum specimen size	11 mm (W)×10 mm (D)×2 mm (H)
Specimen stage	X : ±3 mm, Y : ±3 mm
Specimen alignment	±5°
Vacuum system	TMP, RP
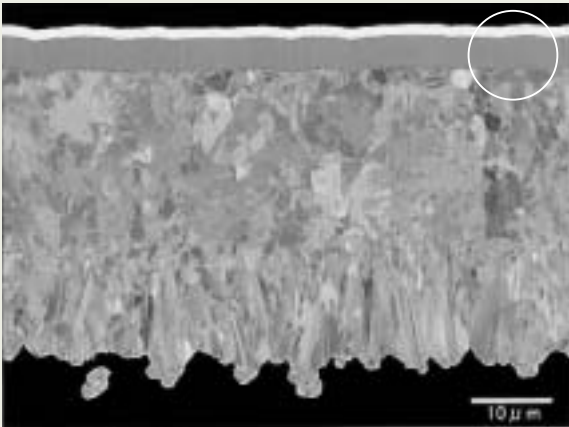
Fig. 3   CP method (Backscattered electron image).

Fig. 4   Mechanical polishing (Backscattered electron image).

comparison. In Fig. 3, the specimen consists of resin/Cu (first layer)/Cu (second layer)/NiP/Au from the bottom in order (left), and the surface layers are composed of soft metals of Au and Cu, and hard metal NiP (right). With the CP method, 1) crystalline contrast in the Cu portion, 2) lateral stripes arising during NiP film formation can be clearly observed. On the other hand, the specimen produced by mechanical polishing in Fig. 4 fails to show good results due to polish damage.

Bonded gold wire

A cross section micrograph of a gold wire bonded on a gold plated pad is shown in **Fig. 5**. The condition of the bonded part, film thickness, voids, and crystalline contrast can be observed. **Figure 6** shows a cross section and lateral section of the same gold wire. We can observe that the size of the crystal grains varies both in the cross section and lateral section micrographs.

Flexible printed circuit

A cross section SEM micrograph of a flexible printed circuit is shown in **Fig. 7**. The specimen consists of resin/Cu/Ni/solder. a) is a good cross section specimen about 350 μm wide, and we can observe voids in the solder. b) shows the clear difference between crystal grains of the Cu and Ni portions. The CP method provides a good result, even if the specimen is a composite of resin and metals.

IC analysis

Figure 8 shows a cross section SEM micrograph of a molded IC. **Figure 9** shows a magnified image and EDS maps of the Cu terminal connecting portion. On the Si substrate of the molded IC, various materials, such as SiO_2, SiN, Au, Sn, Al (wiring), and Cu (terminal), are contained. It is seen that a good cross sec-
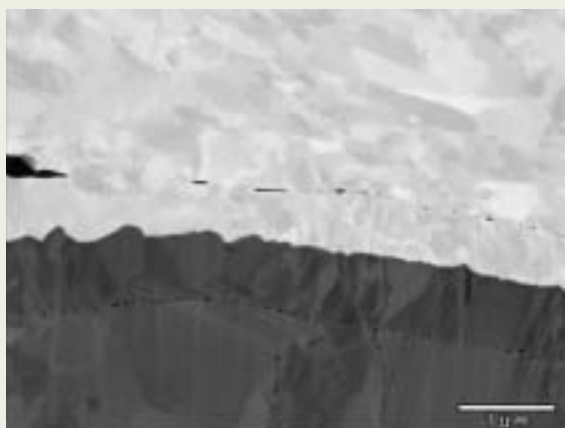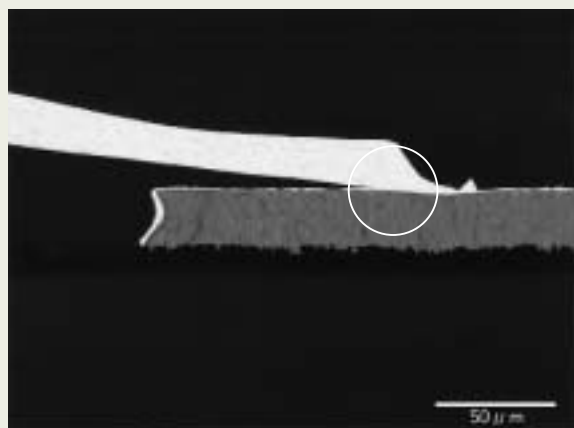

Fig. 5   Bonded gold wire (Backscattered electron image).
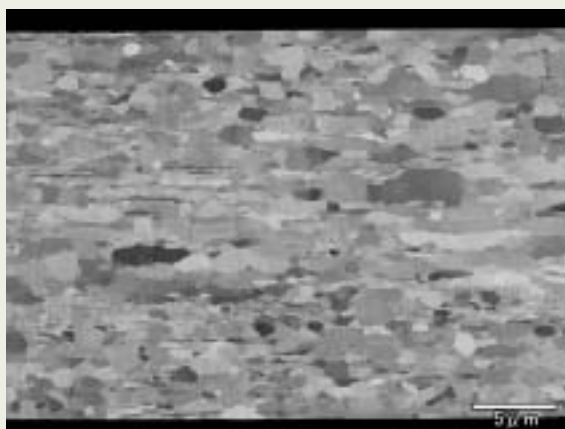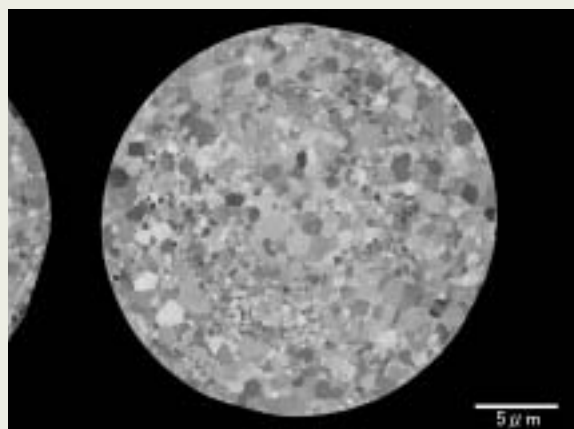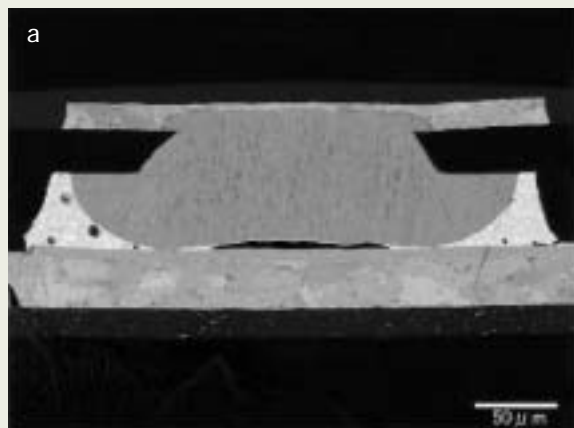

Fig. 6   Cross section and lateral section of the same gold wire (Backscattered electron image).
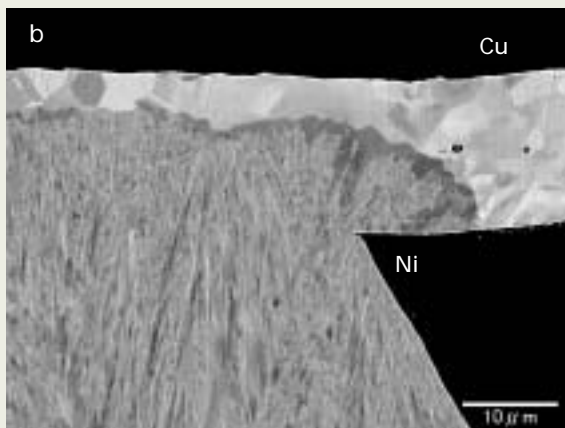

Fig. 7   Flexible printed circuit (Backscattered electron image).

tion is obtained even from composites with different hardnesses.

Figure 10 shows an X-ray spectrum from the area where EDS mapping was performed. As seen from the spectrum, the peak of the ion source, Ar, cannot be found. Of course, depending on the constituent elements, the amount of Ar ion implantation varies, but this IC specimen has so little Ar ion implantation that we can disregard it. With the FIB method, there are cases where the ion source, Ga, is detected. It is necessary to take the overlap of peaks into consideration, depending on the analysis elements.

Cross section preparation of ceramic powder specimen

Figure 11 shows a SEM micrograph of the surface of a ceramic powder specimen, and **Fig. 12** shows a cross section SEM micrograph. The inner cavity that was not seen by the surface observation can be observed clearly in Fig. 12. For cross section observation of powder specimens, it is often important to observe the inner structure, the differences between specimens, and the core of the powder. In these cases, a cross section specimen that allows observation of a large number of powder grains is needed and so the CP method is considered to be extremely suitable.

Conclusion

The cross section specimen preparation method using an argon ion beam is one of the excellent methods among various cross section specimen preparation methods. It enables one to easily create cross sections of polymers, metals, ceramics, and composites with few artifacts. It is suitable for not only image observation but also EDS analysis, and it can prepare a cross section from a specimen area much wider than the FIB method can.
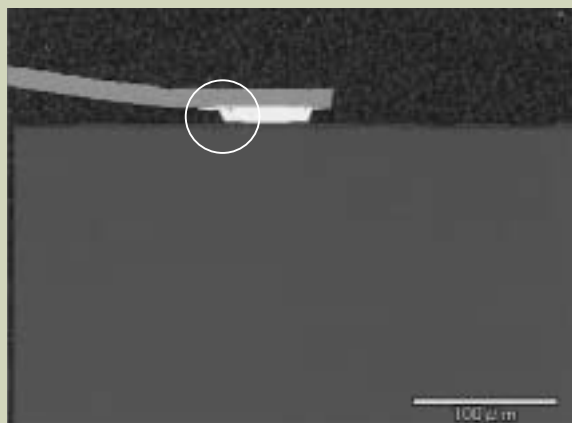
Fig. 8   Cross section of IC (Backscattered electron image).

Backscattered electron image

Elemental map of nitrogen

Elemental map of oxygen

Elemental map of aluminum

Superimposed image of N, O, and Al

Fig. 9   EDS elemental maps on Cu bonding region.
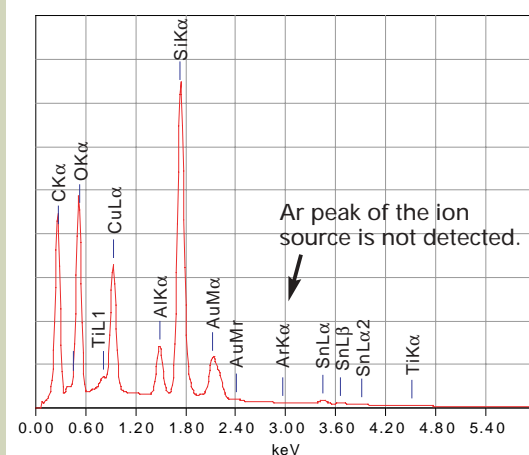
Fig. 10   Spectrum from the elemental mapping area.

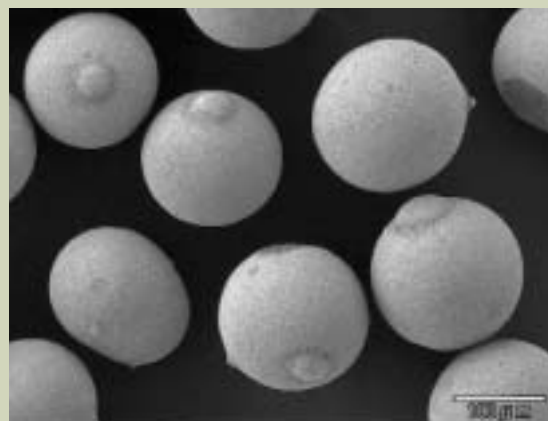Fig. 11   Surface of ceramic powder (Secondary electron image).
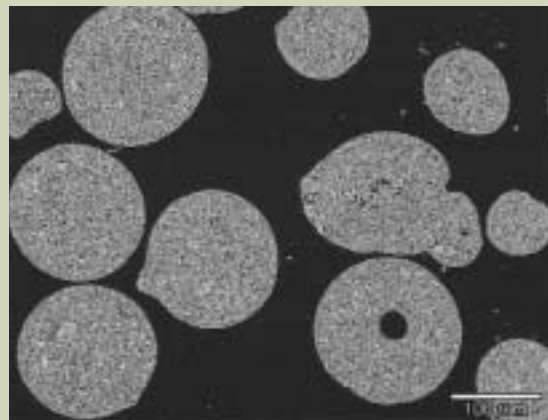

Fig. 12   Cross section of ceramic powder (Backscattered electron image).

Introduction of New Products

Electron microscope

JEM-2100

The JEM-2100 is an analytical electron microscope which not only offers transmission electron microscope (TEM) images and diffraction patterns, but also incorporates a computer control system which can integrate a scanning transmission electron microscope (STEM) image observation device, an energy dispersive X-ray spectrometer (JED-2300T), and an electron energy-loss spectrometer (EELS) in any combination.

High stability: High stability of the high voltage and beam current, together with the excellent lens system, achieves a high resolution of 0.19 nm at 200 kV.
New frame structure for the column: This new base frame greatly reduces the effect of vibration on the instrument.
Analytical electron microscope: The EDS system uses a new detector which is designed for a solid angle of 0.28 sr and a take-off angle of 24.1°, allowing highly accurate analysis and quick data acquisition.
Specimen stage: The new goniometer stage achieves precise specimen movement at nanometer scales.
Expandability: The main computer system can integrate a STEM image observation device, an EDS system, and an EELS device, and offer ease of operation. You can also share the obtained information with other PCs using the networking capabilities of the computer system.

Spherical aberration correctors for STEM and TEM

EM-20900CSS
EM-20910CST

The EM-20900CSS is a spherical aberration (Cs) corrector system for probe-forming (STEM) and EM-20910CST is for image-forming (TEM). Cs correction is a breakthrough technique to improve the limit of resolution for structure observation and chemical analysis. The Cs correctors can be attached to a 200 kV high-resolution microscope with a field emission gun (JEM-2100F, JEM-2200FS). Using these systems, the spherical aberrations of the image and probe-forming lens systems can be set to a desired value. Residual aberrations up to the third order are automatically corrected by the PC controlled system. In the case of an ultra-high-resolution polepiece (URP), the resolutions of 200 kV electron microscope can be enhanced to be 0.1 nm on STEM and 0.12 nm on TEM.

- Automatic aberration correction procedure by computer control
- Cs can be set to a desired value (from –0.5 mm to 0.5 mm in a URP case.)
- Second order aberration coefficients (coma, three-fold astigmatism) can be reduced to < 0.1 µm. Third order aberration coefficients (star aberration and four-fold astigmatism) can be reduced to < 5 µm

Introduction of New Products

TEM Tomograph system
EM-05500TGP

TEM Tomograph system performs 3-dimensional (3D) reconstruction from a tilted image series. Software – RECORDER – features auto-focus, automatic position compensation, automatic exposure time estimation, the automatic image recording and the automatic specimen tilting. Using a TEM with an Ω type energy filter, high quality 3D reconstruction can be performed by high contrast zero-loss-energy images. 3D reconstruction using algorithm based on the CT technique is performed after further precise position compensation and determination of a tilt-axis direction of a series of images. Furthermore, a beautiful 3D reconstruction image can be obtained by removal of the artifacts originating in the missing corn. You can observe 3D structure intuitively at high speed by visualization of the reconstructed 3D data in a dedicated PC.

- Specimen preparation   Slice section (RuO_4 staining).
- Instrument   JEM-2010 electron microscope & TEM Tomograph system
- Photographic conditions -60 deg. to $+60$ deg. (2.5 deg. steps)

Specimen courtesy of Dr. H. Hasegawa of Kyoto University and Dr. H. Jinnai of Kyoto Institute of Technology.
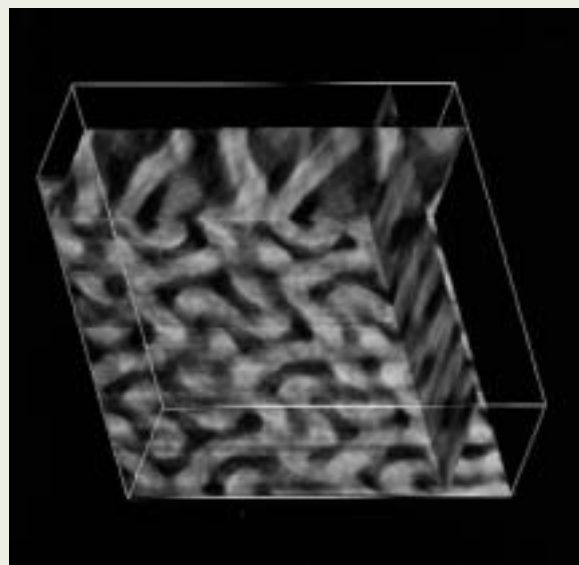
Reconstruction image of gyroid crystal (Polymer). Image area: $70 \times 100 \times 25$ nm.

Energy-dispersive x-ray fluorescence spectrometer
JSX-3000

This Energy-Dispersive X-ray Fluorescence Spectrometer (EDXRF) helps you comply with environmental regulations for hazardous substances such as the RoHS or ELV directive in the EU. This system includes an electronically cooled semiconductor detector as standard, making liquid nitrogen unnecessary. Of course, this system carries out the general-purpose analyses.

- Measurement element range:
  Na to U
- X-ray generator:
  Rh target, 50 kV, 1 mA (50 W), Fail-safe function provided, Primary X-ray filters: 4 including Open
- Specimen chamber:
  300 mm diameter $\times$ 50 mm, automatic Open/close
- Detector:
  Electronically-cooled Si (Li) semiconductor detector, DPP (digital pulse processor) counting method
- Data processing:
  Windows PC, OS: Windows XP, 17 inch liquid crystal display, color printer

Introduction of New Products

The ultimate ultra high resolution FE SEM
JSM-7700F

The JSM-7700F is developed as an ultra high resolution SEM for observation of nano-structures on the surface of a specimen with high fidelity.

The resolution of 0.6 nm is guaranteed at both 5 kV with the aberration correction and 15 kV without the aberration correction. The aberration corrector corrects both spherical and chromatic aberrations.

The side entry type specimen stage commonly used on TEMs is extremely stable even at a magnification of × 1,000,000.

A specimen is kept clean during observation with the completely dry pumping system and the newly developed liquid-nitrogen-free anti-contamination trap.

- Resolution   0.6 nm (5 kV), 1.0 nm (1 kV)
- Accelerating voltage   0.5 to 30 kV
- Magnification   ×25 to 2,000,000
- Specimen size   5 mm × 18 mm × 8 mm thick, 5 mm × 25mm × 4 mm thick
- Specimen movements   X=2.5 mm, Y=24 mm, Z=1 mm T=±45° (4 axes : motor controlled)

Ultra high resolution FE SEM at extreme low voltages
JSM-7401F

The JSM-7401F is the latest high performance field emission scanning electron microscope equipped with the newly developed Gentle Beam and r-filter. The Gentle Beam produces ultra high resolution at low electron energies down to 0.1 kV and enables one to observe true fine surface structures. The r-filter freely mixes secondary electrons and backscattered electrons to observe contrast varying from true secondary images to compositional images.

The large 18.1 inch LCD monitor displays a clear high definition live image with 1,280 × 1,024 pixels.

The fully automated electron optics enables one to achieve the high performance easily.

The large specimen chamber designed for a large variety of detectors can accommodate up to a 200 mm diameter specimen.

- Resolution   1.0 nm
- Accelerating voltage   0.1 to 30 kV
- Magnification   × 25 to 1,000,000
- Specimen size   150 mm dia.
- Specimen movements   X=70 mm (motor or manual driven)
  Y=50 mm (motor or manual driven)
  Z=1.5 to 25 mm, T=− 5 to 70°
  R=360° (motor driven)

Introduction of New Products

High performance general-purpose SEMs with a large specimen chamber
JSM-6480 series

The JSM-6480 series SEM is a flexible multi-purpose SEM. Multiple users can customize the operation GUI for their efficient operations with optimum performance. The well accepted user friendly GUI has been upgraded to be more compatible with multiple user environment. A unique addition is SmileShot, which sets the SEM for the optimum condition by simply selecting the conditions of a specimen. The large specimen chamber with the five-axis motor controlled specimen stage affording large movements can readily handle a large variety of specimens. The JSM-6480LV, which has the low vacuum mode built-in, can observe and analyze non-conductive specimens without any pre-treatment.

The JSM-6480A and JSM-6480LA are the analytical scanning electron microscopes with a JEOL made EDS elemental analyzer embedded. These compact SEM systems offer comfortable seamless operation from observation to elemental analysis.

- Resolution   3.0 nm (HV mode), 4.0 nm (LV mode)
- Accelerating voltage   0.5 to 30 kV (56 steps)
- Magnification   ×5 to 300,000
- Specimen size   203 mm dia. (max.)
- Specimen movements   X=125 mm, Y=100 mm, Z=5 to 80 mm
  T=−10 to 90°, R=360°

JSM-6480LV

High performance general-purpose scanning electron microscopes
JSM-6380 series

The JSM-6380 series SEM is a user-friendly high performance general-purpose scanning electron microscope composed of the fully automated high performance electron optics and the newly developed multi-user compatible operation software. The JSM-6380LV, which has the low vacuum mode built-in, can observe and analyze non-conductive specimens without any pre-treatment.

The JSM-6380A and JSM-6380LA are the analytical scanning electron microscopes with a JEOL made EDS elemental analyzer embedded. These compact SEM systems offer comfortable seamless operation from observation to elemental analysis.

- Resolution   3.0 nm (HV mode), 4.0 nm (LV mode)
- Accelerating voltage   0.5 to 30 kV (53 steps)
- Magnification   ×5 to 300,000
- Specimen size   150 mm dia. (max.)
- Specimen movements   X=80 mm, Y=40 mm, Z=5 to 48 mm
  T=−10 to 90°, R=360°

JSM-6380LV

Certain products in this brochure are controlled under the "Foreign Exchange and Foreign Trade Law" of Japan in compliance with international security export control. JEOL Ltd. must provide the Japanese Government with "End-user's Statement of Assurance" and "End-use Certificate" in order to obtain the export license needed for export from Japan. If the product to be exported is in this category, the end user will be asked to fill in these certificate forms.

DNV
ISO 9001:2000 & 14001:1996 REGISTERED FIRM
DNV Certification B.V., THE NETHERLANDS
Accredited by the RvA
JEOL ISO 9001 Certificated
ISO 14001 Certificated

JEOL Ltd.
1-2 Musashino 3-chome Akishima Tokyo 196-8558 Japan Sales Division ☎(042)528-3381 FAX(042)528-3386

http://www.jeol.co.jp/

ARGENTINA
COASIN S. A. C. I. yF.
Virrey del Pino 4071,
1430 Buenos Aires, Argentina
Telephone: 54-11-4552-3185
Facsimile: 54-11-4555-3321

AUSTRALIA & NEW ZEALAND
JEOL (AUSTRALASIA) Pty. Ltd.
Unit 9, 750-752 Pittwater Road,
Brookvale, N. S. W. 2100, Australia
Telephone: 61-2-9905-8255
Facsimile: 61-2-9905-8286

AUSTRIA
LABCO GmbH
Dr.-Tritremmel-Gasse 8,
A-3013 Pressbaum, Austria
Telephone: 43-2233-53838
Facsimile: 43-2233-53176

BANGLADESH
A.Q. CHOWDHURY & CO. Pvt. Ltd.
Baridhara Central Plaza 87, Suhrawardy Avenue
2nd Floor Baridhara,
Dhaka-12129 Bangradesh
Telephone: 880-2-9862272, 9894583
Facsimile: 880-2-988070

BELGIUM
JEOL (EUROPE) B. V.
Zaventem/Ikaros Business Park,
Ikaroslaan 7A, B-1930 Zaventem, Belgium
Telephone: 32-2-720-0560
Facsimile: 32-2-720-6134

BRAZIL
FUGIWARA ENTERPRISES
INSTRUMENTOS CIENTIFICOS LTDA.
Avenida Itaberaba,3563
02739-000 Sao Paulo, SPI Brazil
Telephone: 55-11-3983-8144
Facsimile: 55-11-3983-8140

CANADA
JEOL CANADA, INC.
(Represented by Soquelec, Ltd.)
5757 Cavendish Boulevard, Suite 540,
Montreal, Quebec H4W 2W8, Canada
Telephone: 1-514-482-6427
Facsimile: 1-514-482-1929

CHILE
TECSIS LTDA.
Avenida Holanda 1248,
Casilla 50/9 Correo 9, Providencia, Santiago, Chile
Telephone: 56-2-205-1313
Facsimile: 56-2-225-0759

CHINA
JEOL LTD., BEIJING OFFICE
Room No. B2101/2106,
Vantone New World Plaza,
No. 2 Fuwai Street, Xicheng District,
Beijing 100037, P. R. China
Telephone: 86-10-6804-6321/6322/6323
Facsimile: 86-10-6804-6324

JEOL LTD., SHANGHAI OFFICE
Sanhe Building 11F2, Yan Ping Road,
No. 121,Shanghai 200042, P.R. China
Telephone: 86-21-6246-2353
Facsimile: 86-21-6246-2836

JEOL LTD., GUANG ZHOU OFFICE
S2204 World Trade Center Building
371-375, Huang Shi East-Road, Guang Zhou,
510095, P, R. China
Telephone: 86-20-8778-7848
Facsimile: 86-20-8778-4268

JEOL LTD., WUHAN OFFICE
Room. 3216, World Trading Bld., 686 Jiefang Street,
Hankou, Wuhan, P. R. China
Telephone: 86-27-8544-8953
Facsimile: 86-27-8544-8695

FARMING LTD.
Unit 1009, 10/F., MLC Millennia Plaza
663 King's Road, North Point, Hong Kong
Telephone: 852-2815-7299
Facsimile: 852-2581-4635

CYPRUS
MESLO LTD.
Scientific & Laboraty Division,
P. O. Box 27709, Nicosia Cyprus
Telephone: 357-2-666070
Facsimile: 357-2-660355

EGYPT
JEOL SERVICE BUREAU
3rd Fl. Nile Center Bldg.,
Nawal Street, Dokki, (Cairo), Egypt
Telephone: 20-2-335-7220
Facsimile: 20-2-338-4186

FRANCE
JEOL (EUROPE) S. A.
Espace Claude Monet,
1, Allee de Giverny 78290
Croissy-sur-Seine, France
Telephone: 33-13015-3737
Facsimile: 33-13015-3747

GERMANY
JEOL(GERMANY)GmbH
Oskar-Von-Miller-Strasse 1,
85386 Eching Germany
Telephone: 49-8165-77346
Facsimile: 49-8165-77512

GREAT BRITAIN & IRELAND
JEOL (U.K.) LTD.
JEOL House, Silver court, Watchmead, Welwyn
Garden City, Herts AL7 1LT., England
Telephone: 44-1707-377117
Facsimile: 44-1707-373254

GREECE
N. ASTERIADIS S. A.
56-58, S. Trikoupi Str. P.O.Box 26140
GR-10022 Athens, Greece
Telephone: 30-1-823-5383
Facsimile: 30-1-823-9567

INDIA
Blue Star LTD. (HQ)
Analytical Instruments Department,
'Sahas'414/2 Veer Savarkar Marg,
Prabhadery Mumbai 400 025, India
Telephone: 91-22-5666-4068
Facsimile: 91-22-5666-4001

Blue Star LTD. (New Delhi)
Analytical Instruments Department,
E-44/12 Okhla Industrial Area,
Phase-11, New Delhi 110 020, India
Telephone: 91-11-5149-4000
Facsimile: 91-11-5149-4004

Blue Star LTD. (Calcutta)
Analytical Instruments Department,
7, Hare Street Calcutta 700 001, India
Telephone: 91-33-2248-0131
Facsimile: 91-33-2248-1599

Blue Star LTD. (Chennai)
Analytical Instruments Department, Lakshmi
Neela Rite Choice Chambers, 5, Bazullah Road,
3rd Floor T. Nagar Chennai 600 017, India
Telephone: 91-44-2815-8846
Facsimile: 91-44-2815-8015

INDONESIA
PT. TEKNOLABindo PENTA PERKASA
J1. Gading BukitRaya,
Komplek Gading Bukit Indah Blok I/11,
Kelapa Gading Jakarta 14240, Indonesia
Telephone: 62-21-45847057/58/59
Facsimile: 62-21)-45842729

IRAN
IMACO LTD.
No. 141 Felestin Ave.,
P. O. Box 13145-537, Tehran, Iran
Telephone: 98-21-6402191/6404148
Facsimile: 98-21-8978164

ITALY
JEOL (ITALIA) S.p.A.
Centro Direzionale Green Office Via Dei Tulipani,
1, 20090 Pieve, Emanuele (MI), Italy
Telephone: 39-2-9041431
Facsimile: 39-2-90414353

KOREA
JEOL KOREA LTD.
Sunmin Bldg. 6th F1.,218-16, Nonhyun-Dong,
Kangnam-Ku, Seoul, 135-010, Korea
Telephone: 82-2-511-5501
Facsimile: 82-2-511-2635

KUWAIT
YUSUF I. AL-GHANIM & CO. (YIACO)
P. O. Box 435, 13005 - Safat, Kuwait
Telephone: 965-4832600/4814358
Facsimile: 965-4844954/4833612

MALAYSIA
JEOL (MALAYSIA) SDN. BHD. (359011-M)
205, Block A, Mezzanine Floor,
Kelana Business Center97,
Jalan SS 7/2, Kelana Jaya,
47301 Petaling Jaya, Selangor, Malaysia
Telephone: 60-3-7492-7722
Facsimile: 60-3-7492-7723

MEXICO
JEOL DE MEXICO S.A. DE C.V.
Av. Amsterdam #46 DEPS. 402
Col. Hipodromo, 06100 Mexico D.F. Mexico
Telephone: 52-5-55-211-4511
Facsimile: 52-5-55-211-0720

PAKISTAN
ANALYTICAL MEASURING SYSTEM (PVT) LTD.
(AMS LTD.)
F-8/1-5, KDA Scheme No. 1,
Main Tipu Sultan Road,
P. O. Box 10604, Karachi-75350, Pakistan
Telephone: 92-21-4525185/4525186
Facsimile: 92-21-4316331/4316332

PANAMA
PROMED S.A.
Parque Industrial Costa del Este
Urbanizacion Costa del Este
Apartado 6281, Panama, Panama
Telephone: 507-269-0044
Facsimile: 507-263-5622

PHILIPPINES
PHILAB INDUSTRIES INC.
7487 Bagtikan Street, SAV Makati, 1203 Metro,
Manila Philippines
Telephone: 63-2-896-7218
Facsimile: 63-2-897-7732

PORTUGAL
Izasa. Portugal Lda.
R. do Proletariado 1,
2790-138 CARNAXIDE Portugal
Telephone: 351-21-424-7300
Facsimile: 351-21-418-6020

SAUDI ARABIA
ABDULREHMAN ALGOSAIBI G. T.B.
Algosaibi Bldg., Airport Rd., P. O. Box 215,
Riyadh 11411, Saudi Arabia
Telephone: 966-1-479-3000
Facsimile: 966-1-477-1374

SCANDINAVIA
JEOL (SKANDINAVISKA) A.B.
Hammarbacken 6 A, Box 716
191 27 Sollentuna, Sweden
Telephone: 46-8-28-2800
Facsimile: 46-8-29-1647

SERVICE & INFORMATION OFFICE
JEOL NORWAY
Ole Deviks vei 28, N-0614 Oslo, Norway
Telephone: 47-2-2-64-7930
Facsimile: 47-2-2-65-0619

JEOL FINLAND
Ylakaupinkuja 2, FIN-02360 Espoo, Finland
Telephone: 358-9-8129-0350
Facsimile: 358-9-8129-0351

JEOL DENMARK
Naverland 2, DK-2600 Glostrup, Denmak
Telephone: 45-4345-3434
Facsimile: 45-4345-3433

SINGAPORE
JEOL ASIA PTE. LTD.
29 International Business Park,
#04-02A Acer Building,
Tower B Singapore 609923
Telephone: 65-6565-9989
Facsimile: 65-6565-7552

SOUTH AFRICA
ADI Scientific (Pty) Ltd.
109 Blandford Road, North Riding,Randburg
(PO box 71295 Bryanston 2021)
Republic of South Africa
Telephone: 27-11-462-1363
Facsimile: 27-11-462-1466

SPAIN
IZASA. S.A.
Aragoneses, 13,
28100 Alcobendas,
(Polígono Industrial) Madrid, Spain
Telephone: 34-91-663-0500
Facsimile: 34-91-663-0545

SWITZERLAND
JEOL(GERMANY)GmbH
Oskar-Von-Miller Strasse 1,
85386 Eching Germany
Telephone: 49-8165-77346
Facsimile: 49-8165-77512

TAIWAN
JIE DONG CO., LTD.
7F, 112, Chung Hsiao East Road, Section 1, Taipei,
Taiwan 10023, Republic of China
Telephone: 886-2-2395-2978
Facsimile: 886-2-2322-4655

JEOL TAIWAN SEMICONDUCTORS LTD.
11F, No. 346, Pei-Ta Road, Hsin-Chu City 300,
Taiwan Republic of China
Telephone: 886-3-523-8490
Facsimile: 886-2-523-8503

THAILAND
BECTHAI BANGKOK EQUIPMENT
& CHEMICAL CO., Ltd.
300 Phaholyothin Rd. Phayathai,
Bangkok 10400, Thailand
Telephone: 66-2-615-2929
Facsimile: 66-2-615-2350/2351

THE NETHERLANDS
JEOL (EUROPE) B.V.
Tupolevlaan 28-A, 1119 NZ Schiphol-Rijk,
The Netherlands
Telephone: 31-20-6533088
Facsimile: 31-20-6531328

TURKEY
TEKSER LTD. STI.
Acibadem Cad. Erdem Sok. Baver Art. 6/1
34660 Uskudar/Istanbul-Turkey
Telephone: 90-216-3274041
Facsimile: 90-216-3274046

UAE
BUSINESS COMMUNICATIONS LLC.
P. O. Box 2534, Abu Dhabi UAE
Telephone: 971-2-6348495
Facsimile: 971-2-6316465

USA
JEOL USA, INC.
11 Dearborn Road, Peabody, MA. 01960, U. S. A.
Telephone: 1-978-535-5900
Facsimile: 1-978-536-2205/2206

JEO USA, INC. WEST OFFICE
5653 Stoneridge Drive Suite
#110 Pleasanton, CA. 94588 U. S. A.
Tel: 1-925-737-1740
Fax: 1-925-737-1749

VENEZUELA
MITSUBISHI VENEZOLANA C. A.
Avenida Francisco de Mirande Los Palos Grandes,
Carecas, Venezuela
Telephone: 58-212-209-7402
Facsimile: 58-212-209-7496